Downloaded from orbit.dtu.dk on: Jun 04, 2024

DTU Library

Ultrafast Field Emission Processes with Terahertz and Mid-Infrared Radiation

Welsch, Malte Lasse

Publication date:
2023

Document Version
Publisher's PDF, also known as Version of record

Link back to DTU Orbit

Citation (APA):
Welsch, M. L. (2023). *Ultrafast Field Emission Processes with Terahertz and Mid-Infrared Radiation*. Technical University of Denmark.

General rights
Copyright and moral rights for the publications made accessible in the public portal are retained by the authors and/or other copyright owners and it is a condition of accessing publications that users recognise and abide by the legal requirements associated with these rights.

- Users may download and print one copy of any publication from the public portal for the purpose of private study or research.
- You may not further distribute the material or use it for any profit-making activity or commercial gain
- You may freely distribute the URL identifying the publication in the public portal

If you believe that this document breaches copyright please contact us providing details, and we will remove access to the work immediately and investigate your claim.

Supervisor: Prof. Peter U. Jepsen
Co-supervisors: Associate Prof. Edmund J. R. Kelleher

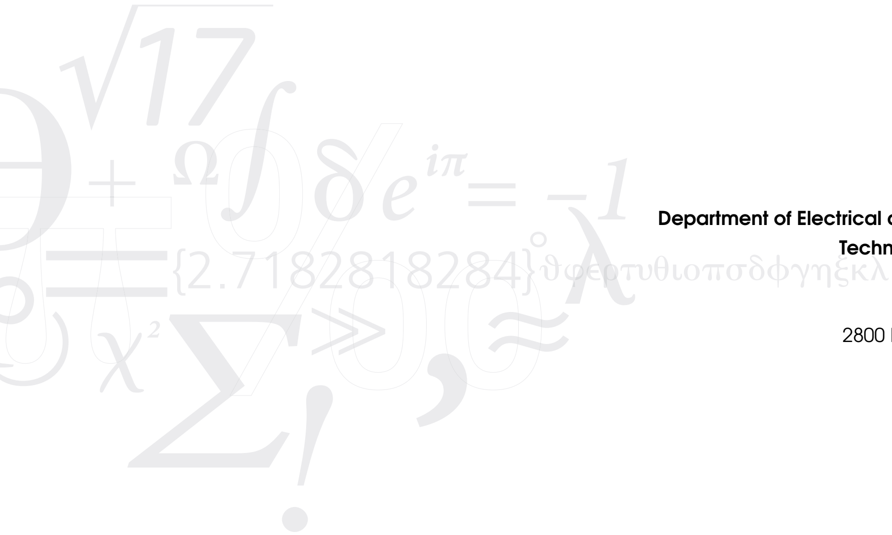

DTU Electro
Department of Electrical and Photonics Engineering
Technical University of Denmark
Ørsteds Plads
Building 343
2800 Kongens Lyngby, Denmark

“Action is the foundational key to all success. ”

- Pablo Picasso

Acknowledgements

I want to use a few pages to express my gratitude to the people who helped, supported, and made my life better during the past 3 years.

First and foremost, I owe a tremendous debt of thanks to **Prof. Peter U. Jepsen**. Thanks to his scientific expertise, this project came to fruition. As my principal supervisor, he struck the perfect balance between providing guidance and allowing me the freedom to explore my own ideas. It was an absolute privilege to work alongside a luminary in the THz field. Equally deserving of recognition is **Prof. Edmund J. R. Kelleher**, who provided important guidance and insights to the project. He always was open to discussions. It was a pleasure to have him as my co-supervisor.

I want to extend my genuine thanks to my friend and project partner, **Martin J. Cross**. His friendship, guidance, and support have been invaluable throughout the past 3 years. Martin's expertise in the lab, data analysis, programming, and personal matters has helped me grow and learn tremendously. I am truly grateful for his unwavering support, and I feel fortunate to have had him by my side during this project. Not less important for the preparation of this thesis was my friend and office mate, **Sergio I. R. Puentes**. His presence and contributions have had a significant impact on my experience during my PhD studies. We have engaged in numerous valuable discussions, and his company has made our office environment more enjoyable. I want to express my heartfelt gratitude for his friendship and unyielding support throughout this journey.

Also, to work with **Dr. Tobias O. Buchmann** was enrichment and pleasure. Besides his professional guidance, spending time with him outside DTU has always been a source of joy. I extend my thanks to **Dr. Matej Sebek** for engaging in discussions about finite element simulations and SEM imaging of the metasurfaces. I also am grateful to **Dr. Simon J. Lange** for his pioneering work on the subject and for always being open to answering my questions. Special thanks to **Prof. Binbin Zhou** for his expertise and assistance with the laser system, as well as for the insightful discussions on optics. Your input has been immensely helpful in addressing various challenges.

Additionally, I want to express my appreciation to **Lars R. Lindvold** for the preparation of dye-doped liquid samples and his expertise in fluorescent molecules. Of great importance for the experimental pursuit of the project was the mechanical workshop of DTU Electro.

Thanks to **John Lauridsen**, **Martin Nielsen**, and **Jan N. Mortensen** for machining many important structures with perfection. I am also deeply grateful to **Dr. Moritz Fischer** for his inexhaustible commitment to promoting a healthy work-life balance, particularly on Friday evenings. Moreover, I would like to extend my gratitude to all current and former colleagues of the Ultrafast Infrared and Terahertz Science group for creating a pleasant and collaborative work environment.

I am especially grateful to **Prof. David G. Cooke** for hosting me during my external stay in his lab. I enjoyed my stay in his group and my discussion with him in the lab. I am thankful to have had the possibility to meet, work and spend time outside of the lab with **Benjamin Colmey**, **Aidan Schiff-Kearn**, **Benjamin Dringoli**, **Rodrigo T. Paulino**, and **Huiwen Shen**. They made my research stay an unforgettable experience. I want to thank especially Benjamin C. and Aidan. During this research stay, I met many other remarkable individuals; here, I want to highlight **Soud Al Kharusi** and thank him for being so welcoming and inclusive to me.

Many thanks as well to **my family**, who supported me during the entire pursuit of my PhD. Moreover, I would like to acknowledge the help and support of my girlfriend, **Michaela**. Her understanding of the long hours and nights spent in the lab, as well as the much-needed balance she provided to my work, have been truly appreciated. Last but certainly not least, I want to express my gratitude to my long-time friend and former lab partner, **Michael Wißmann**, for his constant support and belief in me.

Abstract

This thesis presents an experimental and theoretical investigation of electron field emission from metallic micro antennas in the Terahertz (THz) and mid-infrared (mid-IR) regions of the electromagnetic spectrum and their potential application in ultrafast spectroscopy and mid-IR detection. The thesis begins by presenting the fundamental knowledge about THz generation and detection, followed by an introduction to the Fowler-Nordheim field emission theory. After the fundamentals for this thesis are explained, the performed experiments, results, and analyses are presented.

The first experimental part of the thesis focuses on the application of metallic field emitters for THz radiation and investigates the electron field emission into gaseous and liquid samples. The results demonstrate that electrons can be field emitted into those media. The gaseous samples show a good agreement with the Fowler-Nordheim theory. However, the emission into the liquid samples deviates from the expected Fowler-Nordheim trend, which is attributed to the influence of other field-induced effects. A correction constant is introduced, taking these field effects into account. Additionally, the study presents a simple simulation for electron acceleration in gaseous environments and showcases the importance of the potential barrier shape in the Fowler-Nordheim emission, and gives insights into realistic parameter choice in the field emission theory.

The second study presented in this thesis examines a novel mid-IR photo-multiplier tube (PMT) based on field emission nano-antennas. The study characterizes the PMT with respect to its wavelength-dependent response, which is as well simulated using COMSOL$^{®}$. As a potential use case, interferometric autocorrelations with the PMT as the detector are performed and analyzed by simulations of the autocorrelation traces. The performance of the PMT for application in autocorrelations measurements is compared to standard 2-photon-based mid-IR autocorrelations.

Overall, this thesis presents important findings that contribute to the understanding of electron field emission from metallic micro-antennas and their potential applications in ultrafast spectroscopy and mid-IR detection. The research emphasizes the importance of understanding the electron field emission process and the influence of other field-induced effects on the emission process. Additionally, the novel mid-IR PMT based on field emission nano-antennas shows potential for use in mid-IR detection applications. These findings could have significant implications for the development of new technologies in the THz and mid-IR regions.

Resumé

Denne afhandling præsenterer en eksperimentel og teoretisk undersøgelse af elektron feltudsendelse fra metalliske mikroantenner i Terahertz (THz) og mid-infrarød (mid-IR) regionerne af det elektromagnetiske spektrum samt deres potentielle anvendelse inden for ultrahurtig spektroskopi og mid-IR detektion. Afhandlingen begynder med at præsentere den grundlæggende viden om THz-generering og -detektion efterfulgt af en introduktion til Fowler-Nordheim-feltudsendelsesteorien. Efter at grundlaget for denne afhandling er forklaret, præsenteres de udførte eksperimenter, resultater og analyser.

Den første eksperimentelle del af afhandlingen fokuserer på anvendelsen af metaliske feltudsendere til THz-stråling og undersøger elektron feltudsendelse i gassede og flydende prøver. Resultaterne viser, at elektronen kan udsendes i disse medier. Gassprøverne viser en god overensstemmelse med Fowler-Nordheim-teorien. Imidlertid afviger udsendelsen til de flydende prøver fra den forventede Fowler-Nordheim-trend, hvilket tilskrives påvirkningen af andre feltinducerede effekter. En korrektionskonstant introduceres, der tager hensyn til disse felteffekter. Derudover præsenterer undersøgelsen en simpel simulering af elektronacceleration i gassede miljøer og demonstrerer vigtigheden af potentialebarrierens form i Fowler-Nordheim-udsendelse og giver indsigt i realistisk valg af parametre i feltudsendelsesteorien.

Den anden undersøgelse, der præsenteres i denne afhandling, undersøger en ny mid-IR fotomultiplikator (PMT) baseret på feltudsendelsesnanoantenner. Undersøgelsen karakteriserer PMT'en med hensyn til dens bølgelængdeafhængige respons og simuleres ved hjælp af COMSOL®. Som et potentiale anvendelsesområde udføres interferometriske autocorrelationer og analyseres ved hjælp af simuleringer af autocorrelationssporene. PMT'ens ydeevne til anvendelse i autocorrelationsmålinger sammenlignes med standard 2-foton-baserede mid-IR-autocorrelationer.

Overordnet set præsenterer denne afhandling vigtige resultater, der bidrager til forståelsen af elektronfeltudledning fra metal-mikroantenner og deres potentielle anvendelser i ultra-hurtig spektroskopi og mid-IR-detektion. Forskningen understreger vigtigheden af at forstå elektronfeltudledningsprocessen og påvirkningen af andre feltinducerede effekter på udledningsprocessen. Derudover viser den nye mid-IR PMT baseret på feltudledende nanoantenner potentiale til anvendelse i mid-IR-detektionsapplikationer. Disse resultater kan have betydelige implikationer for udviklingen af nye teknologier inden for THz- og mid-IR-regionerne af det elektromagnetiske spektrum.

Preface

This thesis, with the title ”Ultrafast Field Emission Processes with Terahertz and Mid-Infrared Radiation,” presents the main results obtained during the period from February 1, 2020, to May 23, 2023, while pursuing my Ph.D. degree at the Technical University of Denmark (DTU) under the supervision of Prof. Peter Uhd Jepsen and co-supervision of Associate Prof. Edmund John Railton Kelleher, both from the Department of Electrical and Photonics Engineering (DTU Electro, former DTU Fotonik). All the results presented in this thesis were obtained at the Technical University of Denmark. In the time between June 28, 2022, and October 26, 2022, I had the opportunity to stay in Prof. David G. Cooke's group at the University of McGill, Montreal, Canada, and to work on a related project on electron field emission.

It is important to note that all the presented results in this thesis were obtained by me. The applied metasurfaces in chapter 3 were fabricated by Dr. Simon J. Lange from DTU Electro. The in chapter 4 discussed photomultiplier tube was designed by Dr. Simon J. Lange, assembled by Hamamatsu Photonics, and handed over to me by Dr. Tobias O. Buchmann from DTU Electro. The liquid samples discussed in chapter 3 were prepared by Dr. Lars Lindvold from DTUs Department of Health Technology. All other components used in the experiments were either commercially purchased or manufactured by the in-house workshop at DTU Electro.

The project ULTRA-TED was fully funded by the Independent Research Fund Denmark (Danmarks Frie Forskningsfond), which provided, amongst others, my salary, financial support for the purchase of equipment and materials, and travel expenses. I also obtained a grant for financial support during my external stay from the Otto Mønsteds Fond.

Kongens Lyngby, 23rd May 2023

Malte Lasse Welsch

Contents

Introduction 1

I Fundamentals 3

1 Terahertz Radiation 5
- 1.1 THz Radiation 5
- 1.2 THz Generation 6
  - 1.2.1 Optical Rectification 6
  - 1.2.2 Tilted Pulse Front 9
  - 1.2.3 Experimental Realization of the THz Setups 12
  - 1.2.4 Other Generation Schemes 14
- 1.3 THz-Detection 14
  - 1.3.1 Electro-Optic Sampling 14
  - 1.3.2 Other Detection Methods 17
  - 1.3.3 Field-Strength Calibration 17

2 Electron Field Emission 19
- 2.1 Mechanism of Cold Field Emission 20
  - 2.1.1 Fowler-Nordheim Theory 21
  - 2.1.2 Potential Barrier Shape for Fowler-Nordheim-Type Emission 22
  - 2.1.3 Linear Fowler-Nordheim Plots 23
  - 2.1.4 Keldysh Parameter 24
- 2.2 Field Emitters 24

II Experimental Techniques and Results 27

3 Electron Triggered Reactions in Liquids and Gases 29
- 3.1 Introduction 30
- 3.2 Methods 32
  - 3.2.1 Experimental Setup 32
  - 3.2.2 Samples 34
- 3.3 Measurements 35
  - 3.3.1 Field Emission in Gases and Liquids 35

3.3.2 Simulation of Electrons in Argon Gas 44
3.4 Conclusion 50

4 Mid-IR PMT based on Field Emission 53
4.1 Introduction 54
4.2 Methods/Tools 55
4.2.1 midIR-PMT 55
4.2.2 Optical Setups 56
4.3 Experiments and Results 58
4.3.1 PMT-Characterization 58
4.3.2 Fowler-Nordheim-Autocorrelation 65
4.4 Conclusion 76

Conclusion 79

Appendices 83

Bibliography 95

Introduction

The common theme of this thesis revolves around the field emission of electrons by light waves. In the first part, this theme is explored through the application of Terahertz radiation, while the second part investigates the utilization of mid-infrared radiation to drive the field emission process.

Electron field emission is a quantum mechanical process of an electron tunneling through the potential barrier of a medium into free space when an electric field is applied to the surface of the medium.

The first observation of field emission by Winkler dates back to the 18th century [1] but could not be explained as an electron escaping the medium until Thomson described the electron in 1897 [2]. In 1922, Lilienfeld published an article [3] that drew the attention closer to the process. Many physicists work on the explanation of the problem, among others, Millikan, Schottky, and Oppenheimer [4]. Fowler and Nordheim published then, in 1928, the mathematical elucidation of the problem [5], which is, until today, the theoretical basis for the description of the electron field emission.

In the static electric field, electron field emission is, for instance, applied in field emission microscopy [6] or in high-resolution scanning electron microscopes [7]. However, the electric field of light waves can cause electron field emission as well. An indicator of whether the applied frequency of the radiation leads to electron emission due to multiphoton absorption or field emission is the Keldysh parameter γ [8]. For $\gamma \ll 1$, field emission is more likely than multiphoton absorption. This is the case for the Terahertz and mid-infrared radiation applied in this thesis.

In the past, Terahertz and mid-infrared induced field emission from different emitters such as nanorods [9], single-tip emitters [10–13], and metallic antennas [14] were investigated and applied in novel technologies [15, 16].

In this thesis, Terahertz and mid-infrared have been utilized to field-emit electrons from metallic metasurfaces. The research question for the THz part of this thesis is to verify the direct Terahertz-driven electron field emission into liquids and their possibility of triggering a chemical reaction in the liquid environment. On top of that, the influence of the strong THz field on the liquid shall be considered. For the mid-IR part, the research question is more of technological origin. It should be answered how well the field emission performs as a broadband mid-IR detector and whether it can be applied in autocorrelation measurements.

To address these research questions, the thesis is structured into two parts. The first part, *Fundamentals*, introduces the underlying concepts and methods applied in the thesis. The chapter on THz techniques covers the generation of THz radiation with a focus on optical rectification, as well as THz detection and calibration of field strength. The second chapter provides an overview of electron field emission and describes the metasurfaces used in the experiments. The second part of the thesis, *Experimental Techniques and Results*, is dedicated to the experiments and their findings. This part consists of two chapters, one on THz field emission titled *Electron Triggered Reactions in Liquids and Gases*, and the other on mid-IR PMT based on field emission named *Mid-IR PMT based on Field Emission*. Each chapter is structured with an introduction, a description of the methods and tools, an experimental and results section, and a conclusion. Finally, the thesis is concluded with a summary of the key findings and their implications for future research.

Part I

Fundamentals

CHAPTER 1

Terahertz Radiation

This chapter aims to provide a broad overview of terahertz (THz) techniques, concentrating on THz generation and detection. The primary focus will be on sources based on lithium niobate, $LiNbO_3$ (LN) that utilize a tilted pulse front (TPF) pump scheme. For THz detection, electro-optic sampling (EOS) will be discussed, as well as other detection methods. Lastly, possible approaches for THz field calibration will be debated.

1.1 THz Radiation

The THz regime is loosely defined as spanning from 0.1 to 30 THz in the electromagnetic spectrum. This spectral range was formerly known as the ”THz Gap” due to the lack of emitters and receivers available. Nonetheless, THz radiation presents numerous valuable properties for scientific and technological applications, including time-of-flight measurements [17, 18], spectroscopic tools [19], and even communication [20]. Consequently, researchers and engineers have made considerable efforts to bridge the ”THz Gap.” Various approaches, from the electrical and optical sides of the spectrum, have been developed to create sources that cover the THz range.

Generating THz radiation using electrical elements is challenging because of parasitic capacities and the saturation of electron drift velocity in semiconductors. These factors make it difficult to use the same technologies for THz generation as for microwaves. Nonetheless, backward wave oscillators and gun diodes offer the possibility of generating up to 1 THz, but power output drops significantly for higher frequencies [21, 22]. Semiconductor devices are unsuitable for THz generation due to the low energy of THz radiation (4.14 meV), which corresponds to an energy of 48K and is prone to thermal noise. However, recent advancements in quantum cascade laser technology have made it possible to create THz sources based on semiconductor quantum structures [23].

Femtosecond laser pulses are applied to approach the THz regime from the optical side. The optical pulse pumps different materials like semiconductors for photoconductive antenna (PCA) [24], nonlinear crystals [25, 26], and air plasma [27]. The properties of emitted THz pulse are strongly dependent on the source.

Nowadays, the ”THz Gap” is nearly closed, but the sources must be optimized for field strength, output power, or spectral bandwidth. The strong absorption of the THz radiation by the humidity in ambient air and low conversion efficiency from optical to THz power still gives much space for new developments.

In this thesis, the approach used for THz generation is based on optical methods. Hence, only optical techniques will be described in the following.

1.2 THz Generation

In this section, several techniques for optically generating THz radiation will be discussed, with a particular focus on optical rectification (OR). OR is the primary principle used for the underlying thesis and will therefore receive the most attention. Nevertheless, it's important to acknowledge that other methods for THz generation exist, including photoconductive switches and air plasma generation. However, due to the focus of this section on optical rectification, these methods will only be briefly mentioned.

1.2.1 Optical Rectification

The following discussion can be found in many textbooks for non-linear optics. Here, mostly used as a reference are [28] and [29].

The interaction of strong light fields with matter gives rise to the field of nonlinear optics. The electron response to the field is linear in weak optical fields. The electron motion is proportional to the electric field amplitude and the dielectric polarization density $P(t)$ is expressed as follows:

$$P(t) = \epsilon_0 \chi^{(1)} E(t) \tag{1.1}$$

Here, ϵ_0 is the vacuum permittivity, $E(t)$ is the incident electric field, and $\chi^{(1)}$ is the first-order susceptibilities of the medium. The Lorentz-oscillator model can describe electron motion quite well for the linear case. The electrons are treated as oscillators driven by the electrical field, and dispersion and absorption in the material for low field strengths can be calculated. However, for a strong electric field, the electronic response of the medium is no longer linear, and a nonlinear polarization is induced. This polarization leads to new optical properties of the material. Expanding the nonlinear polarization leads to

$$\begin{aligned} P(t) &= \epsilon_0 \left(\chi^{(1)} E(t) + \chi^{(2)} E^2(t) + \chi^{(3)} E^3(t) + ... \right) && (1.2) \\ &= P^{(1)}(t) + P^{(2)}(t) + P^{(3)}(t) + ... && (1.3) \end{aligned}$$

OR is a second-order nonlinear process, and hence the focus is on

$$P^{(2)}(t) = \epsilon_0 \chi^{(2)} E^2(t) \tag{1.4}$$

of the nonlinear polarization. The second-order non-linearity only takes place in non-centrosymmetric materials.
Assuming an electromagnetic wave with the electric field of

$$E(t) = E_0 e^{-i\omega t} + c.c. \tag{1.5}$$

incidence on non-centrosymmetric material results in two terms.

$$P^{(2)}(2\omega) = \epsilon_0 \chi^{(2)} E_0^2 e^{-2i\omega t} + c.c. \;\; \& \;\; P^{(2)}(0) = \epsilon_0 \chi^{(2)} E_0^2 \tag{1.6}$$

The $P^{(2)}(2\omega)$-term describes the sum-frequency generation (sum-frequency generation (SFG)), while the $P^{(2)}(0)$-term expresses a DC component in the polarization. The latter means that the average location of the dipoles is changing. The DC-term shows no effect for slowly varying optical powers. However, for short laser pulses, the DC component is increased and again decreased in a short time, leading to the re-emission of electromagnetic radiation. In the case of femtosecond Gaussian laser pulse, the envelope of the pulse is comparable to the time evolution of the polarization and gives rise to THz radiation with a bandwidth of approximately the inverse of the laser pulse duration [29].

Another way to view the THz generation by OR is to consider the bandwidth of the ultrashort Gaussian laser beam. Let us define the incident electric field as

$$E(t) = E_1 e^{-i\omega_1 t} + E_2 e^{-i\omega_2 t} + c.c. \;\; . \tag{1.7}$$

The substitution of equation (1.7) in equation (1.4) leads to different terms such as second-harmonic generation (second-harmonic generation (SHG)), SFG, different-frequency generation (difference-frequency generation (DFG)), and OR [28].

$$\text{SHG:} \;\; P(2\omega_1) = \epsilon_0 \chi^{(2)} E_1^2, \;\; P(2\omega_2) = \epsilon_0 \chi^{(2)} E_2^2 \tag{1.8}$$

$$\text{SFG:} \;\; P(\omega_1 + \omega_2) = 2\epsilon_0 \chi^{(2)} E_1 E_2 \tag{1.9}$$

$$\text{DFG:} \;\; P(\omega_1 - \omega_2) = 2\epsilon_0 \chi^{(2)} E_1 E_2^* \tag{1.10}$$

$$\text{OR:} \;\; P(0) = 2\epsilon_0 \chi^{(2)} (E_1 E_1^* + E_2 E_2^*) \tag{1.11}$$

Not all of these nonlinear processes happen at the same time. Phase-match conditions select one dominating process and its complementary one. The herein labeled OR-term describes a DC component in the polarization as previously seen in equation (1.6). Relevant for THz generation is here as well the DFG- term. A laser pulse from a mode-locked laser can be seen as a frequency comb [30] with discrete frequency steps. The DFG between all frequency components contained in the laser pulse generates THz-radiation.

In the discussion above, the dielectric polarization density $P(t)$ and the electric fields $E(t)$ were scalar quantities. However, a full description of the nonlinear process needs to consider the vector nature of $P(t)$ and $E(t)$. Doing that, the susceptibilities χ^n become tensors of the rank $(n+1)$. The tensors are dependent on the lattice structure of the nonlinear crystal. This leads to the complete expression [28]

$$P_i(\omega_n + \omega_m) = \epsilon_0 \Sigma_{jk} \Sigma_{(nm)} \chi^{(2)}_{ijk}(\omega_n + \omega_m, \omega_n, \omega_m) E_j(\omega_n) E_k(\omega_m) \tag{1.12}$$

Here i, j, and k can represent the field's Cartesian coordinates x, y, and z. n and m represent the interacting frequencies of the fields. Due to the symmetry of the crystals and dependent on the mixing frequencies, $\chi^{(2)}$ can be simplified in the so-called d-matrix. For further details, please consult [28, 29]. Performing the mathematical description for OR for the used crystal gives the polarization of the resulting THz field and optical field for maximal THz generation efficiency. This concludes that the optical field has to be oriented along a certain crystalline axis. Hence, only specific crystal cuts show efficient THz generation [29].

So far, the generation mechanism of THz radiation by means of OR based on a field-induced nonlinear polarization in the material has been discussed. Let us now take a look at the propagation of the THz wave through the medium. Therefore the nonlinear wave equation needs to be formulated. For the full derivation, please see [28]. The following nonlinear wave equation is taken from [29]

$$\frac{\partial^2 E_{THz}(z,t)}{\partial z^2} - \frac{n_{THz}^2}{c^2}\frac{\partial^2 E_{THz}(z,t)}{\partial t^2} = \frac{1}{\epsilon_0 c^2}\frac{\partial^2 P_{THz}^{(2)}(z,t)}{\partial t^2} \tag{1.13}$$

Here the nonlinear polarization acts as a source term for the emitted THz field. Solving the nonlinear wave equation leads to an expression for the emitted THz field. The THz field is dependent on the refractive index of the crystal for the optical electric field n_O and for the generated THz-field n_{THz}. Considering an idealized crystal with $n_O = n_{THz}$, the emitted THz and the optical pulse would travel at the same speed. The optical pulse and the THz pulse are in phase, and due to constructive interference of the emitted THz fields at every point in the crystal, the THz field gets amplified proportionally to the distance l traveled through the crystal. However, in non-idealized crystals, the THz- and the optical fields have non-identical refractive indices, which cause a walk-off between the optical pulse and the generated THz field. As a consequence, the THz fields generated at separate positions in the crystal no longer have the same phase and interfere destructively. This reduces the overall emitted THz-power. After a phase delay of $\pi/2$, the amplitude of the emitted THz field decreases again. Thereby, the coherence length l_c can be defined as the length in a crystal after which the THz and the optical pulse are out of phase by $\pi/2$ [29].

$$l_c = \frac{\lambda_{THz}}{2|n_{gr} - n_{THz}|} \tag{1.14}$$

Here, also the dispersion of the nonlinear crystal is considered. The phase matching can only be optimized for a certain THz frequency. For the optical pulse, the group index n_{gr} is applied, while for the THz pulse, the refractive index n_{Thz} of the center wavelength is used.

Besides the walk-off between the optical and THz pulse, re-absorption of the THz radiation in the crystal lowers the THz bandwidth and power. As all crystals at room temperature, also the nonlinear crystals used for THz generation pose phonons (lattice vibrations). The optically active phonons in crystals are energetically located in the THz emission band, which reabsorb the emitted THz pulse. This sets a limit to the emitted THz bandwidth. Moreover, absorption of the optical light leads to heat accumulation in the nonlinear crystal, which sets a limit to applied optical powers due to the risk of causing damage to the crystal.

Assuming that the DFG in the nonlinear crystal is the source for THz-emission, the THz generation efficiency η_{THz} for the phase-matched case can be expressed through the following equation [26].

$$\eta_{THz} = \eta_0 \cdot e^{-\alpha_{THz} L/2} \cdot \frac{\sinh^2\left[\alpha_{THz}(L/4)\right]}{\left[\alpha_{THz} L/4\right]^2} \quad \text{with} \quad \eta_0 = \frac{2\omega^2 d_{eff}^2 L^2 I}{\varepsilon_0 n_{NIR}^2 n_{THz} c^3} \tag{1.15}$$

Here the quantities are L the crystal thickness and α_{THz} the intensity absorption coefficient for generated THz wave, ω the angular frequency of the THz, d_{eff} the effective nonlinear coefficient, I the intensity of the pump light, ϵ_0 the vacuum permittivity, n_{NIR} and n_{THz} are the refractive indices of the pump light and the THz radiation respectively, and c the vacuum speed of light.

For small absorption $(\alpha_{THz}L \ll 1)$, only η_0 remains and one could hypothesize that the efficiency would increase with the thickness of the nonlinear crystal. However, in reality, absorption occurs. Hence, for crystal length longer than α_{THz}^{-1}, the generation efficiency does not increase further. Only the THz photons generated in the distance α_{THz}^{-1} to the surface of the crystal can be emitted [26].

Another important parameter for efficient THz generation is the effective nonlinear coefficient d_{eff}. It is a material and pump polarization-dependent quantity to quantify the strength of the nonlinearity of the material and can be derived from the above-mentioned d-matrix. The greater the d_{eff} of a material, the stronger the nonlinear response and the more efficient the THz generation.

In table 1.1, important parameters for selected materials for THz generation are displayed.

Table 1.1. Optical and electro-optical properties of selected materials.

Material	n_{gr} (800 nm)	n_{THz} (1 THz)	d_{eff} [pm V^{-1}]
GaP	3.67 [26]	3.34 [26]	24.8 [26] (@800 nm)
ZnTe	3.13 [26]	3.17 [26]	68.5 [26] (@800 nm)
sLiNbO$_3$	2.25 [26]	4.96 [26]	168 [26] (@800 nm)

From table 1.1, one can see that for gallium phosphide (GaP) and zinc telluride (ZnTe), the group indices n_{gr} and the THz refractive indices n_{THz} are close to each other which makes it possible to generate THz radiation co-linear to the pump beam due to a long coherence length. This is not the case LN. Here the mismatch between n_{gr} and n_{THz} leads to a rapid phase-mismatch which causes inefficient THz generation. However,LN shows a high effective nonlinear coefficient d_{eff}, and due to that, it is still used for THz generation with the tilted pulse front method. As it was used during the experimental part of this thesis, the technique is elucidated in section 1.2.2. GaP, ZnTe, and LN are inorganic crystals. In recent years, organic crystals have become increasingly popular for THz generation due to their favorable phase-matching properties for co-linear THz generation and high optical-to-THz conversion efficiencies [31–33]. However, their low damage thresholds often constrain their usage of the full available optical power due to thermal heating that causes damage. Hence, feasible heat management is investigated to address this limitation [34].

1.2.2 Tilted Pulse Front

As mentioned earlier, materials with high effective nonlinear coefficients offer better optical-to-THz conversion efficiencies. However, some materials cannot be used in a colinear generation scheme due to enormous differences in the refractive indices between the optical pump and generated THz light. To overcome this limitation, Hebling et al. [35] proposed a new pump scheme that enables the generation of strong THz fields from materials with a large velocity mismatch. Therefore, the pump pulse front is tilted. The idea is to generate THz in a Cerenkov cone-like fashion.

When an optical beam is focused in a nonlinear medium with $n_{op} \ll n_{THz}$, the pump beam travels faster than the generated THz, and the THz is emitted in a Cerenkov cone [36]. The opening angle Θ_C of this cone is given by the expression:

$$\Theta_C = \cos^{-1}\left(\frac{\nu_{THz}}{\nu_{gr}}\right), \tag{1.16}$$

where ν_{THz} is the THz velocity and ν_{gr} is the group velocity of the pump pulse. This phenomenon is known as the electro-optical Cerenkov effect. A schematic drawing of it is presented in figure 1.1 a).

However, this method of THz generation has its limitations. The optical beam must be small in the transverse direction to avoid destructive interference between the THz generated at different points along the lateral extension of the beam. Additionally, focusing the beam to a circular spot results in a cone-shaped emission which limits the collection of the THz radiation. To address this issue, the focus spot can be changed to a line focus to increase the collection efficiency, as the THz will be emitted as a plane wave on both sides of the laser pulse [37]. However, even with this approach, the lateral extension of the pump beam needs to be small, which in turn limits the maximum applied optical power due to the risk of thermal damage to the nonlinear medium. To overcome these limitations, the pulse front can be tilted with respect to the phase plane. This means that the pump beam moves with the velocity ν_{gr}, and the THz is generated perpendicular to the tilted pulse front. In this case, only the projection onto the direction of the THz propagation is important, so the tilt angle γ can be chosen so that velocity matching is fulfilled. The relationship between the THz velocity ν_{THz}

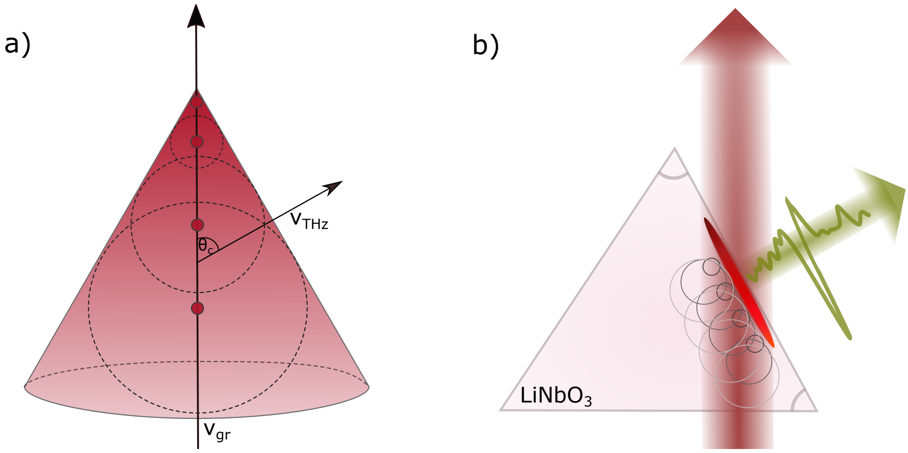

Figure 1.1. In a) the electro-optical Cerenkov effect and in b) the THz generation by tilted pulse front is schematically depicted.

and the pump pulse velocity ν_{gr} is given by:

$$\nu_{THz} = \nu_{gr} \cdot \cos(\gamma) \implies \gamma = \cos^{-1}\left(\frac{n_{gr}}{n_{THz}}\right) \tag{1.17}$$

In figure 1.1 b), the generation of THz due to constructive interference along the TPF is schematically depicted. This thesis exclusively uses LN for THz generation by tilted pulse front. Therefore, the discussion will focus on LN. The tilt angle γ for LN can be calculated to be approximately 63°. It should be noted that γ is the tilt angle required for velocity matching inside the crystal. The pulse front angle outside of the crystal, γ_{free}, is determined by taking the refraction at the crystal-air interface into account, as shown by the following equation:

$$\tan \gamma_{free} = n_{gr} \cdot \tan \gamma \ , \tag{1.18}$$

which leads to $\gamma_{free} \approx 77°$. In the standard TPF experimental setup, the tilt angle is achieved by using a reflective grating. The diffraction caused by the grating results in a tilt of the pulse front. The grating-introduced tilt can be calculated as follows. Assuming the pulse incidence onto the grating under the angle Θ_i and refracts under the angle Θ_d then the path difference Δ between the incident pulse and the diffracted pulse follows by

$$\Delta = \frac{D_{pulse}}{\cos \Theta_d} \cdot (\sin \Theta_i + \sin \Theta_d) \tag{1.19}$$

Here D_{pulse} is the spacial width of the refracted pulse. This expression is found by the assumption that the lateral extension of the pulse is the same for the incident pulse and the refracted. With that expression, one can now calculate the introduced tilt angle γ as follows:

$$\tan \gamma = \frac{\Delta}{D_{pulse}} = \frac{\sin \Theta_i + \sin \Theta_d}{\cos \Theta_d} \tag{1.20}$$

At this point, we apply the grating equation to achieve control about imported experimental parameters as grating grove density p and central wavelength λ_0 dependence.

$$\tan \gamma = \frac{m \lambda_0 p}{\cos \Theta_d} \tag{1.21}$$

m is here the diffraction order. For efficient THz generation, the pulse at the grating needs to be imaged in LN-crystal where the THz is generated. Therefore, the magnification factor β of the imaging system needs to be taken into consideration. Also, the aforementioned additional reduction of the pulse front tilt due to refraction at the air-LN interface leads to the final expression for γ

$$\tan \gamma = \frac{m \lambda_0 p}{n_{gr} \beta \cos \Theta_d} \tag{1.22}$$

As demonstrated in [38], the pulse front tilt is a result of the angular dispersion, which can be incorporated into the equation, revealing its contribution to the phenomenon.

$$\tan \gamma = \frac{m \lambda_0 p}{n_{gr} \beta \cos \Theta_d} = \frac{\lambda_0}{n_{gr} \beta} \frac{d\Theta_d}{d\lambda} \tag{1.23}$$

To achieve the best results, it is important to carefully match the grating image with the tilted pulse front. This is because the shortest time across the tilted pulse front occurs in the image plane, where both long and short-wavelength components of the pump pulse experience similar dispersion. Therefore, to optimize the THz generation process, it is crucial to ensure a good alignment between the grating image and the tilted pulse front [39]. To achieve the best agreement between the image plane and the tilted pulse front, the tilt angle of the image of the grating can be expressed as [40]:

$$\tan \gamma_{im} = n_{gr} \beta \tan \Theta_d \tag{1.24}$$

Equation (1.23) and equation (1.24) allow us to choose the best magnification factor of the imaging system for a specific grating. In a setup with a blazed grating, the grating is typically selected so that the required diffraction angle for the optimal pulse front tilt coincides with the maximum or near-maximum of the grating refraction efficiency. Usually, the diffraction order $m = -1$ is chosen, and refractive efficiencies of more than 90% can be achieved, which is important to utilize most of the available optical power.

The use of a grating for optical-to-THz conversion based on TPF can achieve an efficiency of about 0.1% at room temperature, with a 780 nm pulse of 85 fs duration at 1 kHz [40]. However, cooling the LN crystal to cryogenic temperatures can enhance the conversion efficiency. For instance, S. Huang et al. [41] reported conversion efficiencies of 1.15% at room temperature and 3.8% at cryogenic temperatures using 1030 nm pulses of 680 fs duration, an increase of 2.65 %-percent points. The high efficiency of the OR is attributed to the cascaded generation process, where THz generation can be viewed as a DFG of the frequencies present in the pump frequency comb, as mentioned earlier. This allows a pump photon to participate in the generation of multiple THz photons, exceeding the Manley-Rowe limit, as long as the phase matching condition is satisfied [42]. However, the cascaded process also limits the THz generation efficiency, together with the angular dispersion of the pump pulse introduced by the grating [43].

To overcome the limitation of angular dispersion caused by the grating, a stair-step echelon can be used to achieve the pulse front tilt [44,45]. This method involves delaying discrete beamlets using the echelon to create a pulse front tilt that contains beamlets with a flat pulse front. The tilt angle γ_{ech} of the pulse front in the crystal is given by

$$\tan \gamma_{ech} = \frac{2H}{n_{gr} \beta W} \tag{1.25}$$

where H and W are the step height and width of the echelon, β and n_{gr} are the magnification of the imaging system and the group index of the pump pulse in the LN crystal, respectively.

1.2.3 Experimental Realization of the THz Setups

In this subsection, the main setup for THz generation used for the experimental part of chapter 3 is shortly described. It is mainly based on the presented setup in [40].

It was decided to use an experimental setup based on a TPF- scheme due to the necessity for the generation of strong THz pulses with a low-frequency spectrum to benefit from the lighting rod effect [12, 46]. A schematic drawing of the experimental setup is depicted in figure 1.2. The applied non-linear crystal is a LN-prism with prism angle Θ_{LN} of 63° so that the output facet aligns with the tilted pulse front, allowing efficient outcoupling of the generated THz radiation. The crystal is pumped with $800\,\mathrm{nm}$ pulses from a laser amplifier. The average power of the laser is $4.8\,\mathrm{W}$ with a repetition rate of $1\,\mathrm{kHz}$. The pulse duration is about $100\,\mathrm{fs}$. However, for optimization of the THz generation, the compressor settings are changed, which means the pulse width is changed as well.

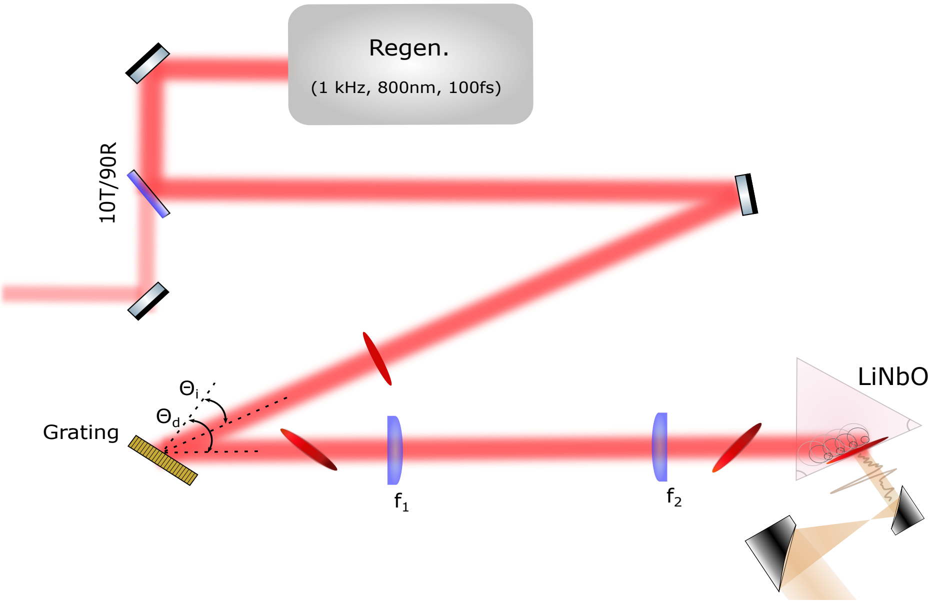

Figure 1.2. Schematic drawing of the THz generation scheme used for the performed experiments.

The beam from the laser is split by a 10/90-plate beam splitter. The transmitted 10% are used for the coherent detection by EOS, which is described in section 1.3.1. The reflected beam is utilized for THz generation by TPF. The tilt of the pulse front is achieved by a grating (715.701.140, Spectrogon) with a groove density of $1800\,\mathrm{grooves/mm}$ with an efficiency of 90% for the diffraction order $m = -1$. The $800\,\mathrm{nm}$-beam incidents under an angle of $\Theta_i = 38°$ onto the grating, which leads to a diffraction angle of $\Theta_d = 55.5$. The diffracted beam is then imaged by two cylindrical lenses onto the LN-crystal. The focal lengths of the lenses are $f_1 = 250\,\mathrm{mm}$ and $f_2 = 150\,\mathrm{mm}$, which are chosen to achieve the correct magnification needed for optimal pulse front tilt angle (see equation (1.24)). The generated THz pulses are expanded and collimated by two metallic off-axis parabolic mirror (OAP)s with a 1:4 ratio of the reflective focal lengths. The collimated beam is propagated to the experimental setup described in section 3.2.1.

1.2.4 Other Generation Schemes

Besides OR, THz radiation can be generated by various techniques, amongst which the most prominent sources are photoconductive antennas (PCA), air-plasma sources, and free-electron lasers (free-electron laser (FEL)). The first two generation schemes are tabletop-based, while the latter are large-scale facilities.

PCA devices are based on semiconductors [36], with the most commonly employed materials being LT-GaAs or InGaAs [47,48], although other materials may be utilized [49]. When a femtosecond laser pulse illuminates the semiconductor, free electron-hole pairs are generated, which are then accelerated by a bias voltage applied across affixed metal electrodes. As a result of this acceleration, a THz pulse is emitted. While standard PCA devices emit relatively low field strength and bandwidth up to around 6 THz, carefully designed electron structures and material engineering of the semiconductor can lead to increased THz field strength or bandwidth [50–54]. Due to their robustness and relatively low optical power requirements, PCA devices are frequently used in commercial THz time-domain spectroscopy (time-domain spectroscopy (TDS)) systems [55].

In contrast to PCA devices, THz generated by an air plasma is known for its broad spectrum with high pulse energies [56–58]. The THz pulse is emitted by a plasma, which is generated due to the focusing of an intense laser pulse into air. The air gets ionized and generates a plasma channel. Macroscopic currents in the plasma lead to broadband THz emission. The emitted bandwidth extends for a standard air-plasma setup up to 15 THz. The broad bandwidth makes it an ideal tool for performing material research such as high-frequency carrier dynamics [59].

FELs operate on a larger scale than PCAs and air-plasma sources and are based on electron accelerators. Electrons are accelerated to relativistic energies and then passed through magnetic undulators, which cause the electron beam to wiggle and emit THz radiation [60]. One major advantage of FELs is their wide tuning range, high pulse repetition rate, and strong THz power. Most FELs are open-user research facilities where various research topics can be pursued. Examples of THz FELs include ELBE and TELBE in Germany and the UCSB Center for Terahertz Science and Technology in the United States.

1.3 THz-Detection

Detecting THz radiation is a challenging task due to the lack of low bandgap materials and high levels of thermal noise in standard semiconductor devices. However, various techniques have been developed to detect radiation in the THz frequency range. The following section will explain the most important techniques used in this thesis.

1.3.1 Electro-Optic Sampling

Electro-optic (electro-optic (EO)) sampling is widely used to characterize THz pulses. The technique delivers precise information about the amplitude and phase of the signal [61]. EO-sampling is based on the EO-effect (Pockels-effect) in non-centro symmetrical media such as ZnTe or GaP. The Pockels effect is the change in the refractive index of a material when an external field is present. The change in the refractive index depends on the applied field strength and the EO-coefficients of the material. This effect results, as OR, from the above-mentioned nonlinear polarization $P^{(2)}$. The EO coefficient r for a given medium is directly related to the effective non-linear coefficient d_{eff} through [26]

$$r = -4\frac{d_{eff}}{n^4}\,. \tag{1.26}$$

The change of refractive index due to the external field is not uniform along all crystal axes, resulting in birefringence. If linear polarized light is transmitted through the material, the different parts of the electric field experience different refractive indices, causing a phase retardation Γ. As a result, the polarization of the light changes from linear to elliptical. The degree of ellipticity is proportional to the strength of the external field. This effect can be used to detect the electric field of a THz pulse. Therefore, we assume that the THz pulse varies much slower than the time duration of the optical probe pulse so that the THz field can be assumed as static, seen from the probe pulse perspective. Then the THz pulse changes the polarization of the optical pulse from linearly to elliptically polarized. A polarization-sensitive detection scheme is then to be used to analyze the change.

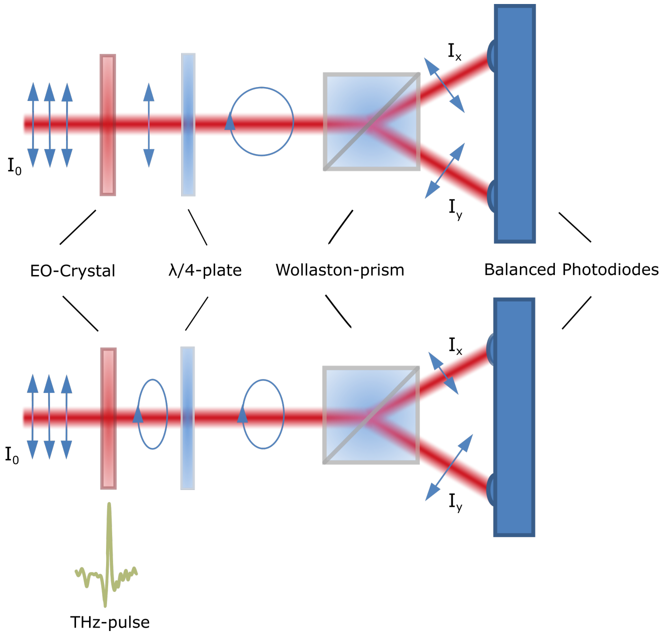

Figure 1.3. Basic Principle of EO-sampling. The THz pulse induces birefringence into the EO-crystal, which changes the polarization of the probe beam. The displayed detection scheme measures the difference in intensity in different components of the polarization.

In the experimental setup (see figure 1.3), the probe-beam is propagating with the intensity I_0 through the EO-crystal, after which a $\lambda/4$-plate is placed. Without a THz-pulse, the linear polarization of the probe beam is not changed by the EO-crystal, and the $\lambda/4$-plate turns the polarization from linear to circular. A Wollaston prism is then used to split the probe pulse equally into the two polarization I_x and I_y. Each part is detected by a separate photodiode. The signals on the photodiodes are given by [29]

$$I_x = \frac{I_0}{2}(1 - \sin\Gamma) \approx \frac{I_0}{2}(1 - \Gamma), \quad I_y = \frac{I_0}{2}(1 + \sin\Gamma) \approx \frac{I_0}{2}(1 + \Gamma) \tag{1.27}$$

The approximation of $\sin\Gamma \approx \Gamma$ is only valid for small Γ's for which the sine can be approximated as linear. The difference signal of the diodes is the measured signal by the data acquisition tools such as Lock-In amplifiers or Box-car integrators. Without a THz pulse, the signal on both diodes should be equal and, therefore, of minimal difference. This detection scheme is called balance detection. To balance the photodiodes, the $\lambda/4$ plate is rotated so that the probe pulse is perfectly circularly polarized. If the THz pulse and the probe-pulse incident together onto the EO-crystal, the slow electric field of the THz causes a phase-retardation of one polarization direction of the probe-pulse. The $\lambda/4$-plate does not change the polarization back to perfectly circular, which results in an unbalancing of the photodiodes. One diode measures a higher intensity than the other. The difference is the measured signal.

$$I_s = I_x - I_y = I_0\Gamma \tag{1.28}$$

Due to the slow change of the THz electric field, the change in refractive index corresponds to the THz field strength at a specific point in time. The full THz waveform can be retrieved by changing the time delay between the THz and the probe pulse.

If the probe beam incidence is perpendicular to the $\langle 110 \rangle$- crystal plane of a crystal with zinkblade structure, the phase retardation due to the induced birefringence is given by [62]

$$\Gamma = \frac{\pi d}{\lambda_0} n_0^3 r_{41} E_{THz} (\cos\alpha \sin 2\phi + 2\sin\alpha \cos 2\phi) \tag{1.29}$$

Here, λ_0 is the wavelength of the probe beam in a vacuum. d, n_0, E_{THz} and r_{41} are the thickness, the refractive index for the probe pulse without THz-field, and the EO-coefficient of the EO-crystal, respectively. α is the angle between the [001]-axis and the polarization of the THz field and ϕ is angle of the probe beam polarization to the [001]-axis. Consequently, in the experiment, the probe and the THz polarization must be aligned to each other ($\alpha = \phi$ or $\phi = 90^\circ + \alpha$) and to the EO-crystal orientation to measure the full THz electric field strength. As one can see from equation (1.29) and equation (1.28), the detection sensitivity increases with the thickness d of the crystal. However, it is to mention that for EO-sampling also, the phase-matching conditions must be fulfilled between the probe and THz pulse in the EO-crystal. Due to the mismatch in real crystals, the detection bandwidth decreases for thicker crystals.

1.3.2 Other Detection Methods

There are several methods for detecting THz radiation besides EOS. Microbolometer arrays and pyroelectric detectors are two additional detection strategies that were commonly used during the experimental phase of this thesis preparation. In this subsection, the basic operating concept of both detectors is briefly presented. Both techniques are thermal detection schemes and hence are not coherent.

Microbolometers are frequently utilized for infrared imaging and have been modified to detect THz waves by altering the materials and absorption layer's structure. They are some of the most frequently employed approaches for THz detection in commercial cameras [63]. The working principle is based on a change in the electric resistance of an absorptive layer induced by the THz radiation. This change is measured [64]. Microbolometers have a high sensitivity, high resolution, and wide bandwidth, and they can function at room temperature [65]. However, they have a poor response time and require complicated reading circuits. In this thesis, microbolometers are used in the form of a THz-camera to measure the beam profile of the THz beam and for alignment purposes.

Pyroelectric detectors are often employed for THz power-measuring applications due to their ability to operate at ambient temperatures with high sensitivity. Thermal changes caused by the THz radiation are detected due to a change in the detector's material's electrical polarization as the temperature rises, which leads to a potential difference across the material [66, 67]. Nonetheless, pyroelectric detectors have a low signal-to-noise ratio, and background signal subtraction is important for achieving quality measurements. All THz power measurements in this thesis are performed by pyroelectric detectors.

1.3.3 Field-Strength Calibration

At the end of the chapter about THz science and techniques, methods to calibrate the electrical field strength of the THz pulse are introduced. Two different methods are discussed. The first method is based on the correlation between the field-induced modulation of the detected signal during EOS and the field-induced phase retardation in the EO-crystal. For the second method, a calibration factor is derived from the THz spot size, average power, and time dependents. Both methods have their disadvantages which are pointed out in the following.

Calibration by field-induced modulation In section 1.3.1, it is shown how the phase retardation Γ in EO-crystal causes unbalancing of the photodiode (PD)s. Let us take a look at equation (1.29) with $\alpha = \phi = 90°$ and equation (1.28) leading to

$$\Gamma = \frac{I_x - I_y}{I_0} = \frac{2\pi d}{\lambda_0} n_0^3 r_{41} E_{THz} \tag{1.30}$$

From this equation, we can see that the measured intensities can be used to calculate the peak electric field E_{THz} of the THz pulse if d, n_0, r_{41}, and λ_0 are known for the used EO-crystal.

This method provides a direct measurement of the peak field based on only the PD signals and physical constants. However, due to the assumption made in equation (1.27) that Γ is small, this method for calculating the field strength requires significant attenuation of the THz field. Moreover, poor alignment of the probe and THz beams to each other can affect the field calibration significantly. This considers the overlap of the beams in the crystal but also the polarization orientation to each other and the crystal. Additionally, measured modulation of the PDs dependent on the pulse width. When applying EOS to measure the field, a negligible probe pulse duration compared to the THz pulse width is assumed. However, in many cases, the probe pulse is heavily chirped, leading as well to an underestimation of the field [68].On the other hand, for too short probe pulses, the refractive index n_0 cannot be assumed to be constant due to the high bandwidth. Moreover, equation (1.30) assumes a perfect crystal. However, in reality, the crystals have defects and might be strained, which alternates the crystal properties. Due to those and other uncertainties, the modulation of the photodiodes delivers an underestimated field strength of the THz pulse.

Calibration through power and spot size measurements By measuring the average power P, the 2D-spot size $\sigma_x,\ \sigma_y$ ($1/e^2$-radius), and time trace $E_{raw}(t)$ of the THz pulse, a scaling factor κ for time trace can be determined when a Gaussian beam is assumed by [32]

$$\kappa = \sqrt{\frac{2P}{\pi c \epsilon_0 f_{rep} n \sigma_x \sigma_y \int E_{raw}^2 \mathrm{d}t}} \tag{1.31}$$

with f_{rep} the repetition rate of the laser. This calibration is derived via the integration of the spatial Gaussian intensity in time and space.

This technique has the advantage that the calibrated field is less dependent on the alignment of the EOS detection scheme because even for an imperfect alignment, the time evolution of the field is properly measured. Moreover, this method is more robust for strong fields. In the case of a strong THz pulse, the EOS signal might be nonlinear. However, due to the measurement of the average power, the energy contained in the THz pulse is still measured and only a small underestimation will occur. Nevertheless, the technique relies on accurate measurements of the average power and spot size of the THz pulse. Commonly used THz cameras do not have a flat spectral response in the THz range, which favors higher frequency contents in the pulse. This causes an underestimation of the measured spot size and, thereby, an overestimation of the THz field. Moreover, the average power measures the total power included in the time evolution of the pulse. However, if only a short (in time) EO trace of the pulse is measured, the field will be overestimated, especially when the setup is not purged.

In this thesis, the electric field strengths of the THz pulses are calibrated by the second method.

CHAPTER 2

Electron Field Emission

The observation of electron emission for metals can have numerous underlying mechanisms, such as thermal, photoelectric, or field emission.

In the case of thermal emission, also called thermionic emission, the material is heated, and that way, the electrons gain enough energy to overcome the work function of the material and leave it.

The photo-electric effect is as well based on energy transfer from the photo to the electrons in the metal. If the photon energy is higher than the work function of the metal, the transferred energy from the photon to the electron leads to the emission of it. For a light source with low intensity, the energy of a single photon must be higher than the work function to emit an electron successfully [69]. However, for high-intensity light sources, multiphoton can occur, meaning that multiple photons can transfer their energy to a single electron so that the sum of the photon energies is higher than the work function [70].

For low-energy radiation such as THz light, the process of photo-electric emission due to multiphoton absorption is highly unlikely. However, it is observed that strong THz fields can cause electron field emission [71]. In contrast to the two previously mentioned emission processes, field emission does not rely on energy transfer to the electrons in the metal. Hence it is also known as cold field emission. The wave nature of the electron becomes important. The light field bends the energy barrier with the height of the work function, which allows the electron to tunnel quantum-mechanically into free space. In 1928, Fowler and Nordheim described the process of electrons tunneling out of metal in an intense electric field through a triangular barrier [5]. Since then, cold field emission is often referenced as Fowler-Nordheim (FN) like emission. The FN-equation describes the tunnel current density J for an electric field F applied to a metal surface

$$J = a_n \frac{F^2}{\phi} \cdot \exp\left(\frac{-b_n \phi^{3/2}}{F} \right) \tag{2.1}$$

with a_n and b_n as the first and second FN-constants. ϕ is the work function of the metal.

In this chapter, the FN theory is discussed in more depth, which is crucial for the research conducted in this thesis. The chapter begins with a qualitative discussion of the field emission process, followed by a more mathematical derivation method. The potential barrier shape adjustments are then examined, and a comment is made on the linearisation of the FN plots. The importance of the Keldysh parameter for determining ionization regimes is also discussed. Finally, this chapter introduces the field emitters used in this thesis, providing the fundamental knowledge required to understand the experiments conducted.

2.1 Mechanism of Cold Field Emission

Field emission can not only take place from metal, but also other materials show electron emission if exposed to strong fields. This includes semiconductors [72], 2D materials [73], molecules [74], and even single atoms [75]. However, in the following, only the case for field emission from metallic surfaces is discussed due to its relevance to the here presented thesis.

A simple model for electrons in a metal is the free electron model, in which the electrons can be seen as free electron gas [76]. For the one-dimensional case, the electrons do freely move around along a line in a potential well with the potential function $U(x)$. The electrons obey the Pauli exclusion principle so that the energy levels can only be filled by two electrons with opposite spin states. The highest filled energy level is called n_F. For a temperature of $0\,\mathrm{K}$, this is the Fermi Energy E_F. An increase in temperature leads to the filling of an energetically higher state and vacating of an energetically lower state. This is described by the Fermi-Dirac distribution function. For $T = 0$, the Fermi-Dirac distribution is a step function going from 1 for lower energies than E_F to 0 for higher energies than E_F. For $T > 0$, the distribution smears out. The electrons at E_F get excited to a higher energetic state. The energy of the highest occupied state is called the Fermi level. The potential barrier $U(x = 0)$ prevents the electron from leaving the metal with a common height of around $5\,\mathrm{eV}$. The potential should have the following form:

$$U(x) = \begin{cases} U_{vac} & \text{for } x \geq 0 \\ E_F & \text{for } x < 0 \end{cases} \tag{2.2}$$

The energy to overcome U_{vac} and access the vacuum state is the work function ϕ. It is defined as the energy needed to remove an electron from the material (Gold: $\phi_{Au} = 5.1\,\mathrm{eV}$ [77]). Without external energy application by heating (thermionic emission) or shining light onto the metal (photoelectric emission), the electrons can not leave the metal because of too little energy. Also, the wave nature of the electrons does not allow them to tunnel through the barrier. The barrier is infinitely thick.

However, if an external field F is applied to the metal surface, the barrier shape is modified. Here, it should be mentioned that in field emission theory, the convention is that F denotes the extracting field and is always positive [78], while in conventional electrostatic static for positive fields, the barrier increases but in negative fields, the barrier shape is tilted. If F is high enough, the barrier reaches a defined distance down to E_F, meaning that the electrons at the Fermi level can tunnel with a certain probability through the barrier. The higher F, the thinner the tilted barrier becomes and the more likely a tunneling event will happen. The tunneling does occur from the electrons close to the Fermi level. For this here discussed scenario, the barrier shape would be triangular due to the reduction of F. The number of electrons tunneling through the barrier can be described by the FN-equation which is discussed in the following.

2.1.1 Fowler-Nordheim Theory

The derivation of the FN-equation follows from the consideration of the current density J through the barrier when viewing the electrons as free electron gas and the description of the electron as a wave. J can then be expressed as [79]

$$J = \int N(E_x) D(E_x) \mathrm{d}E_x \quad \text{with} \tag{2.3}$$

$$N(E_x) = \frac{e m_e k_B T}{2\pi^2 \hbar^3} \ln\left(1 + \exp\left(-\frac{E_x - E_F}{k_B T}\right)\right), \tag{2.4}$$

$$D(E_x) = \exp\left(\frac{-b_n \phi^{3/2}}{F}\right) \exp\left(\frac{E_x - E_F}{d_F}\right) \tag{2.5}$$

where $N(E_x)$ is the supply function for the electrons determined for the Fermi-Dirac-distribution of the electrons and $D(E_x)$ is the transmission probability through the triangular barrier. To describe the tunneling through the triangular barrier, R. H. Fowler and L. Nordheim solved the Schrödinger equation for an electron [5].

$$\frac{\mathrm{d}^2\psi}{\mathrm{d}x^2} + \kappa^2 (E_x - \phi + eFx)\psi = 0 \qquad \text{for } (x > 0), \tag{2.6}$$

$$\frac{\mathrm{d}^2\psi}{\mathrm{d}x^2} + \kappa^2 E_x \psi = 0 \qquad \text{for } (x < 0), \tag{2.7}$$

ψ, E_x, and x are the electrons' wavefunction, energy, and location measured from the well edge, respectively. κ is defined by $\kappa^2 = 8\pi^2 m_e / h^2$. For $x = 0$, continuity of ψ and $\frac{\mathrm{d}\psi}{\mathrm{d}x}$ must be given. For the later discussion, it should be mentioned that $M(x) = \phi - eFx$ describes the triangular barrier shape. Those equations can be solved by applying Airy-functions for ψ [80], which leads to the transmission coefficient $D(E_x)$. For zero and low temperatures (room temperature is here considered as low), the final solution is the FN-equation:

$$J = a_n \frac{F^2}{\phi} \cdot \exp\left(\frac{-b_n \phi^{3/2}}{F}\right) \tag{2.8}$$

The first and second FN-constants are:

$$a_n = \frac{e^3}{16\pi^2 \hbar} \approx 1.541 \cdot 10^{-6} \mathrm{AeV/V^2} \tag{2.9}$$

$$b_n = \frac{4(2m_e)^{1/2}}{3e\hbar} \approx 6.831 \cdot 10^9 \mathrm{eV^{-3/2}Vm^{-1}} \tag{2.10}$$

For a more complete derivation, [5, 78–80] should be consolidated. The aim here is only to show the physical origin of the FN-equation.

The assumption made for the derivation of equation (2.8) are the following [79]:

1. The electrons behave like a free electron gas and obey the Fermi-Dirac statistics

2. The emitter's surface is planar, smooth, and flat
3. The local work function ϕ is homogenous over the emitter's surface
4. The electric field F is uniformly applied over the surface
5. The potential barrier shape is triangular
6. The emitter is located in a vacuum

For metallic emitters, especially for noble metals, the Sommerfeld description of electrons as electron gas and description by Fermi-Dirac statistics is valid and led to sufficient good agreement with experimental data [76]. In most cases, the smooth surface is only an approximation due to fabrication errors of the emitters. Those errors then affect the local field distribution and the local work function ϕ. ϕ is also not necessarily stable as measurements of the local work functions by applying scanning tunneling mircroscope (STM) spectroscopy reveal. The local work function is dependent on the cleanliness of the sample as well as the environment [81]. It is lower in the air than in the vacuum [15].

The limit due to the triangular barrier shape is discussed separately in the subsequent paragraph.

2.1.2 Potential Barrier Shape for Fowler-Nordheim-Type Emission

The standard FN-equation applies an exact triangular-shaped potential barrier through which the electrons tunnel and the wave equations in equation (2.6) are solved for it. The exact triangular barrier has the mathematical form of

$$M_{ET}(x) = \phi - eFx \tag{2.11}$$

Already in their publication in 1928, Fowler and Nordheim mentioned that the real barrier shape is not a perfect triangular one; instead, the barrier is rounded at the top due to image charges. However, the rounded barrier is not considered in the original derivation. The Schottky-Nordheim (SN)-barrier takes the image charges into account and corrects the barrier shape accordingly, which leads to rounding off of the triangular barrier [82]. The expression for this barrier is given by

$$M_{SN}(x) = \phi - eFx - \frac{e^2}{16\pi\epsilon_0 x} \tag{2.12}$$

the leaving electron adds its image potential to the external field, which leads to a reduced location-dependent potential barrier. Solving the wave equation for the new potential results in [83]

$$J = a_n \frac{F^2}{\tau_F^2 \phi} \cdot \exp\left(\frac{-b_n \nu_F \phi^{3/2}}{F} \right) \tag{2.13}$$

with the Schottky correction factors τ_F and ν_F, also called special field emission elliptical functions [84]. A series expansion of the elliptical functions leads to good approximations [85].

$$\nu_F(f) \approx 1 - f + \frac{f}{6}\ln f, \tag{2.14}$$

$$\tau_F(f) \approx 1 + \frac{f}{9} - \frac{f}{18}\ln f \tag{2.15}$$

f is the scaled field for a barrier height of ϕ when no external field is applied. In can be expressed by:

$$f = \frac{c_s^2}{\phi^2}F\,, \quad c_s = \left(\frac{e^3}{4\pi\epsilon_0}\right)^{1/2} \tag{2.16}$$

c_s is the Schottky constant. The values of ν_F range from 0 to 1, while τ_F stays close to 1. However, in experiments, τ_F is difficult to quantify because other effects, such as surface roughness of the emitter, influence the scaling more than τ_F. Hence, a linear scaling factor is proposed taking many effects into account [86]. Theoretically, the SN-barrier is physically more correct than the exact triangular barrier. As a consequence, the standard FN-equation, as shown in equation (2.8), predicts a lower current density by a factor of several hundred [85].

2.1.3 Linear Fowler-Nordheim Plots

It is common practice to analyze the measured field emission curves by transforming the axis of the plot to $x = ln(J/F^2)$ and $x = 1/F$ to observe a linear dependency of x and y. Considering a reduced form of the FN-equation

$$J = C \cdot F^2 \exp(-B/F) \quad \Leftrightarrow \quad J/F^2 = C\exp(-B/F) \tag{2.17}$$

and taking the logarithm of both side lead to

$$\ln\bigl(J/F^2\bigr) = \ln(C) - B/F \quad \Leftrightarrow \quad \ln\bigl(J/F^2\bigr) = -B \cdot 1/F + \ln(C) \tag{2.18}$$

It is easy to see the linear equation of the form $y = mx + k$. Comparison to the FN equation in 2.8 direct to the following expressions for the coefficients:

$$x = \frac{1}{F}, \quad y = \ln\left(\frac{J}{F^2}\right), \quad m = -b_n\phi^{3/2}, \text{ and } \ k = \ln\left(\frac{a_n}{\phi}\right)$$

For experiments as performed here in this thesis, the theoretical field F is exchanged by the amplitude of real field E and a field enhancement factor β multiplied by the field. This leads to the ensuing expression of $y = mx + k$.

$$x = \frac{1}{E}, \quad y = \ln\left(\frac{J}{E^2}\right), \quad m = \frac{-b_n\phi^{3/2}}{\beta}, \text{ and } \ k = \ln\left(\frac{a_n\beta^2}{\phi}\right)$$

As one can see, m is the slope of the line plot, which can effortlessly be extracted by fitting it. For a known ϕ, a value for the field enhancement factor β can be calculated or for a know β, ϕ is accessible.

However, this procedure is always based on knowing one or the other, which is, as discussed above, not trivial. The work function is environment-dependent, and β is dependent on the emitter structure, which can be roughly estimated by simulations. However, structural imperfection of the emitter can cause deviations from the simulation. Moreover, the barrier shape is unknown and would also be part of the slope m if substituting equation (2.13) into equation (2.18). Hence, the linearity of the FN-equation does only indicated that the underlying electron emission process is FN-like but does not provide significant information about the detail of the tunneling process as barrier shape, field enhancement factor or work function as long as the other two variables are unknown.

2.1.4 Keldysh Parameter

So far, when talking about the field emission process, the electric field was considered to be a constant or slow-varying field. However, in this thesis, fields oscillating with THz frequencies are employed for the field emission, which opens the question if tunneling can even appear if the barrier is tilted for only a short time or if multiphoton dominates the emission process. The Keldysh parameter gives information about the adiabaticity of the ionization process and indicates whether the process is located in the weak- or strong-field regime of light-matter interaction [87]. The Keldysh-parameter has the form following from [88]

$$\gamma = \frac{\omega\sqrt{2mI_0}}{eF} \tag{2.19}$$

where ω, I_0, and F are the frequency of the light field, the ionization potential, and the electric field strength, respectively. For metals, the work function and the ionization potential are considered equal. Keldysh illustrates in [88] that for low frequencies ω and very strong fields F, meaning $\gamma \ll 1$, the ionization probability turns out to be the same as the tunnel-auto ionization of atoms, while for weak fields and high frequency ($\gamma \gg 1$), the multiphoton absorption dominates.

In the strong field THz regime, the value of the Keldysh parameter is typically much smaller than 1. This suggests that the experiments in this thesis, which involve the application of THz fields, are dominated by field emission processes. The THz-induced field emission can be considered quasi-static. For the experiments applying mid-IR radiation, the frequencies are higher, but also, here, the Keldysh parameter indicates the experiments are in the field emission regime.

2.2 Field Emitters

The field emitters used for the research in the here presented thesis are metallic micro antennas fabricated by means of optical lithography in the cleanroom of the Technical University of

Denmark (DTU). The type of emitters was investigated by S. Lange during his studies at DTU [89,90]. The single emitter is a double split-ring resonator (dSRR), which is a resonant structure with two well-defined main resonances [14]. An optical microscope image of dSRR applied in the studies of [89] is displayed in figure 2.1 a). Similar structures are used in the studies presented in chapter 3.

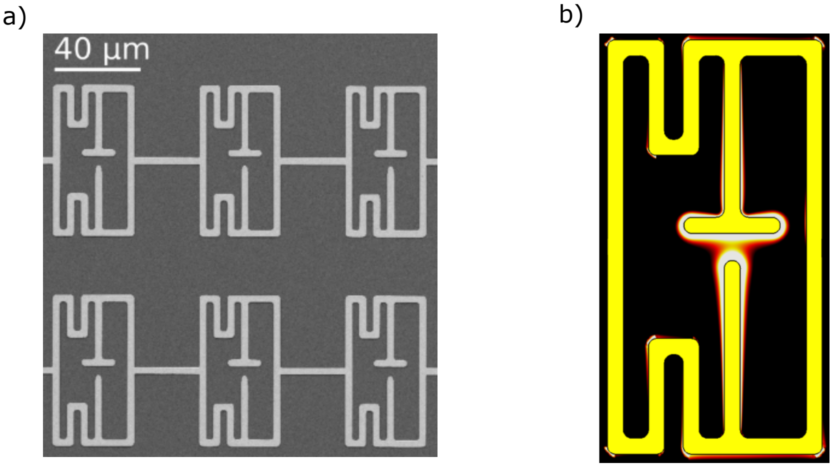

Figure 2.1. Images of the dSRR. In a), the dSRRs applied for the investigation in [89] are displayed. In b), a finite element simulation of the field distribution of a dSRR, when illuminated with THz radiation, is shown. One can see that the field is enhanced in the gap region of the emitter. The pictures are taken from [89] with the permission from S. Lange.

The most basic antenna is a dipole that is tuned to a given wavelength. Illumination with this wavelength results in increased field strength at the dipole tips. Bending this dipole into a ring with both tips facing each other results in an enhanced field in the gap region. The resonance of the split ring is the same as that of the dipole. Adding a second ring of varying length to the resonator creates a second resonance, forming the dSRR. In this thesis, the used dSRR are designed so that the resonances align with the spectrum of the utilized THz pulses.

The resonant nature of the emitter increases the electric field locally by a factor of several hundred, as finite element simulations indicate. As an example, a finite element simulation of the field distribution of a dSRR is depicted in figure 2.1 b). The field enhancement factor is in this thesis labeled with β and plays an important role in the field emission process.

The emitters are arranged in an array. Due to the size of the dSRRs and the wavelength of the THz pulses, the array of emitters is considered a metasurface and will be referenced as such in this thesis when speaking about the emitter array. A metasurface is a periodic or aperiodic structure formed from elements that are smaller in size than the wavelength used for the application [91].

Photolithography is applied to fabricate the dSRR on top of double-side polished high-resistivity float zone silicon chips. In the following, we refer to it simply as Si-chip. Most of the applied antennas have a metal thickness of about $210\,\mathrm{nm}$ where $10\,\mathrm{nm}$ 10 nm is a titanium adhesion layer and the remaining $200\,\mathrm{nm}$ is gold.

Part II

Experimental Techniques and Results

CHAPTER 3

Electron Triggered Reactions in Liquids and Gases

3.1 Introduction

In this chapter, the outcomes of the direct injection of field-emitted electrons into liquids and gases are presented. Furthermore, the possibility of additional electron emission due to direct field ionization of the molecules of the liquid is discussed. Moreover, a simulation of electrons in argon gas is presented.

In previous studies, field-emitted electrons from metal surfaces into the vacuum were characterized and matched with the FN theory. In a vacuum, the electron gets accelerated in the electric field without colliding with any other molecule causing the electrons to gain energies of several keV [12, 13]. The final energy depends on the field strength of the THz-pulse and field enhancement at the electron-releasing surface.

In the past years, researchers from the Ultrafast Infrared and Terahertz Science group at DTU have shown that electron field emission with THz pulses is possible when the emitter is placed outside a vacuum and that the emitted electrons can trigger reactions. The employed emitters were metasurfaces consisting of micro antennas [89, 92, 93].

Even in a nitrogen gas environment, the electrons can gain enough energy to excite and ionize the molecules leading to the emission of ultraviolet (UV) light due to the relaxation of the molecule to the ground state. The emitted light was measured by a photo-multiplier-tube (PMT), and the UV-spectrum gives information about the transitions involved in the process. Simulations could confirm and reproduce the experimental data. The associated energies of the electrons in this experiment were about $100\,\mathrm{eV}$ for a peak electric field strength of $200\,\mathrm{kV\,cm^{-1}}$ [92].

Taking that further, the metasurfaces were covered by a dielectric polymer (DP); that way, the electrons are emitted and accelerated directly in the solid. Two different detection schemes for the successful emission and acceleration in the solid were employed. First is using a DP which changes its properties due to electron impact. Therefore, electron-beam resist was used. The experiment showed that the developer dissolved the resist at the high-field regions of the metasurfaces where possibly the electrons were emitted. However, whether the field or the electrons caused the change in the DP was not resolved. The possibility of structural change in the resist due to field enhancement was shown before in [94]. Hence, a scintillating dye-doped DP sensitive to electrons was applied. As before, in the gas, the emitted light from the DP was detected and confirmed that the electrons trigger the scintillating molecules in the dye. Also here, amonte-carlo (MC)-simulation was in good agreement with the experimentally recorded data. The MC-simulation obtained energies for the electrons in the DP in an interval from $100\,\mathrm{eV}$ to $600\,\mathrm{eV}$ for a maximal free space THz field strength of $300\,\mathrm{kV\,cm^{-1}}$ [89, 93].

In addition to the experiments conducted at DTU, field emission has been investigated by other researchers in various media. For instance, a study examined electron field emission (not THz driven) from sp^3-bonded 5H-BN microcones in air [95]. The researchers observed a glow discharge and discussed whether the dissociation and ionization of the molecules were responsible for it. Another study, conducted by Park et al. [96], explored the effect of electron impact on electron beam resist, similar to the experiment performed at DTU. In this experiment, a bowtie antenna was coated with resist and exposed to a THz beam. Polymerization of the resist was observed and attributed to field emission. Their argument is based on current measurements, electron dose calculations, and a good match between the field emission data and simulations.

Those experiments explored the possibility to field emitting electrons into the gaseous and the solid phase of materials. The obviously missing phase is the liquid phase. Compared to a solid material, the molecules are not static, and the density of a liquid is generally higher than the one of gases. Moreover, the density of many polymers ranges around the one of water ($1\,\mathrm{g\,cm^{-3}}$). The higher density and the movement of the molecules in a liquid opens the question of whether directly injecting an electron into a liquid through THz-driven field emission is possible or if the electrons are immediately stopped due to collision and solvation. It was observed that hot electron emission into water is feasible [97]. Also, field emission experiments with electron emission into dielectric liquids with static fields have been performed before [98, 99]. However, direct THz-driven field emission from metal antennas into a liquid is so far, to our best knowledge, not reported.

The direct THz-driven electron emission from the metasurfaces into a liquid could provide the stepstone for a new experimental technique to perform pulsed radiolysis experiments with relatively low-energy electrons. This is important because the free electron does not exist long in ambient conditions before reacting with other species. Depending on the electron's energy, different reaction paths can be triggered. Low-energy electrons (0-20 eV) can be involved in dissociative electron attachment, which is the dissociation of molecules into fragments due to the attachment of the electron [100]. This leads to the creation of a free radical, a highly reactive species. In water, the low-energy electrons split the molecule into ions, which are reactive as well. Studies have shown that those ions cause damage to the DNA solvated in water [101]. Higher electron energies, around 70 eV, are utilized in mass spectrometry for electron ionization. The exact ionization energy is dependent on the molecule or atom in question, but 70 eV leads with a high probability of ionization [102]. Ionization can lead to dissociation into fragments [103, 104]. Moreover, the study of the time evolution of the electron's solvation in liquids, especially in water, is highly important. During the solvation process, the electron is believed to contribute to reactions such as radiation damage of the DNA [105], aerosol formation in the upper atmosphere [106], or cataclysm of ammonia generation [107].

Those electron-triggered events happen in tens of femtoseconds up to picoseconds. [108–110] To investigate such fast processes with ultrafast spectroscopy, the exciting electron pulse must be shorter than the event to observe. To generate such short electron pulses with low energy is challenging. The direct injection of the electrons into the sample solves this problem.

For this purpose, the field emission of electrons into liquids is investigated in the following. Experiments on liquids doped with a fluorescent dye were performed to answer the question of the possibility of THz field emission into liquids. The fluorescent dye gives the opportunity to detect the electrons due to the emitted light. The idea is the same as for the gas or solid-state of materials shown above. Firstly, the experimental methods are introduced. Afterward, the measured results are presented and discussed. Lastly, a simulation of the emission process will be shown and compared to the measurements.

3.2 Methods

The experimental implementation of the investigation will be laid out in this section, in addition to assessing the gaseous and liquid substances utilized.

3.2.1 Experimental Setup

The experimental setup utilizes a LN-based THz source as described in section 1.2.3. After rapid expansion and collimation, the THz-beam is propagated onto a 2-inch OAP with a focal length of 2 inches. The THz beam fills most of the OAPs reflective surface, allowing tight focusing of the THz beam. This results in a $1\backslash\mathrm{e}^2$-width of $w_x = 0.661\,\mathrm{mm}$, $w_y = 1.119\,\mathrm{mm}$, determined by a two-dimensional Gaussian fit to the measured intensity distribution of the beam, measured by an uncooled microbolometer (NCE, IRV-T0831) with pitch size of $23.5\,\mathrm{\mu m}$.The observed ellipticity in the spot size is most likely due to a slight misalignment of the focusing OAP or the collimating OAPs in the expanding telescope. However, this astigmatism should not affect the here performed measurement. It limits the acquired field strength, but the THz beam after illumination of the metasurface is not further analyzed. The THz beam is focused onto the backside of the Si-chip of the metasurface. The Si-chip forms the front window of the transmission cell. By doing so, the metasurface is directly submersed in the gaseous or liquid sample, providing direct contact. The rear window of the cell is formed by a Quartz plate, ensuring a good transmission of the emitted visible light to the detector. The transmission cell can hold several milliliters of the substance of interest and is designed specifically for this experiment. The detector for the emitted light is in direct and light-tight contact with the outer frame of the liquid cell. The applied detectors are a charge-coupled device (CCD)-camera (Lumenera, Infinity 3) for imaging the emission regions of the metasurface via a microscope objective with 20x magnification and a PMT (Hamamatsu, R2496) to detect the overall emitted light intensity from the samples (see section 3.2.1 c)). The DAQ-system for the PMT as detector is realized through a boxcar integrator (SRS, SR250) and a DAQ-card . The boxcar integrator is triggered from the lasers' delay generator. An oscilloscope is used to fine-adjust the delay between the gate and the PMT signal. To control the impinging THz field strength, two wire grid polarizer (WGP) are used to adjust the transmitted field continuously. Therefore, the first WGP is mounted in a motorized rotation stage, while the second one maintains a fixed orientation to pass all THz-radiation which has a polarization parallel to the tabletop of the optical table. The rotation of 0° of the first WGP is defined to give full transmission, while 90° means that the WGPs are cross-polarized and no THz is transmitted. A schematic of the experiment, including the DAQ system, is depicted in section 3.2.1 a).

The WGP and the DAQ system are computer controlled by a home-built Python code to interface with the instruments. At the beginning of the experiments, we developed a graphical user interface. However, we moved away from that due to limited flexibility for the integration of new instruments and measurement procedures. To record the time traces of the THz-pulse, EOS is applied. Therefore, the focusing OAP is bypassed, and the THz beam is focused by an independent OAP onto the EO-crystal (ZnTe, $1\,\mathrm{mm}$ thickness). As a probe

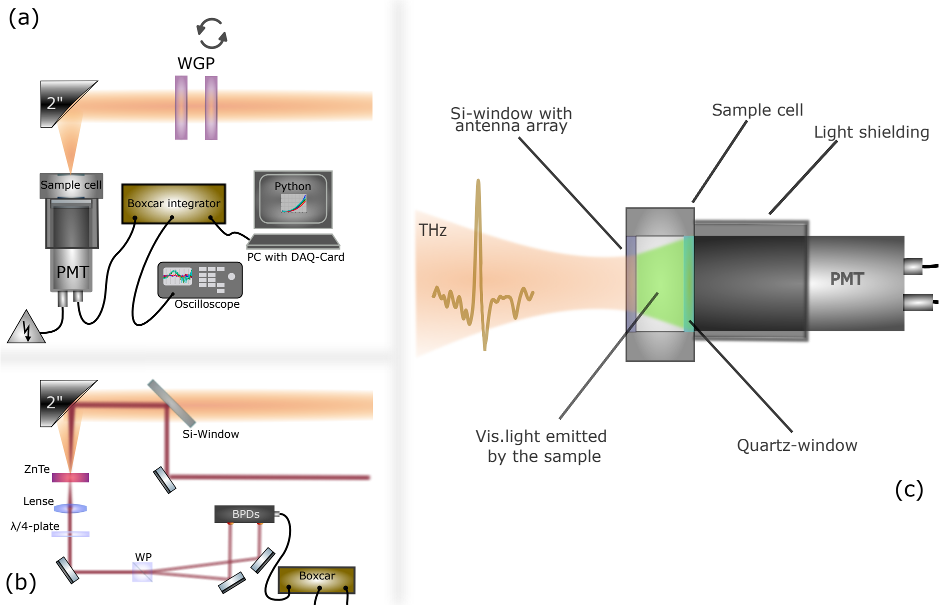
(a)
WGP
2"
Sample cell
Boxcar integrator
Python
PC with DAQ-Card
PMT
Oscilloscope
2"
Si-Window
ZnTe
Lense
λ/4-plate
WP
BPDs
Boxcar
(b)
Si-window with antenna array
Sample cell
Light shielding
THz
PMT
Vis.light emitted by the sample
Quartz-window
(c)

Figure 3.1. Experimental setup for direct electron injection into gases or liquids by means of THz-driven field emission. In (a), the setup, including the data acquisition (DAQ)-system, is depicted. A more detailed view of the sample cell and detection is presented in (c). The applied EOS-setup for measuring the time trace of the THz pulse can be seen in (b).

beam, a small amount from the amplifier output is used. This means that the probing of the THz is performed with the same beam properties as used for the THz generation. This might limit the detection efficiency and bandwidth because the TPF-generation requires a chirped pulse, while for the EOS, an unchirped pulse is preferred. For the realization of the THz-probe overlap, both beams are focused onto the EO-crystal by the same OAP. Therefore, the THz-beam propagates through a 45°-tilted Si-window of which the probe beam reflects off. The probe power has to be low enough so that not too many free charge carriers in the Si get generated, which would screen the THz significantly. A schematic of the experimental realization of the EOS is shown in section 3.2.1 b).

The relevance of the THz time trace in this experiment is to ensure proper THz generation, to gain information about the contained frequency components, and to calibrate the THz-field strength. The latter is achieved by applying equation (1.31) discussed in section 1.3.3. We are aware that applying equation (1.31) can lead to a misestimation of the field strength, as elaborated in section 1.3.3.

3.2.2 Samples

In this study, we investigated 4 different samples, two gases and two liquids doped with a fluorescent dye. The gases are ambient air and Argon (Ar). The employed liquids are ethanol (EtOH) (C_2H_5OH) and silicone oil. It is known that the exited or ionized nitrogen in ambient air emits light in the UV-region [92]. If argon gets exited or ionized, the strongest emission of the discharge spectrum lies in the UV, visible red and near-infrared region of the spectrum [111]; for this reason, argon is chosen. While the nitrogen light emission can only be detected with a PMT, the light emitted by argon can also be detected with a CCD-camera [112]. The selection of EtOH and silicone oil is made based on the polarity of the liquids. The former is a polar liquid, meaning the molecule possesses a non-zero dipole moment caused by the hydroxyl group (OH). In contrast, the silicone oil molecules are neutral, making the fluid non-polar. The chemical structure of EtOH and silicone oil can be seen in figure 3.2 a) and b), respectively. To our best knowledge, EtOH and silicone oil do not exhibit fluorescence in the visible. Studies show that using EtOH as a solvent influences the fluorescence [113, 114], but a study documenting the fluorescence from pure liquids could not be found. However, impurities in the ethanol might induce fluorescence. Nevertheless, any light emission from the samples indicates an induced interaction. Due to the lack of natural fluorescence in EtOH and silicone oil, a fluorescent dye is added to the substances. A suitable dye to be solved in EtOH and silicon oil is the industrial organic dye fluorescent yellow 3G (CAS# 12671-74-8), which exhibits an emission spectrum, as the name already indicates, in the yellow spectral range. Its structural formula is depicted in figure 3.2 (c). We have to take into account that the dye has a purity of 75% which means there are 25% of unknown compounds in it.

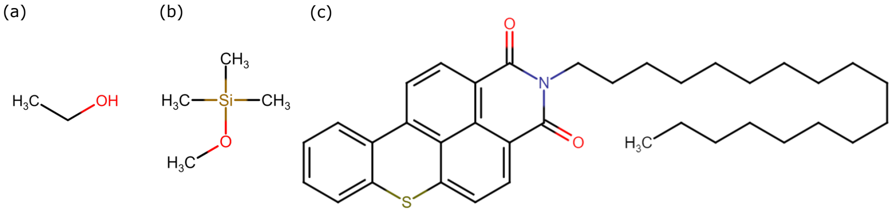

Figure 3.2. Structural chemical formulas of the solvents Ethanol (a) and silicone oil (b) for the fluorescent dye Fluorescent Yellow 3G. The dyes formula is depicted in (c).

Also, the EtOH is never pure; the highest grade is 99%. However, we applied laboratory grade EtOH with a purity of 96%. The impurity of EtOH is water (H_2O), which is a great solvent for EtOH due to the polarity of both molecules. As a consequence of the water residuals, the fluorescence of the dye molecule can be reduced. The water dipole moment couples to exited state of the dye and quenches the emission process. Water can be solved in silicone oil, and hence, there is no quenching expected. There is oxygen in the silicone oil. However, it is tightly bound, which restricts interaction with the dye. Therefore, we expect a stronger signal from the silicone oil due to the absence of oxygen-quenching.

3.3 Measurements

3.3.1 Field Emission in Gases and Liquids

Here, the interaction of the THz field emitted electrons with gases is presented. For Argon as the gas of interest, the sample cell is flowed with the Argon gas, and a constant flow is maintained during the measurement. For ambient air as a sample, the cell is just exposed to the laboratory air. In both cases, the Quartz window is removed to improve the collection of emitted light. First, the CCD-camera acts as a detector for Argon gas. The camera integrates over $500\,\mathrm{ms}$, which is equivalent to 500 THz-pulses impinging onto the metasurface. The recorded picture can be seen in figure 3.3. The peak THz field stregth is $337\,\mathrm{kV\,cm^{-1}}$. Only for the Argon, the camera can be used due to either too little light emission or light in a spectral range where the camera is not sensitive anymore. From the picture, one could extract the beam profile of the THz intensity. We see that, as in the measurements with the bolometer, the spot size is not perfectly round. Moreover, when measuring the spot size based on the CCD camera, it is bigger than measured before. This is expected because the metasurfaces have a narrow band response to THz frequencies of 0.5 THz, while the bolometer tends to be more sensitive to the higher frequency components (> $1\,\mathrm{THz}$). Zooming in on the emission spot of a single antenna, the region of the interaction with the electron and the Argon can be estimated. Therefore, the emission spot is fitted by a two-dimensional Gaussian, and the full-width half-maximum (FWHM) in the x and y-direction are extracted. We find values of $w_x = 45.6\,\mu\mathrm{m}$ and $w_y = 43.6\,\mu\mathrm{m}$. This leads to a radius of about $20\,\mu\mathrm{m}$ in which the electrons stimulate a significant amount of Argon.

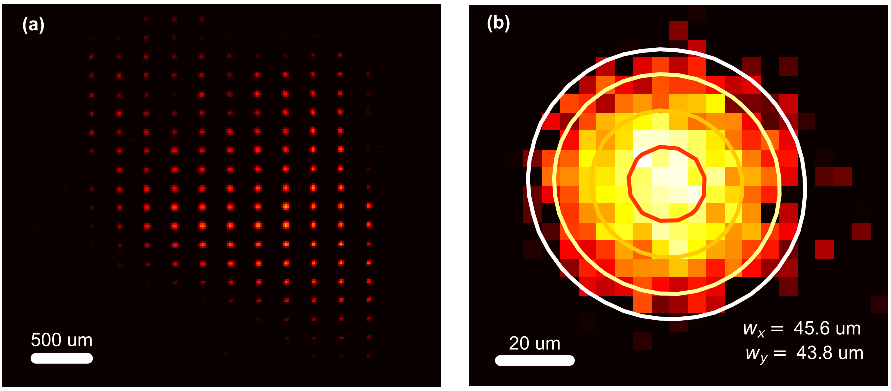

Figure 3.3. Camera image of the illuminated metasurface in Argon gas. The light emission from single antennas is clearly visible (a). Zoom on a high-emission antenna (b). A two-dimensional Gaussian fit provides an interaction radius of about $20\,\mu\mathrm{m}$.

Replacing the camera with a PMT, the field dependence of the emission in Argon and in ambient air is measured. Therefore, the PMT signal is integrated with a boxcar integrator, and the field strength is adjusted by the WGPs. The following formula provides the transmitted field through the WGPs:

$$E(\vartheta) = E_0[\cos^2(\vartheta + a) + b] \tag{3.1}$$

with ϑ as the rotation angle of the first WGP, E_0 as the THz field for $\vartheta = 0°$ and a, b as correction constants for a misalignment of the WGPs in the holders and leaking THz for $\vartheta = 90°$, respectively. $a = 1.94°$ and $b = 0.042$ are determined by fitting an angle-dependent transmission measurement. The THz waveform can be seen in figure 3.4. We show the full waveform with a prepulse $13.9\,\mathrm{ps}$ before the main pulse arrives and the first echo following the main pulse at $10.5\,\mathrm{ps}$. We attribute the echo to the Si-window in the beam path for the EOS. The delay matches well with the window thickness. The prepulse is more difficult to explain. The amplifier doe not produce a significant prepulse which could generate a prepulse that strong. Also, reflected optical pulses in the THz generation crystal would not lead to a prepulse. However, a reflection in the probe pulse could lead to a prepulse by sampling the THz pulse when the delay for the main sampling pulse is before the overlap. For the delay, we calculate a free space delay length of $8.3\,\mathrm{mm}$. In the beam path are absorptive neutral density (ND) filters with a refractive index of 1.5. The length would correspond to a $1.4\,\mathrm{mm}$ thick ND filter, which matches well with the used ND2-fiter. Moreover, the THz pulse shows distortion at the pulse onset, which is not visible in the prepulse. The distance between the echo and the main pulse does not match the prepulse delay. So the overlap between the

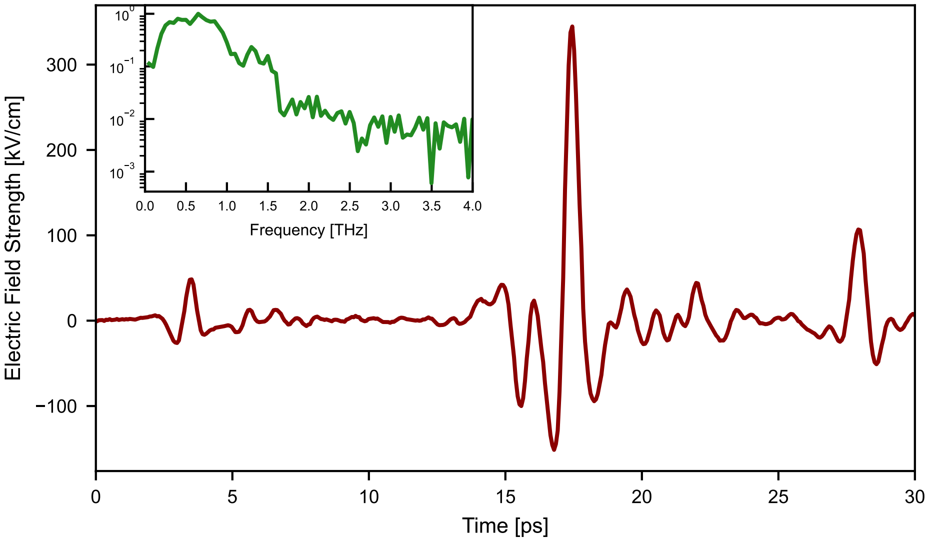

Figure 3.4. THz waveform detected with EO-sampling. The inset illustrates the spectrum of the pule. The waveform includes a prepulse and the first echo from the Si-window in the beam path.

reflected sampling pulse and the echo can be ruled out for causing the distortion. Slight misalignment of the focusing OAP could also lead to a distortion of the pulse shape.

The spectrum of the main pulse peaks at $0.6\,\mathrm{THz}$ as can be seen in the inset of figure 3.4. This means that the peak of the spectrum aligns well with the resonance of the metasurfaces antennas. The field strength calibration of the time trace is performed by applying the second explained in section 1.3.3. The THz-power of $495\,\mu\mathrm{W}$ is measured with a THz-power meter (Gentec-EO, T-Rad, power head: THZ9B-BL-DZ). A silicon window is mounted at the power head to block all residual pump light. Due to that, the measured power and the calibrated field correspond already to the power arriving at the metasurface.

After the THz field is calibrated, the field-dependent response of the metasurface for Argon and ambient air is measured. The integrated PMT response for different fields is displayed in figure 3.5. A gain voltage of $1\,\mathrm{kV}$ for the PMT is used.

As expected, the emitted light from the metasurface increases nonlinearly with increasing impinging THz field strength. The data are fitted with the following FN-fit.

$$I = k \cdot a_n (\beta E)^2 \phi^{-1} \cdot e^{-b_n \phi^{3/2}/(\beta |E|)} + d \tag{3.2}$$

The free parameters for the fit are k as a proportionality constant for the DAQ-system, β as field enhancement factor at the antennas, and d for compensation of any offset due to the DAQ-system. The fit for those free parameters leads to a great match between the data and FN-theory. The residuals of the fit and the data are only fluctuating in the range of noise level (see figure 3.5 b)). However, for a constant work function $\phi = 5.1\,\mathrm{eV}$ [77], β reaches different values for air compared to argon ($\beta air = 2720$, $\beta_{Ar} = 1696$). The discrepancy might be explained by the difference in the ionization energy of the molecules and the gas pressure. Moreover, the assumption of a constant ϕ affects the values of β. As discussed in chapter 2, the environment of the emitter can influence ϕ. By fitting only with the 2 free parameters β and k, the changes of ϕ are included in those parameters. For the FN-plot displayed in figure 3.5 c), the fit is performed without d; otherwise, the expected linearity is not given anymore, as one can see in figure 3.5 d). For high fields, the measurements closely follow a linear trend, but for smaller fields, the data deviate strongly from the theory-suggested values. This is due to the fact that for small fields, no significant amount of electrons are emitted or at least not energetic enough to cause emission from the molecules. The increasing tail for low fields is due to the constant noise level of the DAQ-system. Adding d to the fit is bending it accordingly. In figure 3.5 d), an artificial offset of 10 is added to the data, which leads to a strong deviation from the expected linear plot. This shows the importance of removing an offset in the measurements. Including d in the fit can help to correct the offsets. Besides the mismatch for the low field region, the FN-theory also describes quite accurately the excitation of gases by field-emitted electrons from metallic surfaces.

With the evaluation of the electron-induced light emission from gases and the relation to the FN- theory, we confirmed previous experiments and provided a system to compare the investigations on liquids with. To perform the experiment on the liquid samples, the Quartz window is placed back into the sample cell, and the cell is filled with the samples. A PMT gain voltage of $1.5\,\mathrm{kV}$ is applied. The increase of the gain voltage compared to the gaseous samples originates in the reduced emission of the liquid samples. The measured

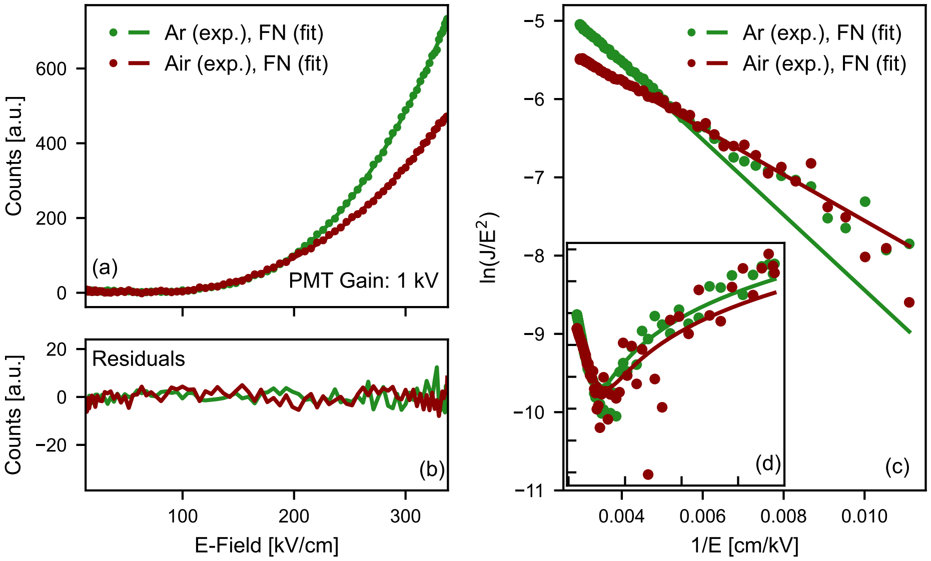

Figure 3.5. Field-dependent light emission from Argon and ambient air detected with a PMT and fitted with a FN-fit. The PMT-response is plotted over the impinging THz peak field strength (a) and fitted with a FN-fit. In (b), the residuals are displayed. Additionally, in c), the truncated FN-plot for a fit without the constant d, and in d), the FN plot for a fit including d is presented. Here, an additional offset of 10 is added to the data.

field dependence of the emitted light from the dye-doped solvents can be seen in figure 3.6. Also, the PMT responses for the liquids are fitted with equation (3.2). A mismatch between the data and the fits can be observed and is clearly seen in the residuals of the fit. For field strengths from around $75\,\mathrm{kV\,cm^{-1}}$ to $200\,\mathrm{kV\,cm^{-1}}$, the fit overshoots the data, followed by an underestimation from $200\,\mathrm{kV\,cm^{-1}}$ to $300\,\mathrm{kV\,cm^{-1}}$.

A possible explanation for the mismatch can be given by not only assuming the FN-emission as the source for the electrons and the excitation of the dye. Due to local field enhancement around the tip of the antennas, the electric field strength approaches tens of $\mathrm{MV\,cm^{-1}}$. Such field strengths are in the order of magnitude of observed field ionization of molecules [115]. When the field only tilts the molecule's potential, it is called tunnel ionization and was observed for strong THz fields in water [74]. The tunnel ionization rate W_{stat} for complex atoms in intense static fields is described by [116]

$$W_{stat} = \frac{|B|^2}{2^{|m|}|m|!}\frac{1}{\kappa^{2Z/\kappa-1}}\left(\frac{2\kappa^3}{E}\right)^{2Z/\kappa-|m|-1} e^{-2\kappa^3/3E} \tag{3.3}$$

with E as field strength, Z as nuclear charge, m as the magnetic quantum number, and B as known constant. κ is given through the ionization potential $I_p = \kappa^2/2$. For a slowly varying

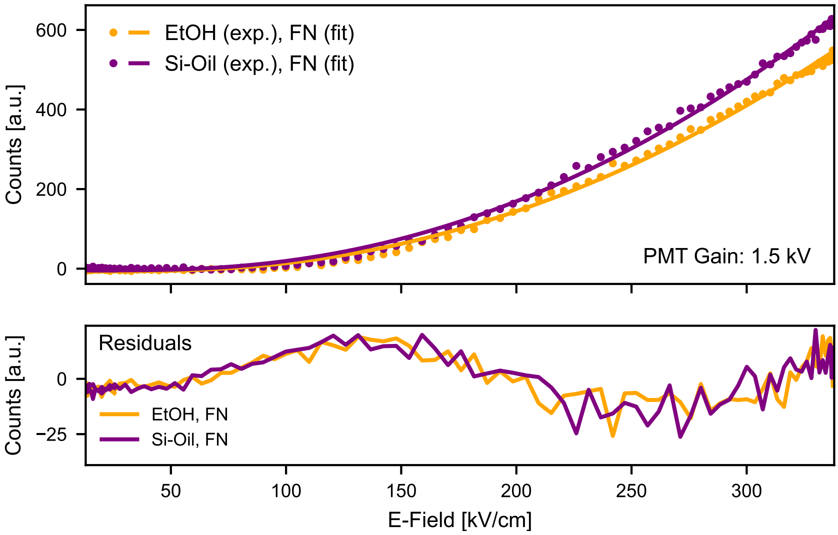

Figure 3.6. Field-dependent light emission from dye-doped EtOH and silicone oil. The recorded data are fitted with an FN-fit. The fit exhibits clear mismatches to the data, which can be clearly seen in the residuals of the fit.

field, the tunnel ionization rate can be approximated as [116]

$$W \approx \left(\frac{3E}{\pi\kappa^3}\right)^{1/2} W_{stat} \tag{3.4}$$

Knowing that EtOH, silicone oil, and the dye molecule are presumably not perfectly described by the model above, the field-dependent measurements are fitted with equation (3.3) due to a lack of an analytic model describing large molecules. The expression for a diatomic molecule can be found in [117]. However, we will use the expression shown in equation (3.3) because the differences are in the expressions, which are used as free parameters in this discussion. Moreover, the static field tunnel ionization equation is chosen due to the fact that the applied THz pulse here is much longer than the tunneling time (low Keldysh parameter $\gamma \ll 1$). To fit the recorded data with equation (3.3), we make the following simplifications:

1. We assume that $m = 0$ due to the problem that common fitting algorithms based on non-linear least squares perform their fitting with floating numbers.
2. We group $\kappa^{2Z/\kappa - 1}$ in the fitting parameter d

This leads to our fitting function:

$$W = k_1 \left(\frac{k_2^2}{|\beta_{TI} E|}\right)^d e^{-k_2^3/|\beta_{TI} E|} \tag{3.5}$$

Here, we have 4 free parameters $k1$, k_2, d, and β_{TI}. Applying those fitting functions to the data, we obtain a great fit with minimal residuals (see figure 3.7). The good agreement between the data and the adapted tunnel ionization theory shows that conventional FN- theory is not the best fit for describing the process, but due to the changes made to the tunnel ionization equation, we cannot conclude that the observed signal is purely from tunnel ionization of the molecules. The process for a deviation of the recorded data from the conventional FN-theory cannot be determined here. However, equation (3.5) gives the possibility to derive a phenomenological FN-equation describing field emission rates if the field dependence is not limited to the metallic surface.

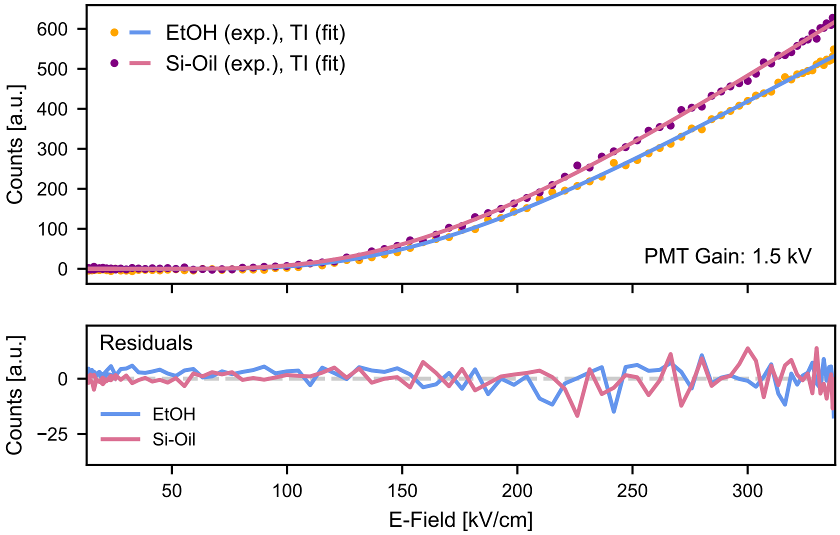

Figure 3.7. The data of the light emission from liquids fitted by adaption of the equation for tunnel ionization.

To confirm that equation (3.5) does also deliver a good agreement with the measurements agreeing already well with the conventional FN-theory, the light emission from gaseous materials is fitted again with equation (3.5). The new fit compared to the conventional FN-fit can be seen in figure 3.8. Applying both equations leads to nearly the same fit of data, and for both fit functions, the residuals are minimal. The result that both functions do fit gaseous data perfectly results in that equation (3.5) must be equal with the FN- fit equation.

$$k_1 \left(\frac{k_2^2}{|\beta_{TI}E|}\right)^d e^{-k_2^3/|\beta_{TI}E|} \overset{!}{=} c_1 \cdot a_n \frac{1}{\phi}|\beta_{FN}E|^2 \cdot e^{-b_n \phi^{\frac{3}{2}}/|\beta_{FN}E|} \tag{3.6}$$

Here, we see that this equation is only true if $d = -2$. The fits for the gases reveal d-values of $d_{Ar} = -1.94$ and $d_{air} = -1.87$. Those values are close to 2. The small mismatch might

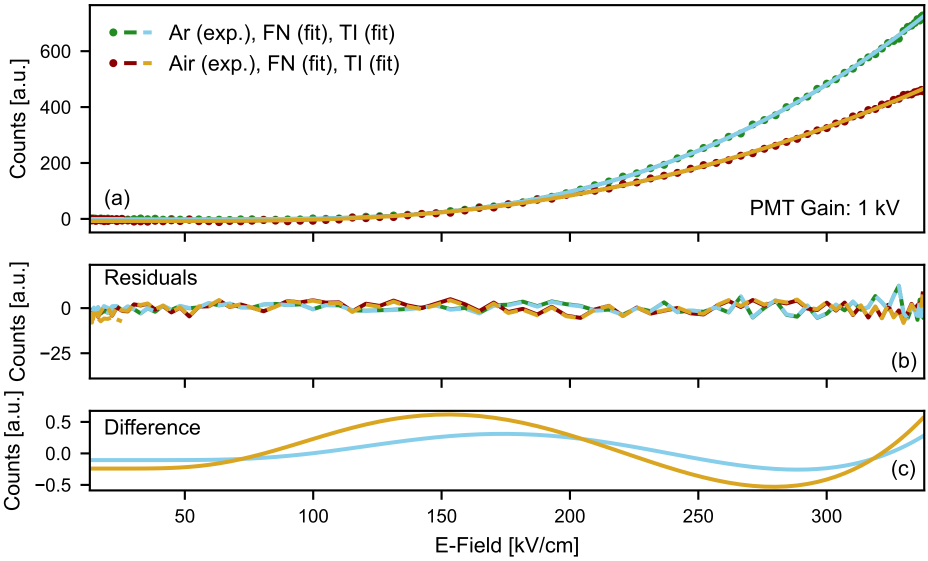

Figure 3.8. Light emission data fitted with the FN-equation compared to a fit through an adaption of the equation for tunnel ionization (a). In (b) are the residuals presented, which show that both fits lead to nearly the same result. The differences between the two fit-function can be seen in (c).

be the reason for the mismatch of the FN-fit, which is small but bigger for air than for Argon (see figure 3.8).

In order to compensate for this mismatch, we introduce the free parameter α to the FN-equation.

$$k_1 \left(\frac{k_2^2}{|\beta_{TI}E|}\right)^d e^{-k_2^3/|\beta_{TI}E|} = c_1 \cdot a_n \frac{1}{\phi}|\beta_{FN}E|^{2\alpha} \cdot e^{-b_n\phi^{\frac{3}{2}}/|\beta_{FN}E|} \tag{3.7}$$

Both sides of this equation return the same value for a given electric field E. Because we can easily fit the left side to our data, we can determine α, β_{FN}, and c_1 by the following relations:

$$\alpha = -\frac{d}{2} \tag{3.8}$$

$$\beta_{FN} = -\frac{b_n\phi^{\frac{3}{2}}\beta_{TI}}{k_2^3} \tag{3.9}$$

$$c_1 = \frac{k_1 k_2^{2d}\beta_{FN}^d\phi}{a_n\beta_{TI}^d} \tag{3.10}$$

Applying those relations, the light emission data can be matched by applying the corrected parameters. This leads to the phenomenologically derived extended FN-equation:

$$J = c_1 \cdot a_n \frac{1}{\phi} |\beta_{FN} E|^{2\alpha} \cdot e^{-b_n \phi^{\frac{3}{2}} / |\beta_{FN} E|} \tag{3.11}$$

The introduction of α made it possible to achieve good agreement with the here presented 4 data sets. In table 3.1, the FN-field enhancement factor and the corrected one are displayed, together with the α parameter. One can see, as discussed before, that for the gases, α deviates only slightly from 1, while for the liquids, the deviation is enormous. Also, between the liquids, a huge difference in the α values is observed. We attribute that to the above-mentioned oxygen quenching in the EtOH, causing a reduced light emission for the same incident field strength.

Table 3.1. Fitting parameters α and the corrected values for the field enhancement β_{new} compared to β return for the FN-equation.

Material	α	β_{new}	β
Argon	0.97	1629	1689
Air	0.93	2394	2685
Ethanol	0.0134	1234.19	6663
Silicone oil	0.1666	1431	6636

Comparing the β- factors for the two fits, we can see that the fit with the slight modification with α lead to a reduction in the field enhancement factor, which brings the values closer to realistic values. However, even for the corrected values, the field enhancement is over-estimated. Simulations suggest field enhancement factors of about 2-3 times lower. A miscalibration of the THz field could lead to lower field strength and, due to that, to a higher β value. Moreover, the fits are performed with the peak value of the electric field. Better fit parameters might be retrieved by fitting with the integral over the FN-emission for all field strengths included in the pulse. Moreover, we are treating the emission as if it were from a single emitter. However, in reality, the signal is a combination of emissions from many emitters on the metasurface where the field is distributed Gaussian.

The change in β for different surrounding materials of the antennas can just be partially explained. The lower values for the liquids are expected due to a significant change in refractive indices between gas and liquids. The change in the refractive index changes the resonance frequency of the antennas, leading to a mismatch between the center frequency of the THz pulse and an off-resonance excitation. Nevertheless, the difference in β between the two gases cannot be explained by that. Even a pressure difference between the gases would not lead to a substantial enough change in the refractive indices to shift the resonance significantly [118]. However, we kept ϕ constants for all samples. As discussed earlier, the environment of the emitter influences ϕ, which causes a sample-dependent work function. A change in the emitters' work function would lead, for the here present fits, to a change in β.

The modification of the field exponent in the pre-exponential term of the FN equation, deviating from the square as commonly used, was previously proposed [119–121]. In [119], the argument is that the emission area and the barrier shape are field dependent and cause a deviation from the square. Later, Forbes [120] proposed to change the square to a variable parameter. His reasoning behind this proposition included a voltage-dependent emission area, a weak field dependency of the work function, and the fact that the square originates from the integration over all electronic states in a bulk metal. However, other materials have different distributions, which could lead to a change in the exponent. Furthermore, in [121], a modification of the field exponent due to the surface roughnesses of the emitter is derived. However, also changes in the exponent of the exponential are suggested due to the roughnesses.

In the above-presented work, the introduction of α to the FN-equation provides a more accurate fit for the data presented in this study and was derived by considering tunnel ionization as a potential electron source. Based on the literature and the there given reasons for the modification, the attribution of the adjustment to tunnel ionization of the molecules seems reasonable. Moreover, the fact that a significant deviation is only observed for the liquid samples and not for the gases points towards an effect in the sample, not in the emitter. Further experimental verification needs to be done. However, there are indications for THz-induced tunnel ionization of the liquid sample, which can be included in the FN-equation by the introduction of α. As mentioned before, THz tunnel ionization was previously observed [74] as well as static field ionization of liquids [122].

However, previous observations for static field emission experiments in dielectric liquids also observed a deviation from the FN-plot, and the influence of space charge effects was discussed [98, 99]. In a recent theoretical study about field emission into liquid and gases [123], the experimental data from [99] are reanalyzed with a model which takes the electron mobility in a medium into account. It was observed that for increasing field strength, a transition from the FN-equation to the Mott–Gurney law takes place. The Mott-Gurney law describes space charge limited current in semiconductors and insulators. Additionally, experimental and simulation results on field emission and ionization in mineral oil concluded that the Zener-like ionization and impact ionization for positive and negative voltages contribute to the measured currents, respectively [124]. Their model for Zener ionization had the form $G = A \cdot F \exp(-B/F)$ with A and B as fitting parameters. This equation corresponds to equation (3.11) with $\alpha = 0.5$, which would make a description of the data possible by applying it.

Certainly, space-charge effects need to be considered as a possible contribution to the deviations of the presented data from the standardFN-equation. If that is the case for the here presented THz field emission into liquids, it is included in α. Also, the difference between the aforementioned experiments of field emission into dielectric liquids and the here presented study needs to be considered. Here, the emitting field is of oscillatory nature and is applied in a pulsed manner. Moreover, it is a secondary process that is measured. In the static field emission experiments, a dc-voltage is constantly applied to the emitter, and a current is measured. Those differences might lead to the domination of different effects in the experiments.

In figure 3.9 a), the recorded data for liquid samples are plotted as FN-plot with the standard FN-equation of the form $J \propto F^2 \exp(-K/F)$. The linearity of the plot is not given. Saturation is visible for higher fields. This might be an indication of space charge effects. The introduction of α returns as a linear plot (see figure 3.9 b)) meaning that the obtained α values incorporate the deviations from the standard FN equation.

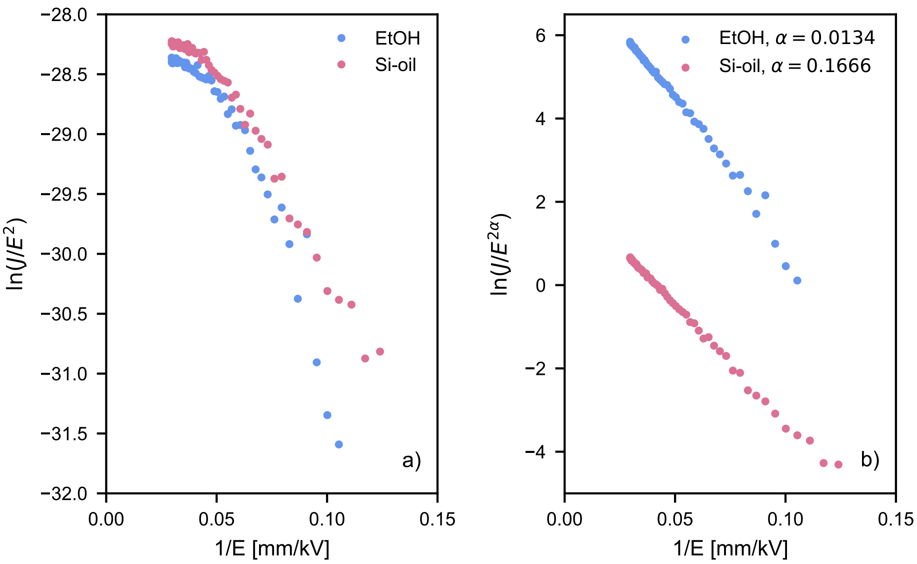

Figure 3.9. FN plots for the liquid samples. In a), the standard FN plot is shown. In b), the FN plot for taking α into account is presented.

The introduction of α as an extension to the FN-equation was motivated by tunneling ionization. However, it should be noted that tunnel ionization is not the only effect that could be incorporated into the extension. The deviations observed in the data require further investigation to understand the contributions from various sources. Nevertheless, the inclusion of the α parameter accounts for field-induced effects and offers potential for gaining a deeper understanding of the field emission process.

3.3.2 Simulation of Electrons in Argon Gas

After the discussion of the experimental data, simulations of the electrons in the accelerating THz field are discussed. The simulations are based on a ballistic acceleration of the electron in the external field, and the theoretical kinetic energies of the electron and their average travel distance in a gaseous environment are discussed. The simulation is not based on a full-blown scattering theory for gases but more on a simplistic pinball model and an adaptation of the Drude model [125].

Simulation Structure The simulation of the acceleration of the electron is simply based on the ballistic acceleration of the electron in an external electric field in 1D. Firstly, we do not take the emission processes of the electron into account. The electron is placed in the electric field of the THz pulse directly at the emitter. The electron is treated so that it does not have any prior kinetic energy, and the releasing field is still present to accelerate it. At every release, only one electron is considered. The acceleration a_e is calculated by:

$$a_e(t) = \frac{\mathrm{d}v_e(t)}{\mathrm{d}t} = \frac{q}{m_e}\beta(s)E_{THz}(t) \tag{3.12}$$

β is the location-dependent field enhancement factor. The accelerating field decreases as the electron moves away from the emitter. The decay function is determined by a finite-element simulation. Solving this equation numerically delivers us the velocity v_e and the traveled distance s_e for an electron accelerated by an enhanced time-dependent field in a vacuum. For the vacuum case, equation (3.12) can be used to estimate the kinetic energy E_{kin} of an electron. However, in the experiment described above, the emitter is surrounded by a gas or a liquid. In order to simulate an approximation of the experiment, equation (3.12) is extended by a scattering term. This term allows for approximating the electron in a gaseous environment. The final equation is the following:

$$a_e(t) = \frac{q}{m_e}\beta(s)E_{THz}(t) - \frac{v_e^2}{|l(v_e)|} \tag{3.13}$$

v_e is the velocity of the electron, and l is the mean free path length in the medium. This equation is based on the assumption that the electron-electron interaction is negligible, the electrons do not penetrate the gas atoms, and the electron trajectory is a straight line between collisions. Moreover, the electron loses its momentum at every collision.

The traced electron gets accelerated in the time-varying field and scattered and again accelerated. When the field turns negative, the electron feels a force toward the emitter and eventually, it collides with it. In the performed calculations, the electron is only traced until it collides again with the emitter. Secondary emissions due to electron-metal interaction are not considered. Additionally, an electron is only released when the field is positive. For the negative fields at the release time, the simulation is immediately interrupted and continues with the tracing of the electron emitted in the next time step. The simulation has two different time axes. One of them is the release time of the electron, which corresponds to the time axis of the propagating THz pulse. The second axis is the simulation time. It corresponds to the time in which the released electron is traced. We choose a time of 10 ps.

The mean free path length is calculated from the effective scattering cross section for momentum transfer of electron Argon scattering. The cross-section data are retrieved from the LXCat database [126] (COP database, www.lxcat.net, retrieved on January 11, 2022.). In the LXCat database, the here applied cross-section can be found in the Phelps database and is based on [127].

The simulation is also calculating the number of collisions N with an argon gas atom per released electron by the following differential equation.

$$\frac{\mathrm{d}N}{\mathrm{d}t} = \frac{|v_e|}{l(v_e)} \tag{3.14}$$

This equation is coupled to equation (3.13) by the electron velocity v_e. Only ionizing collisions are taken into account, which are determined by the ionizing cross-section for argon [126]. For the determination of the traveled distance and the energy of the electron, the effective scattering cross-section is applied. However, the number of collisions is calculated only for collisions that lead to the ionization of the Argon atom. The light-emitting excitation states are, for simplicity, ignored. In the simulation, at every time step of the THz pulse, an electron gets launched and accelerated in the field following the launch. So far, the simulation is independent of the FN-equation. However, due to the knowledge about the electron's behavior at any point in time of the THz pulse with a given field strength and β, a relative number of emitted electrons per release time can be estimated. In other words, the released electrons can get weighted by the FN-equation.

Simulation results Weighting the electron release over a THz pulse, it can be observed that the main emission takes place around the peak field of the pulse. For the THz pulse used in the experiment above, the emitted electron pulse has FWHM of 100 fs, which is more than 10 times shorter than the releasing THz. This is important if the electrons should be employed in ultrafast fast experiments. However, the pulse will rapidly spread out in time due to electron-electron interaction as well as due to different velocity components in the pulse.

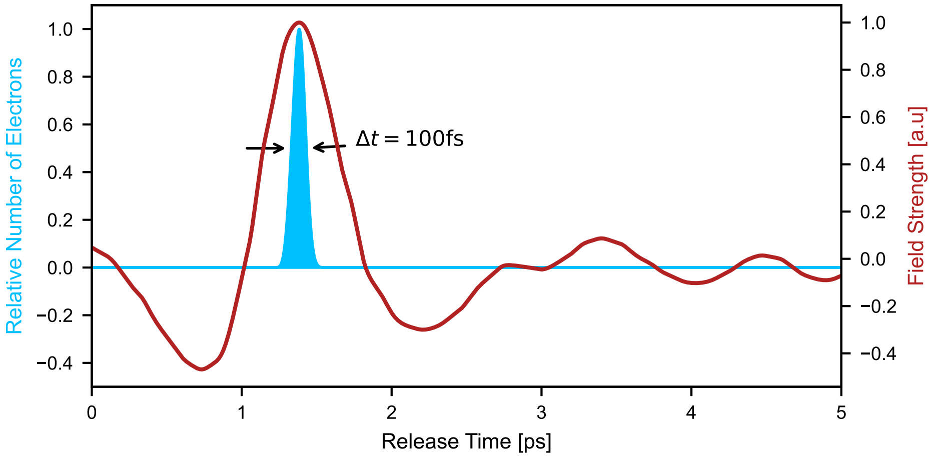

Figure 3.10. The majority of electrons are emitted around the peak of the THz field. The FWHM of the electrons is here 100 fs.

The l is pressure dependent, which causes changes in the electrons' kinetic energy E_{kin} and travel distance s_e. The higher the pressure, the more frequently the electron scatters, and with increasing pressure, E_{kin} and s_e are declining. Running the simulation for pressure values of 0.0, 0.5, 1.0, and 1.5 bar gives us insights into the maximum traveled distance of the electron and their kinetic energy. The simulation values for the emitting field strength and the enhancement factor β are 337 $\mathrm{kV\,cm^{-1}}$ and 120, respectively. The field strength is

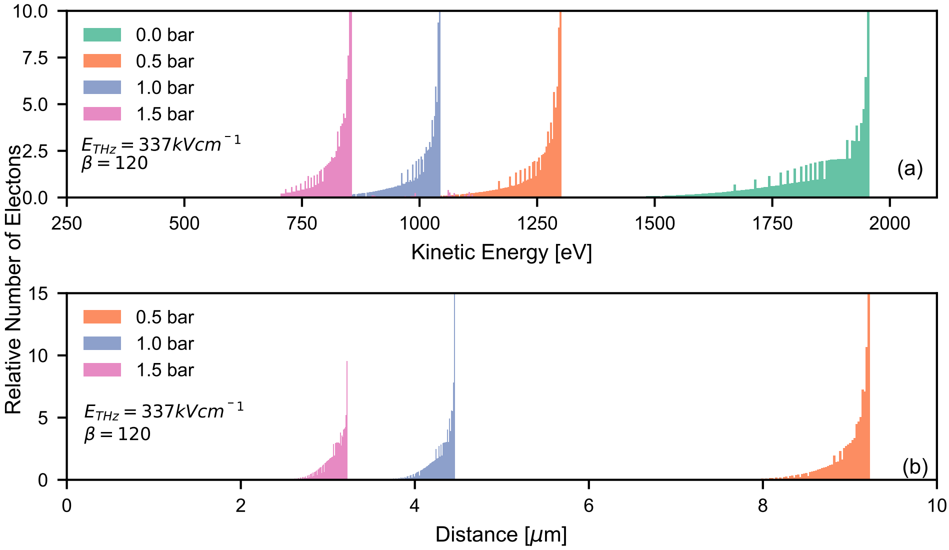

Figure 3.11. Pressure dependence of the distribution of the maximum kinetic energy (a) and traveled distance (b) of the electron.

chosen because of the experimentally measured field (see figure 3.4) and the β value of 120 is the result of the maximum field enhancement returned by a finite-element simulation of the emitters used in the experiment. It is important to note that the β factor can vary depending on the mesh size used in the simulation. In fact, other simulations have suggested higher β factors. However, there is currently no perfect method for determining the β value. The β value of 120 is just an example and should not be considered definitive.

In figure 3.11 (a), the energy distribution of the emitted electrons for the different pressures is presented, and in (b), the maximal traveled distance. For the vacuum case, the electrons gain energies up $1900\,\mathrm{eV}$ with a sharp energy cut-off and a long tail of electrons with lower energies. The sharp cut-off energy is expected due to the limited energy the electrons can gain in a given field. The high number of electrons for the high energy is due to the weighting with the FN-equation. The most electrons get emitted for the strongest accelerating field, whilst for the lower fields, fewer electrons get emitted and the accelerating field is lower. Even in lower fields before the peak of the field, the electron is moved already away from the tip and does not experience the enhanced field. The shape of the energy distribution in the vacuum matches well the ones previously observed in the literature [11, 12, 89]. The energies vary due to differences in the local field enhancement and the impinging THz field. Increasing the pressure leads to a shift of the distribution to lower energies due to energy loss in collisions with the gas atoms. Also, the lower energy tail is reduced due to early collision.

The electron's travel distance decreases as pressure increases, as shown in figure 3.11 (b). The electron's movement in a pressure of $1\,\mathrm{bar}$ is approximately $9\,\mu\mathrm{m}$. The simulation appears to underestimate the electron's distance traveled when compared to the emission spot in figure 3.3. Two possible explanations for the observed phenomenon are: (1) the metasurface in the camera image is slightly out of focus, leading to an apparent increase in spot size, and (2) the local field enhancement factor may exceed 120, resulting in greater electron energy and travel distance prior to scattering.

Every electron emitted along the THz pulse is traced and can be analyzed. In figure 3.12,

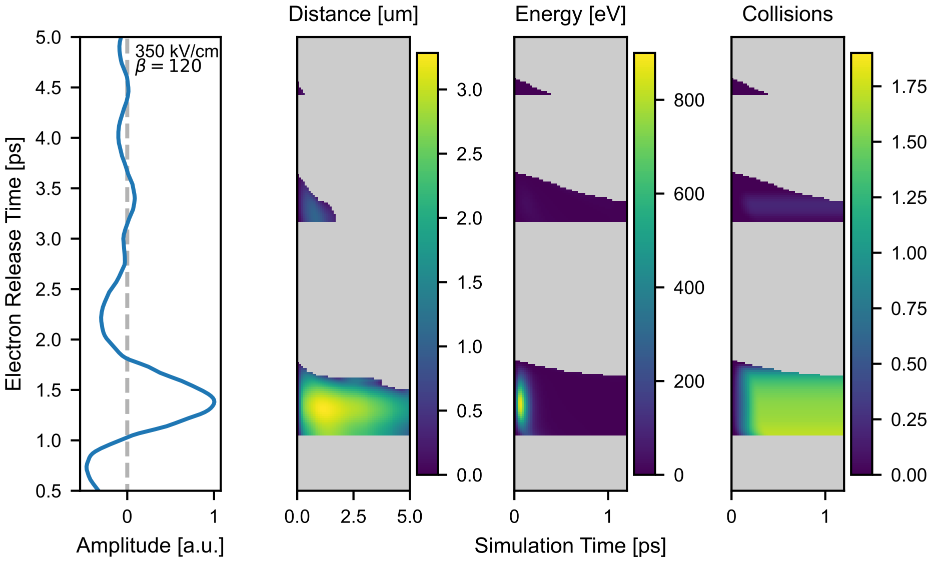

Figure 3.12. The figure presents the simulation results for every electron emitted along the THz pulse. The distance, energy, and collisions for each electron can be seen. The grey background indicates that the termination event of the simulation occurred.

the electrons are released along the THz pulse and are traced, and their traveled distance, their energy, and the number of ionizing collisions are calculated and displayed. The grey areas indicate the termination of the simulation due to electron-emitter interaction. For the presented simulation, a field strength of $350\,\mathrm{kV\,cm^{-1}}$ and a field enhancement factor of 120 are chosen. One can see that only for a positive field is an electron successfully released. For the negative fields, the simulation is immediately terminated. Moreover, it is clearly visible that even without weighting the emission by the FN-equation, the main peak leads to the most emitted electrons. The electrons acquire quickly after emission high energies and do not lead to ionizing collisions. However, the electrons rapidly lose energy and the collisions start to increase but steady on a constant level. The main energy loss of the electrons happens by non-ionizing collisions.

The number of ionizing collisions during one THz pulse can be calculated for different β-values. For β of 120, 500, and 800, the numbers of collisions for a changing electric field are shown. Simulations showed the maximum field enhancement ranges between those β-values.

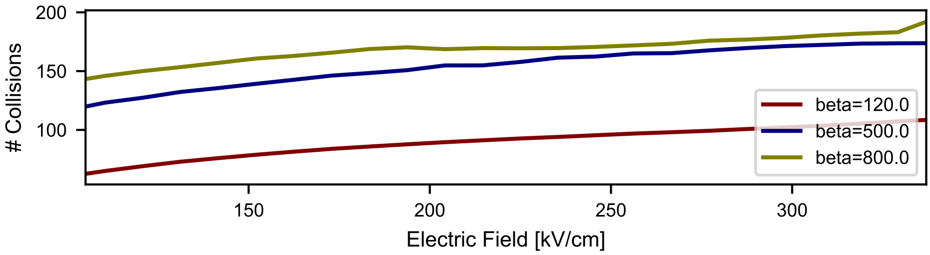

Figure 3.13. The number of collisions for electrons emitted along a THz-pulse for different β-values are presented.

The numbers of collisions increase with increasing field strength but saturate for higher fields. The slope for all β is gentle and gets shallower for higher β. This indicates that the collected light is mainly dominated by the number of emitted electrons and less by their collisions with the argon atoms. The collisions add a relatively flat background on top of the FN-equation. This result was assumed in the previous measurements due to the fact that the signal was following the FN-emission curve.

Lastly, the number of collisions should be weighted with the number of electrons emitted at every time step along the THz pulse and compared to the recorded data of the light emission from argon. In figure 3.14, the measurement is matched with the number of collisions weighted with the number of electrons tunneling out of the emitter for the momentarily applied field. If the numbers of collisions only get weighed by the FN-emission for a field enhancement factor that was used to calculate the collisions, the result does not match the measurements (see dashed lines in figure 3.14 (a)). However, the higher the field enhancement factor is, the closer the result is to measurements. Applying a β of 2000, the simulation result matches the data very well. This is due to the fact that in higher fields, the number of collisions becomes nearly constant with any change in the impinging field, and only the number of electrons increases. However, a β-value of 2000 does not seem to be realistic due to very high electron energies. Such high electron energies are not reported in the literature for THz field emission processes from a sharp emitter tip [12, 13]. For lower β -values, the number of emitted electrons is not high enough when weighting with a FN-equation with a triangular barrier shape. However, by introducing the SN barrier, a better agreement between the data and the simulation can be achieved (solid lines in figure 3.14). However, for the low field enhancement of 120, $v = 0.06$. This indicates that the barrier would be needed to be reduced significantly, which also physically has no explanation. The best agreement between the simulation and the measurement is achieved for a β of 800 with a barrier shape correction factor v of 0.4. Also, here, the barrier would still be reduced significantly. The field enhancement factor of 800 is close to values obtained for high-resolution finite element simulations of the antennas.

The introduction of the SN-barrier is a valid approach based on several theoretical models and should be generally included if the discussion about THz field emission aims to deliver

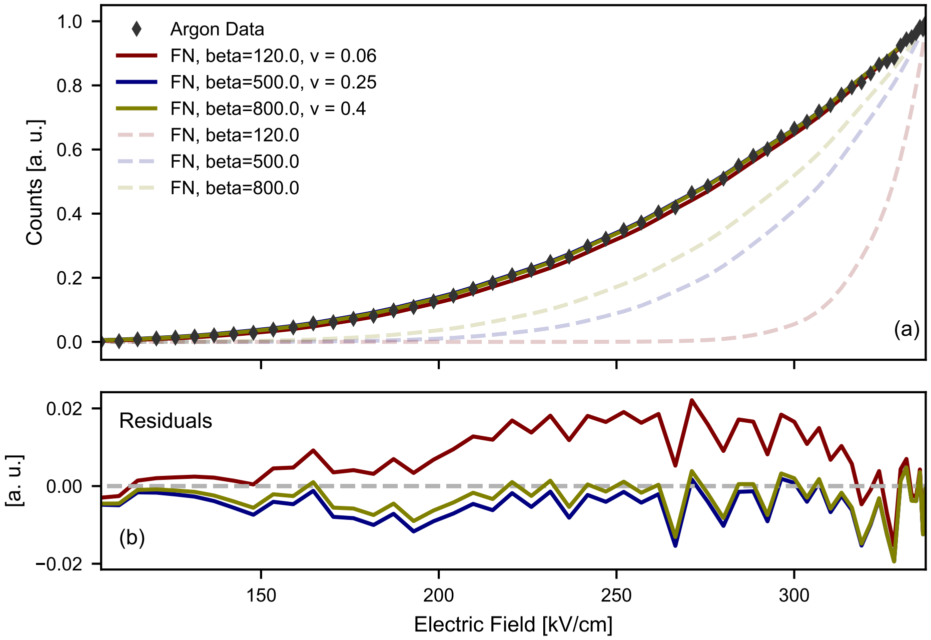

Figure 3.14. In panel (a), the recorded Argon data is matched with the simulation. The number of collisions is weighted by the number of emitted electrons according to the field enhancement factor. In (b), the residuals between the recorded data and the matched simulations for a SN-barrier shape are shown.

a physically relevant value of the number of electrons, the field enhancement factor, or the workfunction. An important discussion about it can be found in [85]. Therefore, the inclusion of the barrier shape in the analysis of the simulation has to be considered because the number of electrons becomes relevant. Fitting the Argon data with a FN-equation extended by the SN-barrier shape leads as well to a good fit to the data and matches considerably well with the barrier-correction factor obtained in the simulation, as well as β. The fit delivers $v = 0.402$ for the barrier correction factor and $\beta = 679$. Considering the barrier shape does not change the quality of the fit but makes it, in my opinion, more meaningful. However, it has to be mentioned that applying the barrier shape to the data obtained from air, does only leads only to a correction factor of $v = 0.85$, which does not lower β significantly.

3.4 Conclusion

In the experimental part, we observed light emission from gases and liquids, which can be attributed to tunneling phenomena. For the gaseous samples, the recorded photo-signal showed good agreement to fits of the traditional FN-equation. Later, the FN-equation with a SN-barrier shape was fitted as well to the data and delivered good agreement. Also, the recorded data from the liquid samples clearly followed the trend of a field emission process. However, the applied fits indicated discrepancies with the data, which raised the question of whether a competing mechanism, tunneling ionization of the molecules, contributes to the detected photo signal. This line of thought led us to a phenomenologically derived correction parameter in the FN-equation which takes potential additional field effects, such as tunnel ionization or space charge effects, besides FN-tunneling into account.

Besides the experimental data, simulations of the field-emitted electron in the external field have been presented. This provided insights into the electron energies acquired for certain field enhancement factors β and gas pressures. Comparison to the literature indicated that high β-values might lead to good fits but the theoretical energy which an electron should acquire in such strong fields does not match with the experimental data. However, the simulation could be matched well with the recorded photo-signal from argon-gas by including the SN-potential barrier to the simulation.

Concluding this chapter, it can be stated that THz field emission of electrons into liquids is possible. Nevertheless, there are indications of other field-induced effects, which can be described by extending the FN-equation by a correction factor α. Moreover, a simulation for simple electron tracing in a gaseous environment was provided.

Subsequent measurements are spectroscopic measurements by recording the electron-induced emission spectrum from the samples. The spectrums will give us insight into the involved electronic transitions. An additional experiment in which the metasurface is covered by a nanometer-thin dielectric layer to prevent the electron from reaching the gas or liquid could finally answer the question if the recorded signal is purely due to FN-emission from the metasurface or if the enhanced field causes light emission from the medium.

CHAPTER 4

Mid-IR PMT based on Field Emission

4.1 Introduction

In this chapter, we study a new device for detecting mid-infrared (mid-IR) radiation using electron field emission. The first introduction to the device can be found in [89]. The working principle of the described device is similar to that of a normal PMT, and therefore it will be referred to as a mid-IR PMT. In recent years, a ”THz-PMT” was developed in the Ultrafast Infrared and Terahertz Science group at the Technical University of Denmark in collaboration with Hamamatsu Photonics [16]. Compared to a traditional PMT, the photo-cathode was removed and replaced by metasurfaces which are optimized to increase the electron yield by THz-induced field emission. The same principle is applied to the mid-IR PMT.

The mid-IR region is loosely defined from $2\,\mu\mathrm{m}$ - $20\,\mu\mathrm{m}$. In this spectral range, many molecules show their fundamental vibrational modes, which makes mid-IR radiation suitable for plenty of applications such as spectroscopy [128], gas-sensing [129], remote sensing [130], and imaging [131]. The detection of mid-IR is challenging due to the high background noise level and the lack of suitable materials for high sensitivity and selectivity. Fortunately, the developments over the last decades made it more feasible to detect mid-IR rather easily. Two main categories of mid-IR detectors are available, photonic devices and thermal infrared detectors, which include Bolometers and Prytorelectro detectors (see section 1.3.2) [132, 133]. Photonic devices show a fast response time, while thermal detectors exhibit slower responses. Both device types show significantly better performance at lower temperatures. Currently, the preferred photonic detector types are mercury cadmium telluride (MCT) detectors, but also quantum well and quantum dot based detectors are advancing [134].

The here presented mid-IR PMT delivers an alternative way for mid-IR detection. It does perform at room temperature and has a similar response time as normal PMTs ($\approx 10\,\mathrm{ns}$), which is determined by the design of the PMTs electron collection [135]. In mid-IR PMT, the photocathode is replaced by a metasurface.

In the following, we will employ radiation between the $3.6\,\mu\mathrm{m}$ - $10.7\,\mu\mathrm{m}$ (mid-wave and long-wave infrared). The mid-IR PMT will be explained and characterized first. Afterward, the mid-IR PMT is used to record interferometric auto-correlation (iAC) traces of the mid-IR pulses. Those auto-correlation (AC) traces are dependent on the field strength at the metasurfaces and can be described by the FN-description of cold field emission from metal surfaces. G. Herink et al. [136] demonstrated already the possibility of performing interferometric AC by means of field emission from a metal tip. However, to our best knowledge, they never stated the mathematical description used for the explanation. Hence, we are providing a new auto-correlation integral for FN-emission

$$I_{FN} \propto \int_{-\infty}^{\infty} A\left[E(t) + E(t-\tau)\right]^2 \cdot e^{-k/[E(t)+E(t-\tau)]} dt \tag{4.1}$$

which allows us to describe our recorded data.

4.2 Methods/Tools

In this section, the mid-IR PMT and experimental methods are explained and described to provide the reader with all the necessary information to comprehend the experiments performed.

4.2.1 midIR-PMT

A photomultiplier tube, or short PMT, operates based on the photoelectric effect to generate an electrical signal and detect photons. Here, a brief overview of its working principle shall be given. (see figure 4.1).

A PMT is composed of an evacuated glass tube. When a photon strikes the front plate of the tube, a photoelectron is emitted from the photocathode. The electron is then directed by a focusing electrode toward the first dynode. A dynode is a metallic electrode to which a voltage is applied to accelerate the electron, causing it to collide with the dynode and emit a secondary electron. In a PMT, multiple dynodes are connected in series after the first one, with a potential difference between each of them that accelerates the electrons. At each dynode, the electrons are multiplied, resulting in an easily measurable current at the anode. This process enables the detection of single photons. However, to photoemit electrons, the energy of the light must be higher than the work function Φ of the photocathode material. This limits the application of PMTs to the detection of light with shorter wavelengths than approximately $1.7\,\mu\mathrm{m}$.

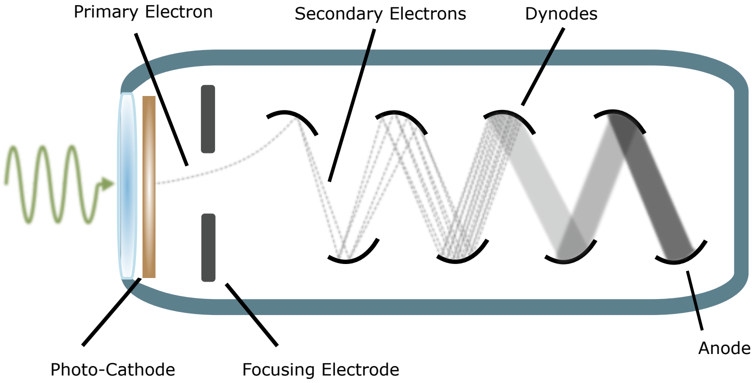

Figure 4.1. Schematic of a PMT. When light hits the photo-cathode, it emits a primary electron, which is then multiplied by the dynodes. This multiplication process allows for small signals to be amplified and measured.

To overcome that limitation of a conventional PMT, S. Lange collaborated with Hamatsu Photonics during his Ph.D. studies to develop a THz-PMT [89]. Instead of relying on photoemission, the primary electron in this PMT is field emitted. The photo-cathode in a conventional PMT is replaced with a metasurface that is optimized to field-emit electrons. The metasurfaces are positioned facing toward the dynodes so that the impinging THz-radiation illuminates the backside of the silicon substrate, causing electrons to be emitted in the direction of the dynodes, which then are accelerated by the potentials applied between the metasurface and the dynodes. This new THz-PMT allows the detection of THz radiation.

The mid-IR-PMT applied in this study is based on the same principle as the THz-PMT, with the metasurfaces scaled to the mid-IR range. The targeted resonance frequency for the mid-IR-PMT is $40\,\mathrm{THz}$ ($7.5\,\mu\mathrm{m}$). S. Lange is responsible for the fabrication of the mid-IR-PMT and has already been introduced in his thesis [89].

4.2.2 Optical Setups

For simplicity, the term ”PMT” will refer exclusively to the mid-IR-PMT from this point forward. The experiments on the new PMT are performed by applying the following setups. Initially, the generation of the mid-IR is briefly discussed. The nonlinear difference frequency generation (nDFG) technique is employed to generate the mid-IR-radiation. Therefore, a regenerative amplifier is pumping an optical parametric amplifier (OPA). The resulting Signal and Idler are then used in the nDFG to obtain the mid-IR-radiation. This technique allows changing the output wavelength continuously over a wide spectral range. The here used spectral region stretches from $3.6\,\mu\mathrm{m}$ to $10.7\,\mu\mathrm{m}$. The first setup, which is utilized to gather the fundamental properties of the PMT, is shortly explained (see figure 4.2). In this setup, the mid-IR-beam is propagated through a longpass filter (LPF) with a cut-off wavelength of $3.6\,\mu\mathrm{m}$ to discriminate the influence of the pump wavelength of the nDFG.

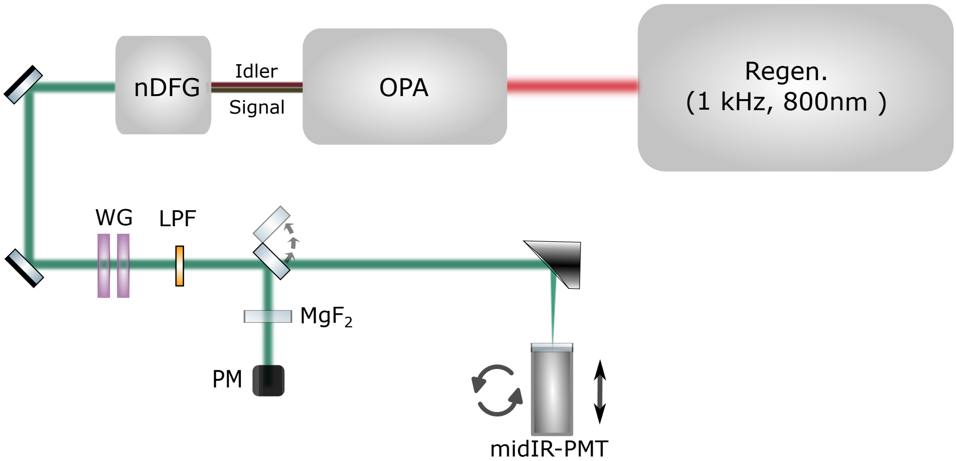

Figure 4.2. Schematic drawing of the experimental setup for the characterization of the mid-IR-PMT.

After the LPF, a pair of WGPs are in the beam path, which is used to adjust the optical power continuously onto the PMT. The power can then be measured when flipping a mirror by a power meter (PM) (Thorlabs S302C - Thermal Power Sensor Head). The mid-IR-beam is then shined onto the PMT. There are two different configurations: the beam falls collimated or focused by an OAP onto the PMT. In both configurations, the PMT is mounted in an automated rotation stage, allowing to adjust the PMT orientation to the mid-IR polarization. When using the focused beam, the PMT is additionally on top of the translation stage to position it at the desired location along the focus.

The second setup is depicted in figure 4.3. It is used to obtain an iAC-measurement of the mid-IR pulses. Therefore the mid-IR beam generated in the nDFG-model is split by a 50:50-beamsplitter (BS) (Thorlabs BSW510). The transmitted beam is delayed by a variable delay line. The reflected beam travels a static delay to compensate for the delay line. The beams get recombined with another BS with the same properties as the first one. Here, the earlier transmitted beam gets reflected on the BS, while the before reflected beam transmits through the second BS. The setup is designed with two BS to ensure that both beams obtain the same dispersion and to compensate for the slightly unequal split ratio of the BS for polarized radiation. Additionally, both beams experience an equal amount of reflection from the metallic steering mirrors. Hence, we consider both pulses as indistinguishable from each other.

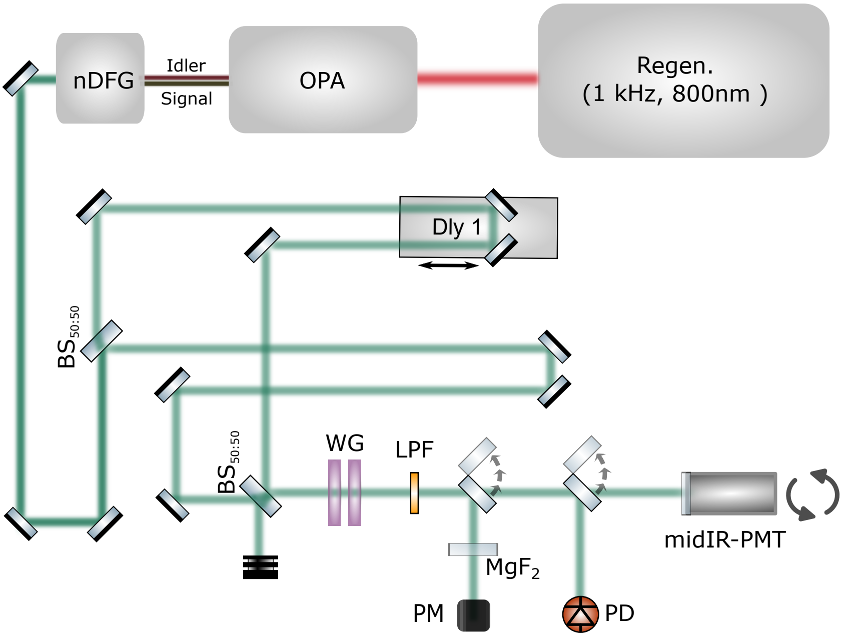

Figure 4.3. Schematic drawing of the experimental setup to perform auto-correlation measurements.

The recombined beams are propagating collinearly through a pair of WGP and an LPF (3.6 µm cut-off) to adjust the power of the beams and to filter out residual pump light, respectively. A flip mirror allows to measure the power of the mid-IR beam. To acquire the AC of the mid-IR pulses, two detectors can be utilized, the PMT and a PD (Thorlabs PDA10D2

- InGaAs Fixed Gain Amplified Detector). The window of the PD is removed to allow two-photon absorption for longer wavelength. The PMT is also in this setup mounted in a rotation mount, allowing to adjust the mid-IR polarization relative to the PMT. The beams are collimated on both detectors.

For both presented setups, the PMT is operated at a voltage of $-1800\,\mathrm{V}$, and for the data acquisition, a boxcar integrator triggered directly by the regenerative amplifier and a DAQ-card are applied.

4.3 Experiments and Results

After the methods of the performed experiment were introduced, the following section will present the results and analysis of the acquired data.

4.3.1 PMT-Characterization

The mid-IR PMT's frequency response is designed to be around $40\,\mathrm{THz}$ ($7.5\,\mathrm{\mu m}$) [89], which should result in a frequency-dependent response. Additionally, the antenna's polarization-dependent design suggests a polarization-dependent response. While both of these characteristics were previously observed in the THz-PMT, they have yet to be investigated in the mid-IR PMT. Thus, the upcoming paragraph will detail the PMT's wavelength- and polarization-dependence, and the results will be compared to fourier-transform infrared spectroscopy (FTIR) measurements and COMSOL®-simulations of the PMT's metasurfaces.

The performance of the PMT is influenced by the wavelength and polarization of the incoming light. Experimentally, it is an iterative process between optimizing the orientation of the PMT and finding the ideal wavelength. Here, the wavelength dependence of the PMT is investigated before the effect of polarization is discussed. To obtain the highest response, measurements are performed at the optimum PMT rotation angle. However, for the wavelength-dependent measurements, the absorption of the MgF_2 -window of the PMT, which is $1.58 \pm 0.01\,\mathrm{mm}$ thick, needs to be taken into account. To assess the impact of the window, FTIR measurements are performed (see figure 4.4 a)). As depicted in figure 4.4 a), the window is not suitable for long wavelengths. The transmission remains flat until $5.5\,\mathrm{\mu m}$, but it starts to decrease rapidly afterward. At $8.7\,\mathrm{\mu m}$, the transmission drops to 50%, and only 6.4% is transmitted at $10\,\mathrm{\mu m}$. As a result, this limits the wavelength range for which the PMT can be utilized.

In figure 4.4 b), the polarization-dependent transmission of the MgF_2-window for a $360°$-rotation is presented. This measurement was conducted to evaluate the effect of birefringence in the mid-IR on the polarization of the radiation, which could potentially cause a decrease in the PMT signal due to the polarization-dependent response of the metasurface. Fortunately, the results show that the polarization of the transmitted light is not significantly affected by the rotation of the window. This indicates that the window has a negligible impact on the polarization-dependent response of the metasurface.

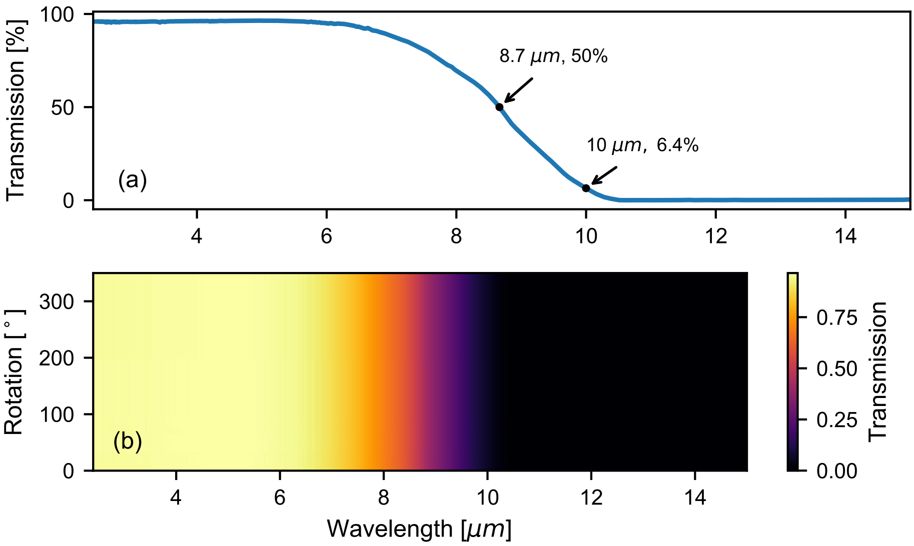

Figure 4.4. FTIR measurements of MgF_2-window with thickness $1.58 \pm 0.01\,\mathrm{mm}$. In (a) the transmission for wavelengths for $2.4\,\mu\mathrm{m}$ to $14\,\mu\mathrm{m}$ is presented. The step cut-off is clearly visible. (b) shows the rotation independence of the transmission of the window. The slight birefringence does not affect the transmission significantly.

Wavelength-dependent PMT Response Two different measurement modes are used for the wavelength-dependent measurements. In the first mode, a constant incident power onto the MgF_2-window is maintained, resulting in a reduction of the arriving power at the metasurface due to absorption in the window. This leads to an absolute wavelength dependency of the PMT. In the second mode, the power arriving at the backside of the silicon chip with the imprinted metasurfaces is kept constant by accounting for the window absorption. This measurement returns a windowless wavelength response of the metasurfaces on the silicon but does not consider the silicon's wavelength-dependent absorption. The results for a collimated beam incident onto the PMT are shown in figure 4.5. The window has a surprisingly low effect on the PMT performance for a wavelength range up to $8\,\mu\mathrm{m}$. The reason for that might be the fluctuations of the mid-IR power. However, the response is significantly lower when the absorption of the window is not compensated for.

The wavelength sweep reveals a strong PMT response between $4.5\,\mu\mathrm{m}$ and $4.8\,\mu\mathrm{m}$ with a weaker response observed at $7.7\,\mu\mathrm{m}$, which is close to the design wavelength of $7.5\,\mu\mathrm{m}$. Surprisingly, this resonance does not provide the strongest PMT response. The data in figure 4.5 a) only cover a wavelength range up to $8.5\,\mu\mathrm{m}$. This limitation is due to the collimated beam setting and the absorption of the window, which results in insufficient power from the nDFG while still measuring a significant PMT response. It is worth noting that in the collimated setup configuration, the mid-IR beam radius is larger than the metasurface, leading to unused

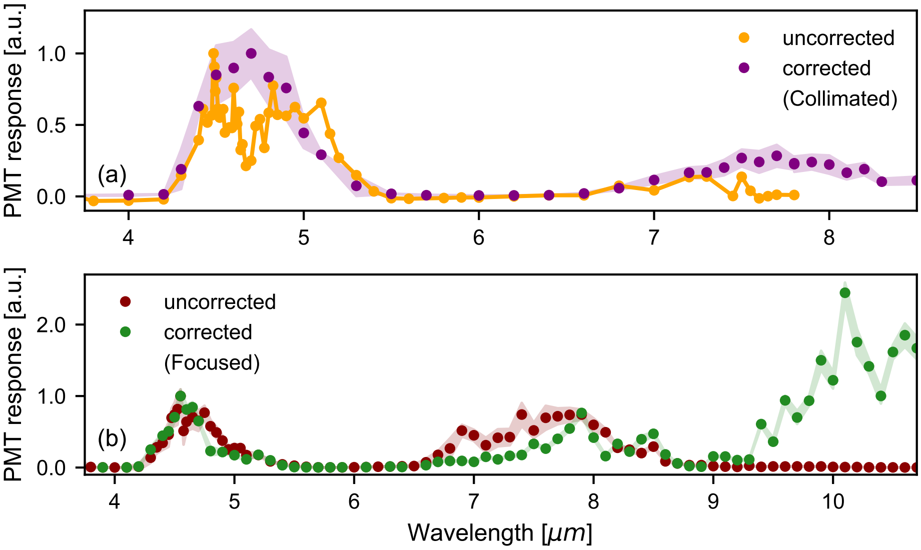

Figure 4.5. Wavelength response of the PMT. Responses accounting and not accounting for the absorption of the window are shown. In a), the mid-IR beam is collimated, while in b), the beam is focused.

mid-IR radiation.

In order to measure longer wavelengths, the mid-IR beam is focused with a silver 4-inch OAP onto the PMT. That way, the fluence on the metasurface is increased and the full beam is illuminating it. This enables to perform a wavelength sweep up to $10.7\,\mu\mathrm{m}$. The PMT is placed 1 inch away from the focus of the beam to avoid a wavelength-dependent spot size. In figure 4.5 b), the PMT response is shown. The measurement takes the MgF_2-window absorption into account. The measurement reveals a strong response at $10.1\,\mu\mathrm{m}$, which is 2.4 times stronger than the one at $4.7\,\mu\mathrm{m}$. For longer wavelengths than $10.1\,\mu\mathrm{m}$, the response is declining again. This might be an indication that it is a resonance of the metasurface and not only an increase in the field enhancement factor γ due to a lightning rod effect of the antenna tip, which increases for longer wavelengths ($\gamma \propto (\lambda/R)^{\alpha}$) [13]. R is the tip radius, and α is a constant.

Polarization-dependent PMT Response Now, the polarization dependence is investigated. Therefore, the PMT is rotated by a rotation mount while the mid-IR polarization is kept the same. The mid-IR PMT is expected to exhibit a polarization dependence due to the resonance behavior of the antenna structures. The absence of resonance would indicate that the antenna shape is not crucial for the performance of the PMT. To ensure that the metasurface did not rotate out of the beam, resulting in a significant decrease in the signal, the PMT was placed in the collimated mid-IR beam. The PMT responses recorded during the 360°-rotation of the PMT are presented in figure 4.6.

The PMT/metasurface exhibits a clear preferred orientation with respect to the incoming polarized light, where two orientations repeating by $180°$ result in an enhanced response. This observation is consistent with previous investigations of the THz-PMT, which employs as well the dSRR as antenna design. We attribute these enhanced responses to the alignment of the antennas of the metasurface with the incoming polarization. Specifically, in the case of a dSRR, the enhanced response occurs when the field polarization is aligned with the I-shaped tip of the antenna. The response of the PMT shows clear polarization dependence close to resonant wavelengths ($4.5\,\mu\mathrm{m}$, $7.5\,\mu\mathrm{m}$, $8.5\,\mu\mathrm{m}$). However, at $3.7\,\mu\mathrm{m}$, the response does not depend on the PMT orientation, suggesting that the response is not solely attributed to the resonance of the antennas. Although weaker than at the resonances, the response at $3.7\,\mu\mathrm{m}$ is still significant over the noise level. On the other hand, at $6.0\,\mu\mathrm{m}$, which is also off-resonant, the PMT response is more diminished than at $3.7\,\mu\mathrm{m}$. This could be explained by the fact that due to the shorter wavelength at $3.7\,\mu\mathrm{m}$, different parts of the antenna act independently as structures where the field can be enhanced, leading to a polarization-independent response. Conversely, for longer wavelengths, the field concentration does not happen as efficiently at the smaller structures of the antennas. Multiphoton absorption as a plausible mechanism would result in an accordingly intensity scaling (I^n). However, an intensity sweep for $3700\,\mathrm{nm}$ is not performed.

FTIR-Measurements of the Metasurface To investigate the behavior of the PMT further, we conducted FITR measurements of only the metasurfaces on the silicon chip. The three main resonances in the PMT response are unexpectedly not harmonics. The FTIR measurements are conducted to investigate whether the three main responses are a result of the PMT and the field emission process, such as back acceleration of electrons towards the electrodes for certain wavelengths, or if the metasurface exhibits intrinsic enhanced absorption of mid-IR radiation at those wavelengths. The light of the FTIR is polarized and the silicon chip is rotated to measure different antenna orientations. The collected FTIR-data (see figure 4.6) clearly show a difference between the two orientations, which are here called 0° and 90°. The naming was randomly chosen due to the lack of information about the real position of the antennas on the chip. The only information we had was that the cut of the substrate crystal is aligned with the antenna sides. The FTIR-measurement for 0° displays a broad absorption. It starts to rise constantly for about $5.0\,\mu\mathrm{m}$ until it peaks at $9.5\,\mu\mathrm{m}$ and declines again. In comparison, the 90°-orientation shows an increased absorption at around $4.0\,\mu\mathrm{m}$, $6.0\,\mu\mathrm{m}$, and a broad response starting from around $8.0\,\mu\mathrm{m}$ with a maximum at $10.5\,\mu\mathrm{m}$. The responses of both orientations do not match the resonance of the PMT. The 90°-orientation of the metasurface exhibits three main absorption peaks, however, at different wavelengths than the PMT. Moreover, the 0°- and 90°-orientations show a strong absorption at $8.5\,\mu\mathrm{m}$ whereas the PMT does show only for one of the orientations a strong response (see figure 4.6). Possible explanations for the discrepancies of the PMT and FTIR might be in the antenna structure itself. The metasurfaces were not fabricated in the same batch. Small variations in the sizes could lead to a shift in the resonances. Moreover, the FTIR is measuring the far-field response of the metasurface. On the other hand, the PMT signal is directly related to the near-field response of the antenna and the cold field emission.

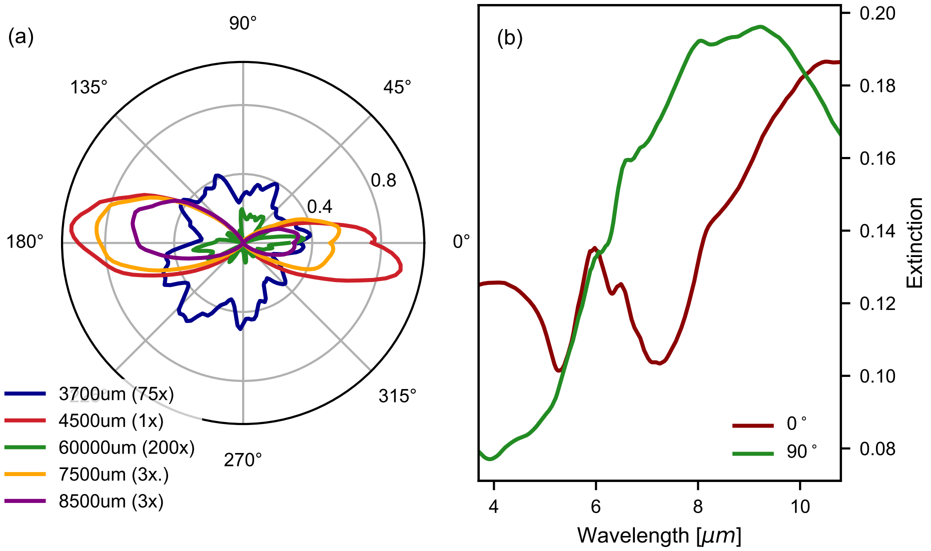

Figure 4.6. Rotation-dependent PMT response for different wavelengths (a) and FTIR measurements of the metasurfaces for different orientations (b). In the rotation-dependent response, two pronounced resonances at about 0° and 180° are clearly visible. The FTIR measurements show for both orientations an increase in extinction for longer wavelengths.

COMSOL®-Simulation of Antenna Structures For a better understanding of the antenna structure behavior in the mid-IR field, COMSOL®-simulations are performed. The model includes the frequency-dependent conductivity of the gold antenna (Drude model) and its substrate. The geometrical dimensions for the antenna are extracted from the scanning electron microscope (SEM) images of the fabricated metasurface, as can be seen in [89]. A frequency sweep from $20\,\mathrm{THz}$ to $81\,\mathrm{THz}$ (around $3.7\,\mu\mathrm{m}$-$15\,\mu\mathrm{m}$) is carried out for a plane wave polarized in the x-direction and propagating along the z-axis. The antenna is situated on the interface of domains with the properties of silicon and air. The em-wave illuminates the antenna from the silicon domain. The relative electric field enhancement at the antenna is measured. Probes obtain the field enhancement at different positions close to the antenna's gap. Here, we are not interested in the exact number for the relative field enhancement factor. The aim of the simulation is to obtain the antenna response function for different wavelengths. The simulated electric field enhancement relative to the impinging radiation at the sharp end of the dSRR tip can be seen in figure 4.7 a). The probe point is located $5\,\mathrm{nm}$ above the metallic antenna in the air domain above the gap of the dSRR. The simulated relative field enhancement for different wavelengths is compared to the measurements of the PMT response. Therefore in figure 4.7 a), the simulated relative field enhancement component in x-direction $|E_x|$ and the out-of-plane component $|E_z|$ are plotted together with the measured PMT response. Both components exhibit three local maxima at around $4.8\,\mu\mathrm{m}$, $6.8\,\mu\mathrm{m}$, and $10.1\,\mu\mathrm{m}$, which is the

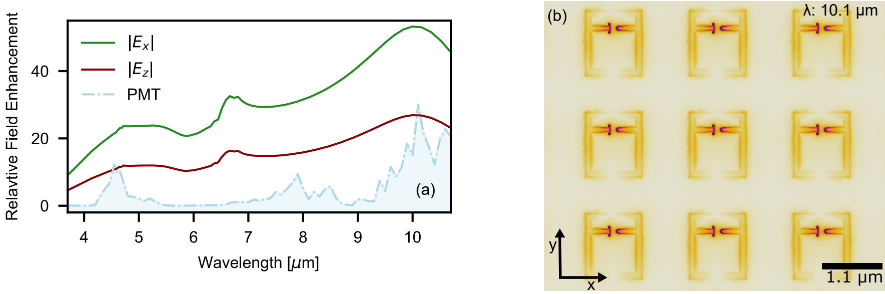

Figure 4.7. a) simulated wavelength response of metasurface (green and red line). The green line shows the in-plane field enhancement $|E_x|$, whilst the red line is the out-of-plane component $|E_z|$. The shaded area is the measured PMT response. b) Simulated antenna response for an incident field with a wavelength of $10.1\,\mu\mathrm{m}$. The field is strongly enhanced in the antenna gap.

highest one of the three. Moreover, on top of the peaks, the simulation shows a background increase in the field enhancement towards longer wavelengths. One can see that the simulation differs from the measurements. However, simulation and measurement have their maxima at round $10\,\mu\mathrm{m}$. Moreover, also the measurements show an increased response at shorter wavelengths around $4.6\,\mu\mathrm{m}$, which is only slightly mismatched with the simulated results. The local maximum at $6.8\,\mu\mathrm{m}$ does not match with the measurements, which has an increased response at around $8\,\mu\mathrm{m}$. The increasing background signal in the simulation is as well not observed in the measurements. The mismatch in the peaks of the responses can be explained by an imperfection in the fabricated antennas, which could lead to a shift in the antennas' resonance. The missing background increase of the PMT response for increasing wavelength is here attributed to the fact that the measurements are a result of field-emitted electrons, while the simulation shows only the field enhancement. In order to be detected, the electron needs to escape the emitter structure and travel in the z-direction. As we can see in the simulation of $|E_z|$, the field enhancement is reduced, including the background enhancement, which leads to a lower detection rate.

Recording the field in the transmitted field through the antenna in the simulation, a far field response is measured. The polarization of the incident light is varied. In one case, the polarization aligns with the x-axis or y-axis of the simulation coordinate system. In figure 4.7 b), the antenna's orientation can be seen. Comparison of the far field simulation and the FTIR measurements show clearly some similarities (see figure 4.8). The before labeled with $90°$ FTIR measurement is resembled by the simulation with light polarized in the x direction. The $0°$ FTIR measurement shows similarities with the simulation with polarization in the y-direction. The simulations show sharper responses than the measurements. This might be due to the differences between antennas or due to the difference in illumination between simulation and measurement. The simulation illuminate only with a single frequency at a time, while the FTIR illuminates with a broad spectrum and detects all wavelength at once.

Overall, the COMSOL®-simulations show only small differences to the measurements, which shows that the near field enhancement is responsible for the shape of the PMT response. However, the detection of only electrons moving in the z-direction influences the response

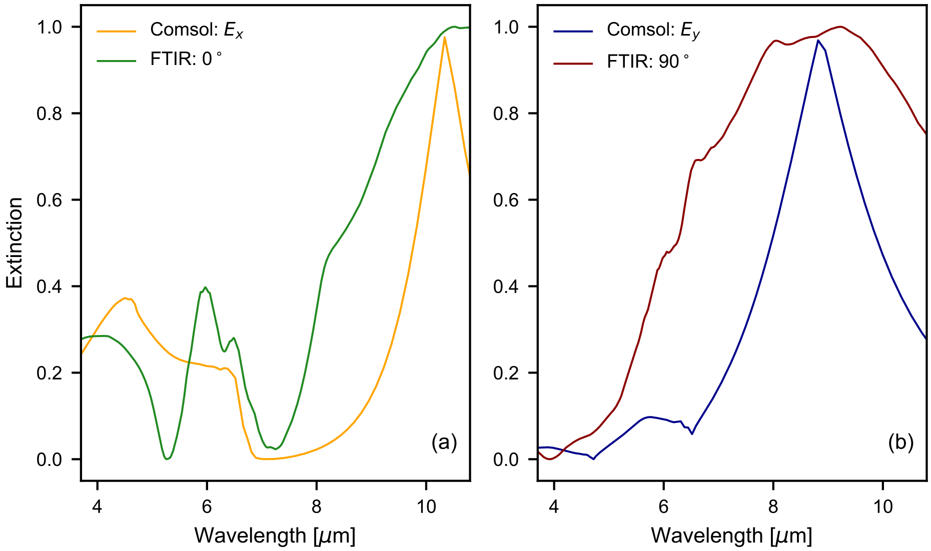

Figure 4.8. Comsol simulation of the transmitted field through the antenna compared to the FTIR measurements. a) Comsol simulation for polarization along the x-axis compared to the 90° FTIR measurement. b) Comsol simulation for polarization along the y-axis compared to the 0° FTIR measurement.

slightly. COMSOL® guide design for antennas with responses in the low response region of the PMT can help to fill the gaps in its response. Looking at the FTIR response of the metasurfaces does not lead to the expected insights about the PMT response. As we could show with the simulation, the FTIR measures the far field response while the PMT response is connected to the near field response of the antennas.

FN-Dependence of PMT for Different Wavelengths Besides the response of the PMT for different wavelengths, it should also be shown that the PMT response is due to the FN-field emission. Therefore, the PMT response is recorded for alternating incident powers of the mid-IR pulses as well for different wavelengths. We observe that for all wavelengths, the PMT responses agree well with the FN-fit for lower field strengths (see inset figure 4.9). However, for the last two data points of the $4700\,\mathrm{nm}$ and $4800\,\mathrm{nm}$ as well for the last data point of the $8000\,\mathrm{nm}$ data set, the FN-emission predicts a stronger response than the measured signal. We assign this mismatch to the saturation of the PMT.

Multi-photon absorption as a possible mechanism for electron emission can be ruled out for two reasons. Firstly, multi-photon absorption would lead to a stronger signal for lower wavelengths which is not observed, and secondly, the polarization dependence of the PMT signal (see figure 4.6) would not be observed in case of multi-photon absorption.

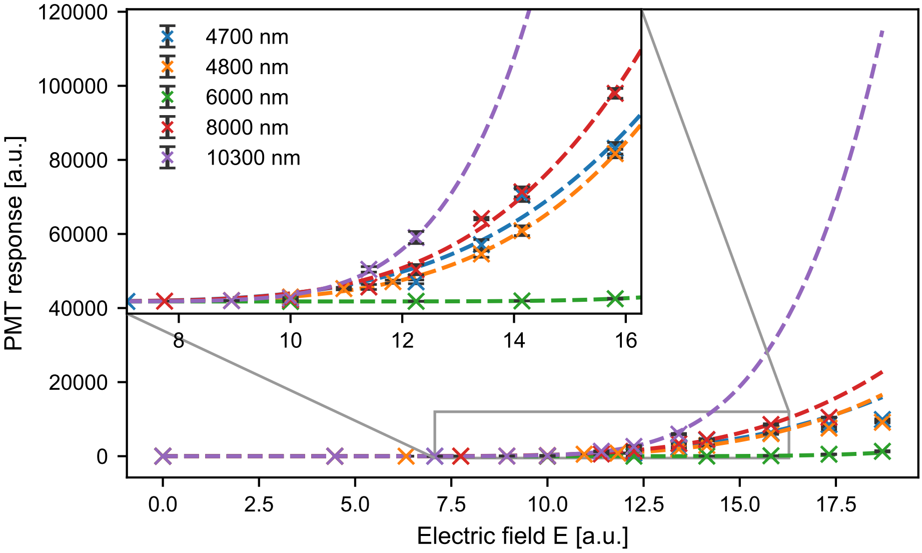

Figure 4.9. PMT responses for different incidence powers and wavelengths. The data are fitted with a standard FN-equation. For high power, the fit does not match the data anymore, attributed to the PMT's saturation. The inset shows a good match between fit and data in the lower power region.

4.3.2 Fowler-Nordheim-Autocorrelation

After the characterization of the PMT, we apply it to measure the iAC of the mid-IR pulses. Therefore, the experimental setup, shown in figure 4.3, is used. The delayed pulses incident collinearly onto the PMT and interfere with each other, causing a change in the field strength at the metasurface. This leads to a change in the local field enhancement and, consequently, to a modification of the FN current density. The change in the current density leads to a field-dependent signal measured by the PMT, which can be related to the field strength on the metasurfaces and, therefore, to the field of the mid-IR pulses.

Usually, the interferometric AC is based on second-harmonic generation in a crystal [137, 138] or on two-photon absorption on a photodiode [139, 140]. In that case, the AC signal is given by [141]

$$I_{ac}(\tau) = \int_{-\infty}^{\infty} \left| \left(E(t) + E(t-\tau)\right)^2 \right|^2 dt \quad . \tag{4.2}$$

Here, $I_{ac}(\tau)$ is the intensity measured by a slow detector as a function of τ, the delay time between the two pulses with the time-dependent electric field $E(t)$. The first square represents the second-order nonlinear process of the detection scheme and the other square and the integral are due to the slow response of the detector compared to the pulse duration. The evaluation of the expression under the integral leads to different contributions to the AC.

$$I_{ac}(\tau) = I_{back} + I_{int} + I_{\omega} + I_{2\omega} \tag{4.3}$$

A background term I_{back}, the intensity AC-term I_{int} and two interferometric terms I_{ω} and $I_{2\omega}$ oscillating with the frequencies ω and 2ω, where ω is the carrier frequency of the light field. Assuming an unchirped Gaussian pulse shape, equation (4.4) can be used to describe the measured intensity.

$$I_{ac}^{G}(\tau) = 1 + e^{-2ln(2(\frac{\tau}{w})^2} + 4e^{-\frac{3}{2}ln(2(\frac{\tau}{w})^2} \cos(\omega\tau) + e^{-2ln(2(\frac{\tau}{w})^2} \cos^2(\omega\tau) \tag{4.4}$$

Here is to mention that w is the FWHM of the optical pulse expressed in intensity.

In comparison to the standard second-order iAC, the nonlinear process applied in the PMT is the FN-non-linearity. The nonlinear medium is, in that case, the metasurface. The PMT structure is the slow detector. For a single pulse, the measured intensity by the PMT is given by

$$I \propto \int_{-\infty}^{\infty} a_n E(t)^2 \cdot e^{-k/|E(t)|} dt \quad . \tag{4.5}$$

To improve the readability of the equation, the terms ϕ and b_n have been grouped into the variable k. It should be noted that the field enhancement factor β has already been incorporated into $E(t)$. Inserting the interfering electric fields $E(t) + E(t-\tau)$ in equation (4.5) leads to the FN-AC-equation:

$$I_{FN} \propto \int_{-\infty}^{\infty} a_n \left[E(t) + E(t-\tau)\right]^2 \cdot e^{-k/[E(t)+E(t-\tau)]} dt \tag{4.6}$$

This equation describes the response of the PMT when two mid-IR pulses are interfering at the metasurface. As one can see from equation (4.6), the FN-AC- signal for relative low field strengths is dominated by the exponential function. However, for significantly strong fields, the signal will be equivalent to the one of a field-AC. This was already mentioned in the supplementary material of [136] by G. Herink et al.. Nonetheless, it has to be mentioned that G. Herink does not explicitly state the mathematical formalism of the FN-AC.

We perform experimental measurements of the mid-IR pulse AC using both a PD with two-photon absorption and the PMT. However, the band-gap of the PD material restricts us to wavelengths lower than $5.5\,\mu\text{m}$, while the FN-AC carried out with the PMT is limited to $7.5\,\mu\text{m}$ due to losses in the optical setup and decreasing output power of the DFG for longer wavelengths.

AC based on Two-Photon Absorption We shall start with the iAC based on two-photon absorption to characterize the mid-IR pulses with a well-known technique. Therefore, the two-photon signal of the PD is matched with the calculated iAC described in equation (4.4) presumed that the beam exhibits Gaussian properties. The wavelength of the mid-IR pulse is known from the fast fourier transform (FFT) of the AC-signal and is used for the fitting.

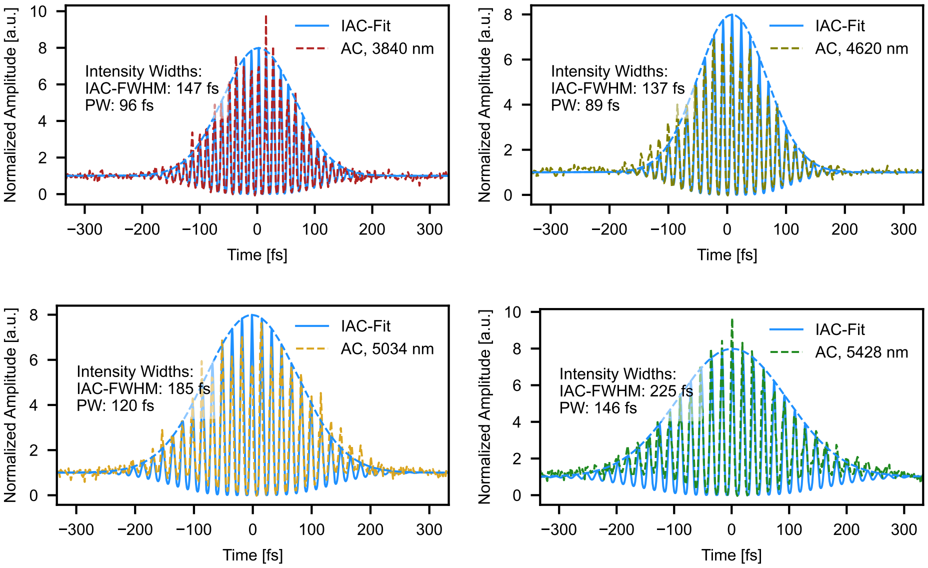

Figure 4.10. Recorded interferometric AC signals determined by 2-Photon absorption on a PD and the corresponding fits. The intensity FWHMs of the iAC (iAC FWHM) and the input pulse (PW) are shown. An increase in the pulse width for longer wavelengths is observed.

The AC signals for the selected wavelength and the corresponding fits are displayed in figure 4.10. We learn from the AC, that the pulse width elongates slightly when applying longer wavelengths. At $3840\,\mathrm{nm}$, the FWHM is $99\,\mathrm{fs}$, while for $5428\,\mathrm{nm}$, it is $148\,\mathrm{fs}$. Due to the change of wavelength for different pulse durations, the numbers of field oscillation periods in the FWHM can be seen as constant (± 2) for all measured wavelengths. This is determined by counting the number of field oscillations and dividing it by the FWHM and is just an observation in the recorded data. Unfortunately, as mentioned above, the AC can only be performed up to $5500\,\mathrm{nm}$. No statement can be made about the pulse duration and the number of field oscillations of a pulse with longer wavelengths. However, we expect pulse durations of similar lengths. Hence, we assume that the contribution to the increased PMT response for longer wavelengths ($9.5\,\mu\mathrm{m}$ to $11\,\mu\mathrm{m}$) cannot be explained by the elongation of the pulses. Moreover, as we will see later in the discussion, an increase in pulse duration while maintaining the optical power is causing a reduction in the PMT response.

AC based on FN-field Emission With the knowledge about the pulse duration of the mid-IR pulses, the recordings of the AC applying the PMT as a non-linear medium and detector are presented and then discussed. We call those AC from now on Fowler-Nordheim-ac (FN-AC). The measurable spectral range for the 2-photon AC is limited by the type of the nonlinear material. That is not the case for applying the PMT as a non-linear medium. The limitations here are, on the one hand, the wavelength-dependent response curve (see figure 4.5) and, on the other hand, the already above-mentioned decrease in power for longer wavelengths generated by the nDFG. The AC with the longest wavelengths recorded by the PMT is $7168\,\mathrm{nm}$ (See figure 4.11). As we can see from figure 4.11, for the same incident power of $400\,\mathrm{uW}$, the signal-to-noise ratio varies dramatically for different wavelengths. For that reason, for most of the following discussion, the FN-AC-traces of wavelengths around $4500\,\mathrm{nm}$ are utilized.

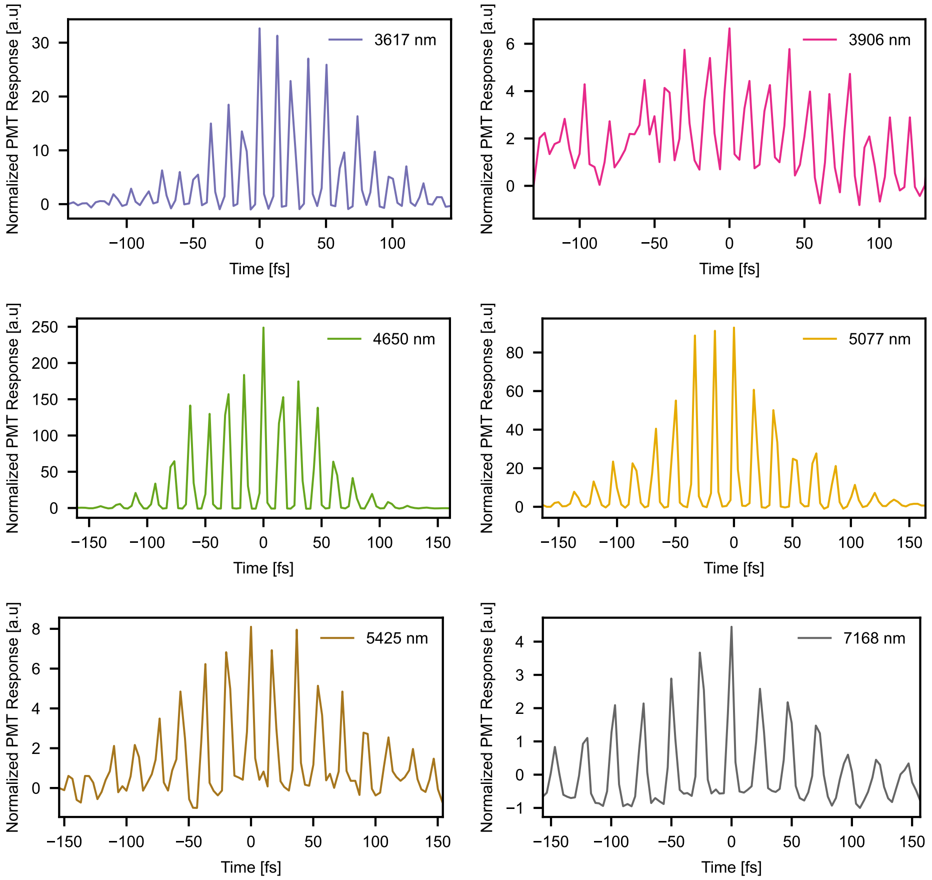

Figure 4.11. FN-AC-signals recorded with the mid-IR PMT for varying wavelengths but constant average power of $400\,\mathrm{uW}$.

We record FN-AC traces for different average powers at a wavelength of $4600\,\mathrm{nm}$. The used power range spans from 0 to $1.4\,\mathrm{mW}$. The beam is collimated with a $1/e^2$-widhts of $1/e_x^2 = 2.76\,\mathrm{mm}$ and $1/e_y^2 = 4.61\,\mathrm{mm}$, determined by a knife edge measurement. With the assumption of a Gaussian-pulse shape and the FWHM determined above, the incident field strength is calculated by applying equation (1.31).

Our data analysis has identified two distinct regimes that can be characterized using simplified versions of the mathematical expressions presented in equation (4.6). The first of these regimes corresponds to the baseline and can be modeled by assuming that the two input pulses arrive at the metasurface with a time delay τ such that they do not overlap in time. Additionally, the time interval between pulse arrivals is shorter than the PMT response time. The resulting PMT response can be modeled as the summation of two FN-emissions.

$$I_{base} = I_1 + I_2 \propto \int_{-\infty}^{\infty} a_n E_1(t)^2 \cdot e^{-k/E_1(t)} + a_n E_2(t)^2 \cdot e^{-k/E_2(t)}\ dt \tag{4.7}$$

The second regime corresponds to the maximum of the traces, where the two input pulses arrive at the metasurface with zero time delay ($\tau = 0$). In this scenario, the two pulses overlap perfectly, leading to constructive interference between the fields. As a result, the field emission is driven by the sum of the fields, which can be represented by the following equation:

$$I_{peak} =\propto \int_{-\infty}^{\infty} a_n \left[E_1(t) + E_2(t)\right]^2 \cdot e^{-k/[E_1(t)+E_2(t)]} dt \tag{4.8}$$

For the region between the maximum and the baseline, the full description given in equation (4.6) needs to be consolidated. We are applying equation (4.8) to determine the underlying coefficients needed for a numerical simulation of the FN-AC. Therefore, the center peak

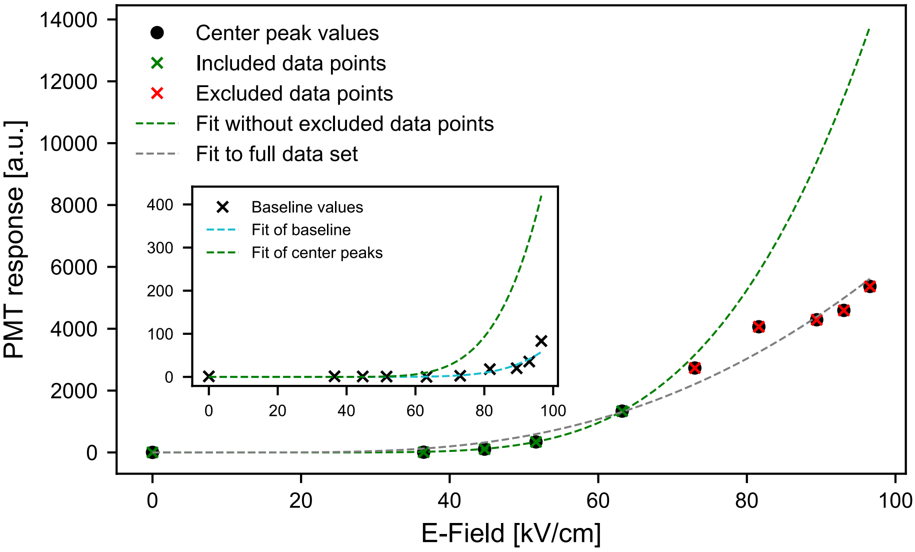

Figure 4.12. The figure shows the fit of the center peak values. The best fit is achieved by omitting the values for high field strengths. The inset shows the fit of the baseline compared to the fit of the center peaks.

values of the recorded traces are extracted and fitted with equation (4.8). The free parameters are β and a proportionality constant to translate the FN-current density to the intensity measured by the PMT. The fit can be seen in figure 4.12. Fitting all peak values leads to an unsatisfactory fit. Hence, we exclude data points for higher fields than $70\,\mathrm{kV\,cm^{-1}}$, which leads to a better fit. The exclusion of the data is justified by the saturation of the PMT, which is visible in the FN-AC-traces of fields higher than $63\,\mathrm{kV\,cm^{-1}}$ (see figure 4.13). The peaks around the center region ($\approx \pm 50\,\mathrm{fs}$) share a nearly identical high, which indicates PMT saturation.

We extracted as well the intensity baseline values of the power-dependent FN-AC traces and fitted those with equation (4.7). Here, the fitting provides a decent result. However, when applying the parameters determined by the fit of the center peaks in equation (4.7), the calculation predicts already a response for weaker fields than observed, although the determined values from the baseline fit underestimate the peak values dramatically. A possible explanation for the lower response for the baseline than expected from the fit of the peak values can be found in the threshold behavior of the PMT. Low energy electrons might not be as efficiently collected by the focusing electrode of the PMT or do not escape the near field region fast enough before the fast oscillating mid-IR field switches polarity. Moreover, it needs to be mentioned that a larger data set with more data points in the region up to $70\,\mathrm{kV\,cm^{-1}}$ would be beneficial for a more significant calculation of the parameters.

Using the determined parameters from fitting the center peak values, we simulate the full FN-AC traces to match the recorded data by applying equation (4.6). Therefore, we assume two identical Gaussian pulses $E(t)$ with a carrier frequency of $4610\,\mathrm{nm}$ interfering at a delay time τ. The electric field FWHM is $125.8\,\mathrm{fs}$ ($89\,\mathrm{fs}$ intensity FWHM) as determined by the 2-photon AC. The resulting electric field is then used in FN-equation to obtain the electrons emitted at any point in time t. Integration over t results in the signal recorded by the PMT at τ.

As one can see in figure 4.13, the data exhibit strong fluctuations caused by the instability of the output of the OPA and nDFG. The power fluctuations of the laser system get amplified in the PMT due to the high non-linearity of the FN-process. Little fluctuations in the field strength result in significant changes in the number of emitted electrons. Especially in the low-field regime, where the exponential function dominates the process. Moreover, the data expose some asymmetry which might be caused by a slight misalignment of the interfering beam. Those irregularities and imperfections make it challenging to accurately align the data with the simulation. However, the simulation captures all significant features, such as the correct width of the traces, the oscillation frequency, and the height of the side peaks in unsaturated traces. As mentioned before, besides the intensity fluctuations, the data expose some asymmetry. One side of the FN-AC traces is elongated. We attribute this asymmetry to the alignment of the autocorrelator. It is well known that interferometric AC requires exact alignment. Here to mention, the first datasets recorded with the FN-AC exhibit a double pulse structure caused by misalignment. The exact alignment requires an infrared beam profiler. Using liquid crystal detector cards and irises does not result in the here required precision.

Our simple model effectively captures the essential characteristics of the FN-AC and should now be used to investigate how the PMT responds to modifications in the FWHM, average power $\mathrm{P_{avg}}$, and the peak electric field strength $\mathrm{E_{peak}}$ of the beams. We specifically

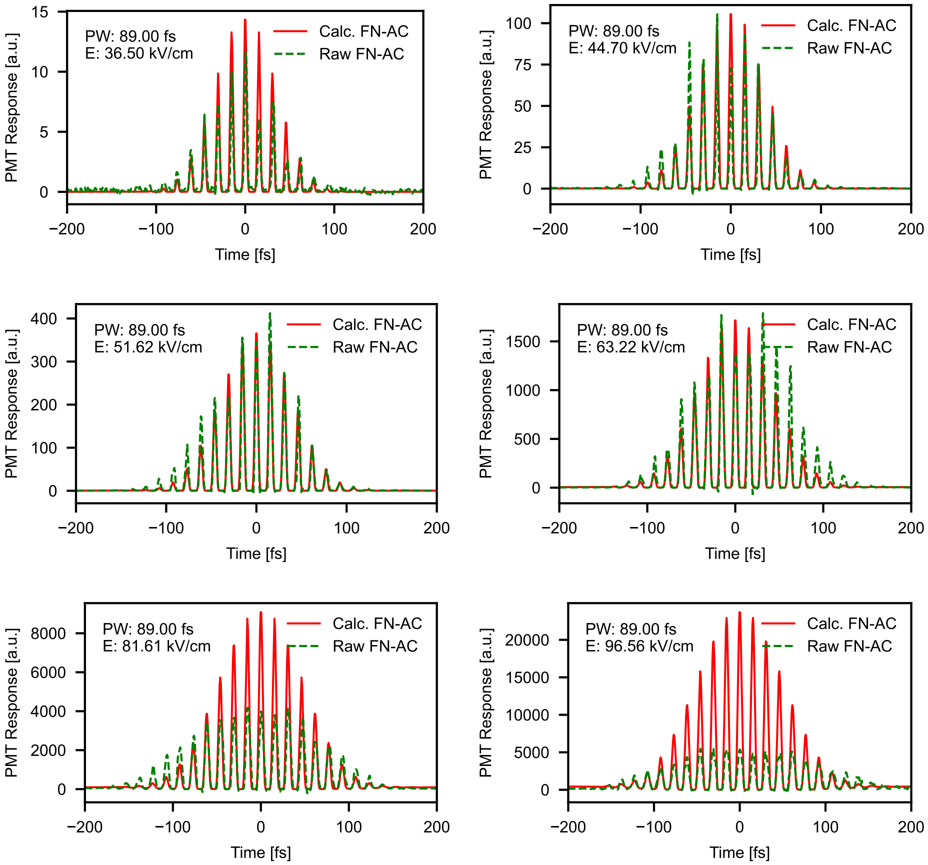

Figure 4.13. The figure shows a comparison of the recorded FN-AC traces (green) from the PMT with simulated data. The recorded traces exhibit saturation for field strengths greater than $70\,\mathrm{kV\,cm^{-1}}$, as indicated by a plateauing of the data. The red curves represent the simulated data.

look at the effects of changing the FWHM for fixed E_{peak}, FWHM for fixed P_{avg}, and E_{peak} for fixed FWHM. For all simulations, the underlying FN-equation is parametrized with the same values as determined above and used in the fitting of the FN-AC traces displayed in figure 4.13.

Variable E_{peak} for fixed FWHM The FWHM of the electric field of the two pulses for the inquiry of the peak field strength variation is $88\,\mathrm{fs}$ in the electric field of the incoming pulses. The field variations are inspected for lower fields and higher fields up to $1\,\mathrm{MV/cm}$ per single pulse. The simulation results are displayed in figure 4.14 in (a) lower fields and in (b) higher fields. The red dots denote the half-maxima of the iAC. The background signal (baseline) is removed for better visibility of the signals. The signals lower than the baseline are not shown as well. In the lower field regime, the FWHM of the FN-ACs broaden quickly in a non-linear manner. When the fields increase in strength, the slope of the broadening decreases rapidly and the width approaches for high fields the width of the field-AC of the pulses (dashed black line). Looking at equation (4.6), one can see that this behavior is expected. For low fields, the exponential function changes rapidly, and for high fields, it approaches 1 so that the squared sum of the fields dominates the measured intensity. On that account, pulse

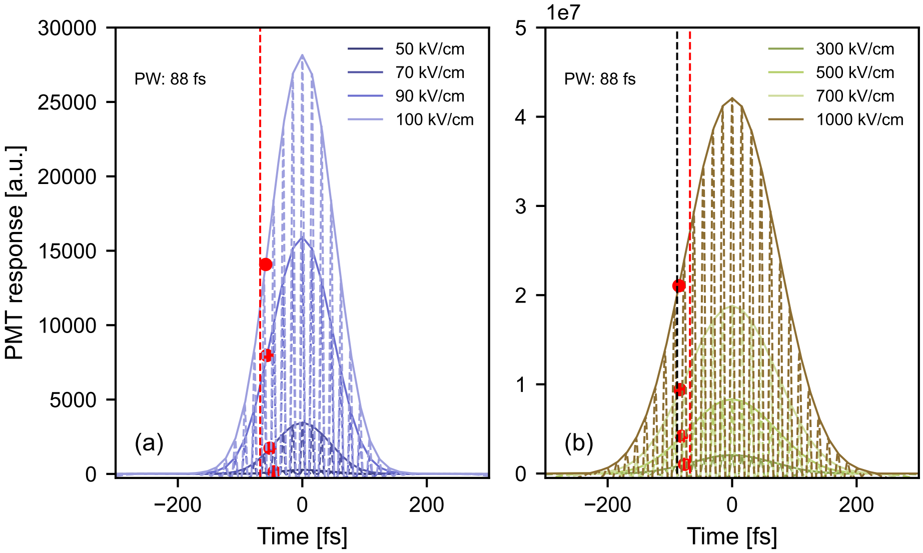

Figure 4.14. Calculated FN-ACs for a varying field strength of the impinging pulses while the pulse widths are kept constant at $88\,\mathrm{fs}$ for the electric field. In (a), the field strengths are about the same as in the experiment, while in (b), the fields up to $1\,\mathrm{MV/cm}$ are applied. The red dots mark the development of the half-maximum for the different field strengths. The red dashed line displays the widths of a 2-photon iAC, and the black dashed line corresponds to the widths of the field AC

.

widths could not be retrieved for fields exceeding a certain strength [142]. In the simulated data, a field strength of about $150\,\mathrm{kV\,cm^{-1}}$ exhibits a AC-width of the predicted second-order nonlinear AC (red line). For stronger fields, the retrieval of the pulse length might be questionable. Hence, we define $150\,\mathrm{kV\,cm^{-1}}$ as a lose threshold. Beyond it, the pulse should not be determined with the PMT.

Analyzing the spectral content of the FN-ACs (see figure 4.15), we observe that many harmonics of the optical frequencies are contributing to the signal. However, the stronger the field, the more dominant becomes the fundamental frequency. This reflects, again, that the non-linearity of the FN process is stronger for lower fields. The higher harmonics appear as

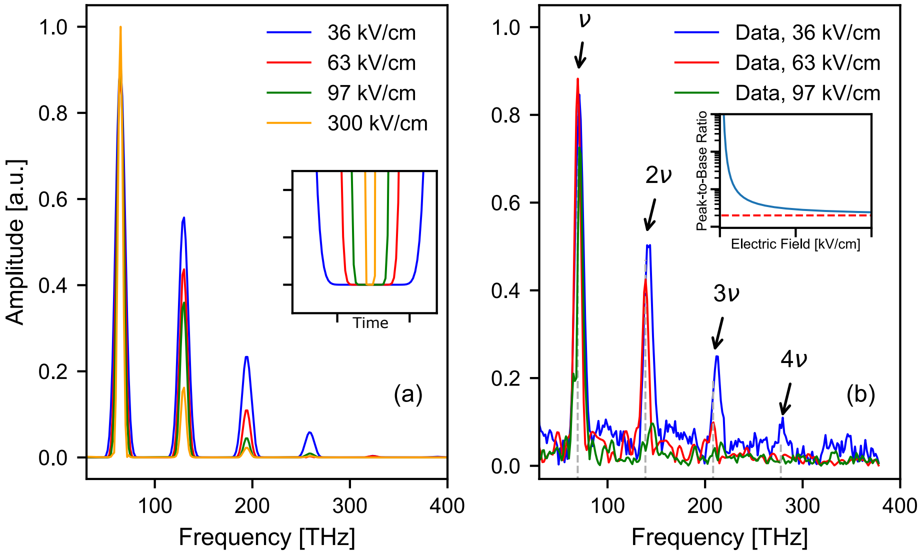

Figure 4.15. FFT of the calculated (a) and measured (b) FN-AC traces. Higher harmonics contribute to the signal. The inset in (a) shows one minimum of the time traces. The inset in (b) illustrates the peak-to-baseline ratio for different fields.

well in the FFT of the measured traces. For the lowest field of $36\,\mathrm{kV\,cm^{-1}}$, frequencies up to the fourth harmonic are manifested before disappearing in the noise level. This matched well with the simulation. Higher fields as $97\,\mathrm{kV\,cm^{-1}}$ cause less contribution of the higher harmonics. In the data, the second harmonic is barely visible, which is an indicator that already this AC trace exhibits more similarities with the field AC. In the simulation, even higher fields show a stronger contribution of the second harmonic. This might indicate a mismatch in the calibration of the underlying parameters for high fields. The supposed origin of the higher harmonic content is the flat nulling of the signal when the fields interfere destructively. The high non-linearity of the process leads to a square-like shape. For higher fields, the time for zero signal decreases, which causes a reduction in the higher harmonic contribution. This is shown in the inset of (a). The inset of (b) shows the ratio between the peak and the baseline, which also reflects the non-linearity of the process. For small fields, the ratio is extremely high, while for high fields, a constant value of 2 is approached, which is the limes for strong fields when dividing equation (4.8) by equation (4.7). Hence, the ratio between peak and baseline could be used as an additional indicator for the underline nonlinearity, as mentioned by [142].

Simulation for a varying field strength showed again the nonlinearity of the FN-emission, which makes it difficult to employ this effect for an exact determination of the pulse width. Small changes in the field cause big changes in the measured width of the AC traces. The field strength becomes a crucial element in order to find the pulse width.

Variable FWHM for fixed E_{peak} Above, the behavior of the field strength on the emission process was discussed and it concluded that fields less than $150\,\mathrm{kV\,cm^{-1}}$ should be applied to stay in a nonlinear regime that can be applied to measure the pulse width. Hence, to study the behavior of the PMT response for ACs of pulses with different pulse widths, a moderate peak electric field of $63\,\mathrm{kV\,cm^{-1}}$ is utilized. The FWHMs from $50\,\mathrm{fs}$ to $275\,\mathrm{fs}$ with a step of $25\,\mathrm{fs}$ are selected. We observe a linear increase of the width of the AC for increasing FWHMs while the peak-to-baseline ratio stays constant, as can be seen in figure 4.16. This behavior is expected due to the increase in the interference region of the two pulses, which

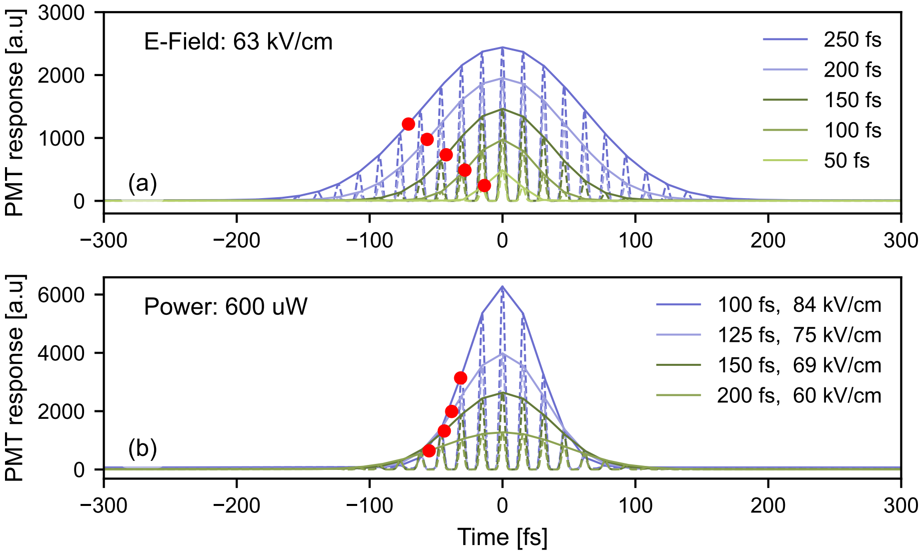

Figure 4.16. Simulation results for varying pulse widths. In panel (a), the pulse electric field of the pulses is kept constant at $63\,\mathrm{kV\,cm^{-1}}$. Panel (b) displays the PMT response for constant power of $600\,\mathrm{\mu W}$. The red dots indicate the half-width of the AC.

causes the broadening of the AC width, while the maximal peak field strength does not change, and hence no change in the peak-to-baseline ratio is introduced.

Variable FWHM for fixed P_{avg} As it is easier to measure the average power of the used laser system than it is to extract the peak field strength of the pulse, simulations for a fixed average power and varying FWHMs of the mid-IR pulses are performed. This leads to a nonlinear behavior of the width of the AC traces as seen in figure 4.16 b) caused by the change in the peak field strength of the pulse when the width of it is varied. This adds complexity to the experimental realization of observing the broadening of the pulse, as mentioned above.

In the following, the sensitivity of the FN-AC with respect to chirp and side pulses are discussed based on the simulation. The here chirped pulses have all the same Gaussian envelope and simply a chirp added. The chirp is not acquired by propagation through a dispersive medium. It is known that a second-order iAC reveals the linear chirp of a pulse. The simulations should be used to evaluate the impact of chirped pulses on the FN-AC. In figure 4.17 (a), a simulation of the FN-AC for chirped pulses, and in figure 4.17 (b), the one of a 2-photon iAC can be seen. Here, the magnitude of the chirp is adjusted by the parameter b, which lowers or increases the quadratic phase of the pulse. All pulses have the same Gaussian envelope with a width of about 88 fs. The envelope of an unchirped pulse is indicated in (a) and (b) by a dashed black line. For a $b = 1$, the chirp is in (b) clearly visible and leads to the characteristic wings of the trace. Visible, but not as pronounced, is the chirp in the FN-AC.

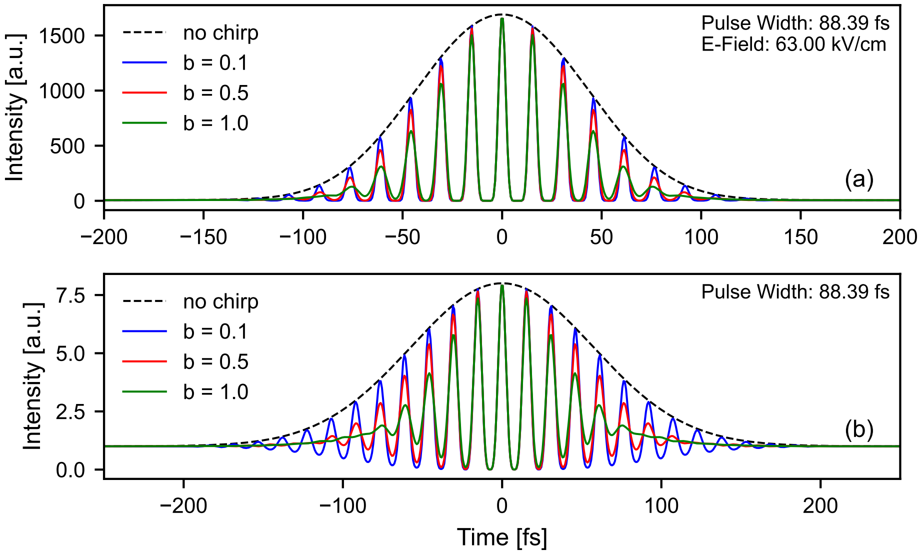

Figure 4.17. AC simulation of linear chirped pulses. In (a), the FN-AC for different magnitudes of the chirp. In (b), the 2-photon AC for the same pulses is displayed.

Also, here, the characteristic wings are developed, but due to the lower field strength at the sides, a significantly weaker signal compared to the max. value is detected. With decreasing the chirp, the signals approach the envelope of the unchirped pulse. In the simulations, for $b = 0.5$, there is still a significant difference compared to the unchirped pulse at the sides of the traces. However, experimentally it is challenging to resolve this difference due to the noise level. Despite the high non-linearity of the FN-emission, it does not hinder the detection of a linear chirp in the pulses when utilizing the PMT in an iAC. However, the extensive dynamic range of the PMT poses challenges in accurately resolving the chirp. Additionally, the sensitivity to fluctuations at low field strength further complicates the observation of the chirp.

4.4 Conclusion

In conclusion, the presented chapter provides a comprehensive overview of a PMT in mid-IR based on electron field emission from metal antennas and its potential as a detector for mid-IR radiation. As a potential application, iAC experiments of mid-IR pulses were performed and described with sufficient accuracy by the here proposed model.

The chapter started by introducing the experimental setups followed by the characterization of PMT by means of power, wavelength, and polarization-dependent measurements, supported by the study of the metasurfaces applying FTIR-measurements and COMSOL®-simulations to add enhanced knowledge to the underlying processes. Those studies showed the capability of the PMT to measure a wavelength range from $3.6\ \mu\mathrm{m}$ to $10.7\ \mu\mathrm{m}$. The investigation towards longer wavelengths was limited by the used mid-IR source and the window material. However, the wavelength response showed that distinct wavelengths are preferred for a strong PMT signal. In order to understand the underlying mechanism for that, the FTIR and COMSOL® were employed, leading to the understanding that the far field response, measured by the FTIR, does not match with the near field response of the antenna and that the PMT response curve can mainly be attributed to a near field response of the metasurface.

The basic characterization was followed by showcasing a potential application of the PMT in an iAC setup as a detector and non-linear medium. The PMT was compared to a standard 2-photon based iAC. Moreover, a model to describe the PMT response to the interfering pulse was provided and used to calibrate the PMT. The model leads to a good agreement with obtained measurements. The model was used to investigate the behavior of the PMT for different beam parameters such as FWHM, electric field strength, average power, and chirp. The results direct towards the conclusion that for unknown field strength and pulse duration, the PMT cannot retrieve an exact pulse duration due to the fact that the response is non-linearly dependent on both parameters. However, a rough estimate can be made. Careful calibration of the PMT response could improve the validity of the pulse width.

Nevertheless, the significance of the new PMT as a tool for the detection of mid-IR radiation is valid. The big advantage is the wide response range in wavelength as well as in input power due to the adjustable gain. The usefulness of the new tool can be improved by adding a variety of different antennas close to each other to fill the gaps in the wavelength response and by switching from the MgF_2-window to e.g. zinc selenide, which exhibits a flat transmission of 70 % up to $20\,\mu m$.

Conclusion

The aim of the presented thesis was to examine field-triggered electron emission processes to gain a better understanding of them and find their limitations and opportunities for future research. This was done by studying two different fields of research. The first investigation was trying to answer the more fundamental question of whether the THz field can emit electrons from metasurfaces in a liquid environment and whether the strong field itself is affecting the sample. In comparison, the second examination was centered on applying the field emission process in technological application and moving away from the THz toward the mid-IR region.

The doubt about the possibility of electron field emission into a liquid medium has been dispelled by the experiments presented in chapter 3 by the observation of light emission from dye molecules dissolved in polar and non-polar liquid solvents when the THz field incidents onto the metasurface. The question of whether the strong field affects the sample could not be fully answered. However, the recorded measurements of the light emitted from the liquid samples exhibited a deviation from the expected FN-trend, which led to the phenomenological derivation of a correction constant taking different field-induced effects into account and might provide information on how much the measured results deviate from the traditional FN-emission. Measurement of electron-induced light emission from gases supports the argument of additional field-induced effects in the liquid samples. Moreover, performed simulations of the electron acceleration in the THz field additionally showcased the importance of the recognition of the potential barrier shape in field emission processes. Those results are highly important for the design of an experiment in which the field-emitted electrons are applied to directly trigger chemical reactions in liquid samples and their investigation in an ultrafast time-resolved measurement. A potential future experiment is to measure the solvation of the electrons in the water. It has an important role in many chemical processes [143]. Most studies of it generate the electron in the water by photoionization [144, 145]. However, our technique would allow us to inject an electron into the water directly. One of the key objectives of this thesis was to examine the feasibility of direct electron injection into a liquid medium. The studies in chapter 3 highly suggest the possibility of the THz-induced electron field emission into liquid water. The hydrated electron exhibits absorption of $800\,\mathrm{nm}$ light [146], which allows us to probe the solvation process of the electron on an ultrafast timescale. This experiment was already designed during the studies for this thesis. Therefore a commercial liquid sample cell (GS20580 Series, Specac) provided a 100 µm thick water film between two Quartz windows. One of them had the micro antennas imprinted. The probe beam was focused through the gap of the dSRR. Due to high laser noise levels and time limitations, the preliminary measurements did not yield a successful result. However, the results of chapter 3 suggest the potential for a positive outcome of the time-resolved measurement, which is worthwhile to pursue because of gaining valuable insights and knowledge about the solvated electron.

The second experimental part of the thesis chapter 4 was centered around the investigation of a new field emission based PMT in the mid-IR region. Characterization of the device was performed, leading to the result of a detection bandwidth from about $3.7\,\mu\mathrm{m}$ to $11\,\mu\mathrm{m}$ when the window absorption is accounted for. Otherwise, the bandwidth only reaches $8.5\,\mu\mathrm{m}$. The wavelength response exhibits regions of high sensitivity, while for other wavelengths, the signal is barely detectable. Concluding that the PMT response is highly dependent on the design of the metasurface. Additionally, the use case of the device for measuring the interferometric autocorrelation of mid-IR pulses showed that the recording of an autocorrelation trace is possible. However, the extraction of the exact pulse width is hard to determine without prior assumptions about the electric field strength of the pulse. Moreover, simulations of the autocorrelation gave insights into the behavior of the autocorrelation width on the experimental parameters.

The relevance of the study of the new device is of technological interest. It showcases a potential application of the PMT and its limitations which enables the improvement of the device to provide an alternative to already existing mid-IR detectors. A possible improvement for the future is the replacement of the window material to enhance the device's bandwidth. Moreover, adding antennas with different frequency responses to the metasurface will help to close the gaps in the wavelength-dependent response, which makes the detector more useful for detection applications.

During the preparation of this thesis, novel experimental setups were constructed for the experiments presented in chapter 3 and chapter 4. The process of designing and building these setups enabled the acquisition of crucial skills in optical setup construction and design. In addition to the presented setups, a LN based THz setup with a step-stair echelon was built during the 4-month external research stay at the University of McGill in Montreal, Canada. The aim during the research stay was to apply the THz field to emit electrons from a tungsten tip and use those electrons to trigger chemical reactions. The project did not lead to any positive results due to problems in confirming good conditions for electron emission. Here, light emission due to electron release from a metasurface into Argon gas would have been beneficial to confirm that the field strength is sufficient for electron emission.

The research project required me to spend many hours in the optical laboratory to construct and optimize the setup. This tedious work taught me persistence and patience, which directed me to my passion for the design and construction of optical setups. Moreover, I had the chance to work with many amazing people and learn from them important skills.

To summarize: The thesis' importance lies in showcasing the broad possibilities enabled by electron field emission. The more fundamental science results for light emission in gases and liquids pave the way to time-resolved electron-pump optical-probe spectroscopy without the need for additional electron optics. While the technological part, by applying field emission for light detection, gives insight into the possible application of such a detector. I hope this thesis adds another piece to the broader picture of electron field emission and its potential impact on various fields of science and technology.

Appendices

Publications and Contributions

Publications

- Simon J. Lange, Tobias O. Buchmann, Matej Sebek, Malte L. Welsch, Edmund J. R. Kelleher, Naoya Kawai, Hisanari Takahashi, Kota Katsuyama, Peter U. Jepsen, "*Lightwave-driven long-wavelength photomultipliers*," Laser & Photonics Reviews, (**submitted**)
- Malte L.Welsch, Martin J. Cross, Tobias O.Buchmann, Simon J. Lange, Edmund J. R. Kelleher, Peter U. Jepsen, "*Autocorrelation with novel field-driven photomultiplier for mid-infrared light*", (**in preperation**)
- Malte L.Welsch, Martin J. Cross, Lars R. Lindvold, Simon J. Lange, Edmund J. R. Kelleher, Peter U. Jepsen, "*Electron field emission into liquids and gases: exploring tunnel ionization effects and their influence*" (**in preperation**)

Conference Contributions

- Malte L.Welsch, Martin J. Cross, Lars R. Lindvold, Simon J. Lange, Edmund J. R. Kelleher, Peter U. Jepsen, "*Light Emission from Gases and Liquids Excited by THz-Driven Field-Emitted Electrons*", Optical Terahertz Science and Technology (OTST), 2022, Budapest,(**talk**)
- Simon L. Lange, Malte Lasse Welsch, Naoya Kawai, Peter U. Jepsen, "*Sensitivity characterization of a photomultiplier tube for terahertz radiation*," 2021 46th International Conference on Infrared, Millimeter and Terahertz Waves (IRMMW-THz)

Abbreviations

AC	Auto-Correlation
BS	Beamsplitter
CCD	Charge-Coupled Device
DAQ	Data Acquisition
DFG	Difference-Frequency Generation
DP	Dielectric Polymer
DTU	Technical University of Denmark
dSRR	double Split-Ring Resonator
EO	Electro-Optic
EOS	Electro-Optic Sampling
EtOH	Ethanol
FEL	Free-Electron Laser
FFT	Fast Fourier Transform
FTIR	Fourier-Transform Infrared Spectroscopy
FN	Fowler-Nordheim
FN-AC	Fowler-Nordheim-Ac
FWHM	Full-Width Half-Maximum
iAC	Interferometric Auto-Correlation
LPF	Longpass Filter
LN	Lithium Niobate, $LiNbO_3$
MC	Monte-Carlo

mid-IR	mid-Infrared
ND	Neutral Density
nDFG	nonlinear Difference Frequency Generation
OAP	Off-Axis Parabolic Mirror
OPA	Optical Parametric Amplifier
OR	Optical Rectification
PCA	Photoconductive Antenna
PD	Photodiode
PM	Power Meter
PMT	Photo-Multiplier-Tube
SFG	Sum-Frequency Generation
SEM	Scanning Electron Microscope
SHG	Second-Harmonic Generation
SN	Schottky-Nordheim
STM	Scanning Tunneling Mircroscope
THz	Terahertz
TPF	Tilted Pulse Front
TDS	Time-Domain Spectroscopy
UV	Ultraviolet
WGP	Wire Grid Polarizer
ZnTe	Zinc Telluride

List of Symbols

The following list presents a number of symbols that will be utilized later on in the document.

$\hbar$	Reduced Planck constant
π	Pi
c	Speed of light in a vacuum
e	Elementary charge
h	Planck constant
k_B	Boltzmann constant
m_e	Electron mass

List of Figures

1.1 In a) the electro-optical Cerenkov effect and in b) the THz generation by tilted pulse front is schematically depicted. 10

1.2 Schematic drawing of the THz generation scheme used for the performed experiments. 13

1.3 Basic Principle of EO-sampling. The THz pulse induces birefringence into the EO-crystal, which changes the polarization of the probe beam. The displayed detection scheme measures the difference in intensity in different components of the polarization. 15

2.1 Images of the dSRR. In a), the dSRRs applied for the investigation in [89] are displayed. In b), a finite element simulation of the field distribution of a dSRR, when illuminated with THz radiation, is shown. One can see that the field is enhanced in the gap region of the emitter. The pictures are taken from [89] with the permission from S. Lange. 25

3.1 Experimental setup for direct electron injection into gases or liquids by means of THz-driven field emission. In (a), the setup, including the DAQ-system, is depicted. A more detailed view of the sample cell and detection is presented in (c). The applied EOS-setup for measuring the time trace of the THz pulse can be seen in (b). 33

3.2 Structural chemical formulas of the solvents Ethanol (a) and silicone oil (b) for the fluorescent dye Fluorescent Yellow 3G. The dyes formula is depicted in (c). . . . 34

3.3 Camera image of the illuminated metasurface in Argon gas. The light emission from single antennas is clearly visible (a). Zoom on a high-emission antenna (b). A two-dimensional Gaussian fit provides an interaction radius of about 20 μm. . 35

3.4 THz waveform detected with EO-sampling. The inset illustrates the spectrum of the pule. The waveform includes a prepulse and the first echo from the Si-window in the beam path. 36

3.5 Field-dependent light emission from Argon and ambient air detected with a PMT and fitted with a FN-fit. The PMT-response is plotted over the impinging THz peak field strength (a) and fitted with a FN-fit. In (b), the residuals are displayed. Additionally, in c), the truncated FN-plot for a fit without the constant d, and in d), the FN plot for a fit including d is presented. Here, an additional offset of 10 is added to the data. 38

3.6 Field-dependent light emission from dye-doped EtOH and silicone oil. The recorded data are fitted with an FN-fit. The fit exhibits clear mismatches to the data, which can be clearly seen in the residuals of the fit. 39
3.7 The data of the light emission from liquids fitted by adaption of the equation for tunnel ionization. 40
3.8 Light emission data fitted with the FN-equation compared to a fit through an adaption of the equation for tunnel ionization (a). In (b) are the residuals presented, which show that both fits lead to nearly the same result. The differences between the two fit-function can be seen in (c). 41
3.9 FN plots for the liquid samples. In a), the standard FN plot is shown. In b), the FN plot for taking α into account is presented. 44
3.10 The majority of electrons are emitted around the peak of the THz field. The FWHM of the electrons is here 100 fs. 46
3.11 Pressure dependence of the distribution of the maximum kinetic energy (a) and traveled distance (b) of the electron. 47
3.12 The figure presents the simulation results for every electron emitted along the THz pulse. The distance, energy, and collisions for each electron can be seen. The grey background indicates that the termination event of the simulation occurred. . . . 48
3.13 The number of collisions for electrons emitted along a THz-pulse for different β-values are presented. 49
3.14 In panel (a), the recorded Argon data is matched with the simulation. The number of collisions is weighted by the number of emitted electrons according to the field enhancement factor. In (b), the residuals between the recorded data and the matched simulations for a SN-barrier shape are shown. 50

4.1 Schematic of a PMT. When light hits the photo-cathode, it emits a primary electron, which is then multiplied by the dynodes. This multiplication process allows for small signals to be amplified and measured. 55
4.2 Schematic drawing of the experimental setup for the characterization of the mid-IR-PMT. 56
4.3 Schematic drawing of the experimental setup to perform auto-correlation measurements. 57
4.4 FTIR measurements of MgF_2-window with thickness $1.58 \pm 0.01\,\mathrm{mm}$. In (a) the transmission for wavelengths for $2.4\,\mu\mathrm{m}$ to $14\,\mu\mathrm{m}$ is presented. The step cut-off is clearly visible. (b) shows the rotation independence of the transmission of the window. The slight birefringence does not affect the transmission significantly. . 59
4.5 Wavelength response of the PMT. Responses accounting and not accounting for the absorption of the window are shown. In a), the mid-IR beam is collimated, while in b), the beam is focused. 60
4.6 Rotation-dependent PMT response for different wavelengths (a) and FTIR measurements of the metasurfaces for different orientations (b). In the rotation-dependent response, two pronounced resonances at about 0° and 180° are clearly visible. The FTIR measurements show for both orientations an increase in extinction for longer wavelengths. 62

4.7 a) simulated wavelength response of metasurface (green and red line). The green line shows the in-plane field enhancement $|E_x|$, whilst the red line is the out-of-plane component $|E_z|$. The shaded area is the measured PMT response. b) Simulated antenna response for an incident field with a wavelength of $10.1\,\mu\mathrm{m}$. The field is strongly enhanced in the antenna gap. 63

4.8 Comsol simulation of the transmitted field through the antenna compared to the FTIR measurements. a) Comsol simulation for polarization along the x-axis compared to the 90° FTIR measurement. b) Comsol simulation for polarization along the y-axis compared to the 0° FTIR measurement. 64

4.9 PMT responses for different incidence powers and wavelengths. The data are fitted with a standard FN-equation. For high power, the fit does not match the data anymore, attributed to the PMT's saturation. The inset shows a good match between fit and data in the lower power region. 65

4.10 Recorded interferometric AC signals determined by 2-Photon absorption on a PD and the corresponding fits. The intensity FWHMs of the iAC (iAC FWHM) and the input pulse (PW) are shown. An increase in the pulse width for longer wavelengths is observed. 67

4.11 FN-AC-signals recorded with the mid-IR PMT for varying wavelengths but constant average power of $400\,\mathrm{uW}$. 68

4.12 The figure shows the fit of the center peak values. The best fit is achieved by omitting the values for high field strengths. The inset shows the fit of the baseline compared to the fit of the center peaks. 69

4.13 The figure shows a comparison of the recorded FN-AC traces (green) from the PMT with simulated data. The recorded traces exhibit saturation for field strengths greater than $70\,\mathrm{kV\,cm^{-1}}$, as indicated by a plateauing of the data. The red curves represent the simulated data. 71

4.14 Calculated FN-ACs for a varying field strength of the impinging pulses while the pulse widths are kept constant at $88\,\mathrm{fs}$ for the electric field. In (a), the field strengths are about the same as in the experiment, while in (b), the fields up to $1\,\mathrm{MV/cm}$ are applied. The red dots mark the development of the half-maximum for the different field strengths. The red dashed line displays the widths of a 2-photon iAC, and the black dashed line corresponds to the widths of the field AC . 72

4.15 FFT of the calculated (a) and measured (b) FN-AC traces. Higher harmonics contribute to the signal. The inset in (a) shows one minimum of the time traces. The inset in (b) illustrates the peak-to-baseline ratio for different fields. 73

4.16 Simulation results for varying pulse widths. In panel (a), the pulse electric field of the pulses is kept constant at $63\,\mathrm{kV\,cm^{-1}}$. Panel (b) displays the PMT response for constant power of $600\,\mu\mathrm{W}$. The red dots indicate the half-width of the AC. . 74

4.17 AC simulation of linear chirped pulses. In (a), the FN-AC for different magnitudes of the chirp. In (b), the 2-photon AC for the same pulses is displayed. 75

List of Tables

1.1 Optical and electro-optical properties of selected materials. 9

3.1 Fitting parameters α and the corrected values for the field enhancement β_{new} compared to β return for the FN-equation. 42

Bibliography

[1] C. Kleint, “On the early history of field emission including attempts of tunneling spectroscopy,” *Progress in Surface Science*, vol. 42, no. 1-4, pp. 101–115, 1993.

[2] J. J. Thomson, “XL. Cathode Rays,” *The London, Edinburgh, and Dublin Philosophical Magazine and Journal of Science*, vol. 44, pp. 293–316, 10 1897.

[3] J. E. Lilienfeld, “The auto- electronic discharge and its application to the construction of a new form of X-ray tube,” *American J. of Roentgenology*, vol. 9, no. 3, pp. 172–179, 1922.

[4] R. G. Forbes, “Use of Millikan-Lauritsen plots, rather than Fowler-Nordheim plots, to analyze field emission current-voltage data,” *Journal of Applied Physics*, vol. 105, no. 11, 2009.

[5] R. H. Fowler and L. Nordheim, “Electron emission in intense electric fields,” *Proceedings of the Royal Society of London. Series A, Containing Papers of a Mathematical and Physical Character*, vol. 119, pp. 173–181, 5 1928.

[6] J. A. Panitz, “Field-ion microscopy - A review of basic principles and selected applications,” *Journal of Physics E: Scientific Instruments*, vol. 15, no. 12, pp. 1281–1294, 1982.

[7] J. Pawley, “The development of field-emission scanning electron microscopy for imaging biological surfaces,” *Scanning*, vol. 19, no. 5, pp. 324–336, 1997.

[8] N. Boroumand, A. Thorpe, A. M. Parks, and T. Brabec, “Keldysh ionization theory of atoms: Mathematical details,” *Journal of Physics B: Atomic, Molecular and Optical Physics*, vol. 55, no. 21, 2022.

[9] F. Kusa, K. E. Echternkamp, G. Herink, C. Ropers, and S. Ashihara, “Optical field emission from resonant gold nanorods driven by femtosecond mid-infrared pulses,” *AIP Advances*, vol. 5, no. 7, pp. 1–6, 2015.

[10] K. E. Echternkamp, G. Herink, S. V. Yalunin, K. Rademann, S. Schäfer, and C. Ropers, “Strong-field photoemission in nanotip near-fields: from quiver to sub-cycle electron dynamics,” *Applied Physics B: Lasers and Optics*, vol. 122, no. 4, pp. 1–10, 2016.

[11] G. Herink, L. Wimmer, and C. Ropers, “Field emission at terahertz frequencies: AC-tunneling and ultrafast carrier dynamics,” *New Journal of Physics*, vol. 16, 2014.

[12] D. Matte, N. Chamanara, L. Gingras, L. P. De Cotret, T. L. Britt, B. J. Siwick, and D. G. Cooke, “Extreme lightwave electron field emission from a nanotip,” *Physical Review Research*, vol. 3, no. 1, p. 13137, 2021.

[13] S. Li and R. R. Jones, “High-energy electron emission from metallic nano-tips driven by intense single-cycle terahertz pulses,” *Nature Communications*, vol. 7, pp. 1–7, 2016.

[14] S. L. Lange, N. K. Noori, T. M. B. Kristensen, K. Steenberg, and P. U. Jepsen, “Ultrafast THz-driven electron emission from metal metasurfaces,” *Journal of Applied Physics*, vol. 128, no. 7, p. 070901, 2020.

[15] T. L. Cocker, V. Jelic, M. Gupta, S. J. Molesky, J. A. J. Burgess, G. D. L. Reyes, L. V. Titova, Y. Y. Tsui, M. R. Freeman, and F. A. Hegmann, “An ultrafast terahertz scanning tunnelling microscope,” *Nature Photonics*, vol. 7, pp. 620–625, 8 2013.

[16] T. O. Buchmann, S. L. Lange, M. Sebek, N. Kawai, and P. U. Jepsen, “High Sensitivity THz Photomultiplier Tubes,” *International Conference on Infrared, Millimeter, and Terahertz Waves, IRMMW-THz*, vol. 2022-Augus, pp. 1–2, 2022.

[17] C. L. K. Dandolo and P. U. Jepsen, “Wall Painting Investigation by Means of Non-invasive Terahertz Time-Domain Imaging (THz-TDI): Inspection of Subsurface Structures Buried in Historical Plasters,” *Journal of Infrared, Millimeter, and Terahertz Waves*, vol. 37, no. 2, pp. 198–208, 2016.

[18] B. Hussain, M. Ahmed, M. Nawaz, M. Saleem, M. Razzaq, M. Aslam Zia, and M. Iqbal, “Simultaneous determination of thickness and refractive index based on time-of-flight measurements of terahertz pulse,” *Applied Optics*, vol. 51, no. 21, pp. 5326–5330, 2012.

[19] M. van Exter, C. Fattinger, and D. Grischkowsky, “Terahertz time-domain spectroscopy of water vapor,” *Optics Letters*, vol. 14, no. 20, p. 1128, 1989.

[20] I. F. Akyildiz, C. Han, Z. Hu, S. Nie, and J. M. Jornet, “Terahertz Band Communication: An Old Problem Revisited and Research Directions for the Next Decade,” *IEEE Transactions on Communications*, vol. 70, no. 6, pp. 4250–4285, 2022.

[21] W. He, C. R. Donaldson, L. Zhang, K. Ronald, P. McElhinney, and A. W. Cross, “High power wideband gyrotron backward wave oscillator operating towards the terahertz region,” *Physical Review Letters*, vol. 110, no. 16, pp. 1–5, 2013.

[22] A. Khalid, N. J. Pilgrim, G. M. Dunn, M. C. Holland, C. R. Stanley, I. G. Thayne, and D. R. S. Cumming, “A planar Gunn diode operating above 100 GHz,” *IEEE Electron Device Letters*, vol. 28, no. 10, pp. 849–851, 2007.

[23] R. Köhler, A. Tredicucci, F. Beltram, H. E. Beere, E. H. Linfield, A. G. Davies, D. A. Ritchie, R. C. Iotti, and F. Rossi, "Terahertz semiconductor-heterostructure laser," *Nature*, vol. 417, pp. 156–159, 5 2002.

[24] M. Mittendorff, M. Xu, R. J. Dietz, H. Künzel, B. Sartorius, H. Schneider, M. Helm, and S. Winnerl, "Large area photoconductive terahertz emitter for 1.55 μm excitation based on an InGaAs heterostructure," *Nanotechnology*, vol. 24, no. 21, 2013.

[25] M. Jazbinsek, U. Puc, A. Abina, and A. Zidansek, "Organic crystals for THz photonics," *Applied Sciences*, vol. 9, p. 882, 3 2019.

[26] J. Hebling, K.-L. Yeh, M. C. Hoffmann, B. Bartal, and K. A. Nelson, "Generation of high-power terahertz pulses by tilted-pulse-front excitation and their application possibilities," *Journal of the Optical Society of America B*, vol. 25, p. B6, 7 2008.

[27] H. Zhong, N. Karpowicz, and X. C. Zhang, "Terahertz emission profile from laser-induced air plasma," *Applied Physics Letters*, vol. 88, no. 26, pp. 1–4, 2006.

[28] R. W. Boyd, *Nonlinear Optics*. Elsevier, 4th ed., 2020.

[29] Y.-S. Lee, *Principles of Terahertz Science and Technology*. Boston, MA: Springer US, 1st ed., 2009.

[30] D. Jones, S. Diddams, J. Ranka, A. Stentz, R. Windeler, J. Hall, and S. Cundiff, "Carrier-envelope phase control of femtosecond mode-locked lasers and direct optical frequency synthesis.," *Science (New York, N.Y.)*, vol. 288, pp. 635–40, 4 2000.

[31] C. P. Hauri, C. Ruchert, C. Vicario, and F. Ardana, "Strong-field single-cycle THz pulses generated in an organic crystal," *Applied Physics Letters*, vol. 99, no. 16, 2011.

[32] T. O. Buchmann, E. J. R. Kelleher, K. J. Kaltenecker, B. Zhou, S.-H. Lee, O.-P. Kwon, M. Jazbinsek, F. Rotermund, and P. U. Jepsen, "MHz-repetition-rate, sub-mW, multi-octave THz wave generation in HMQ-TMS," *Optics Express*, vol. 28, p. 9631, 3 2020.

[33] U. Puc, J.-A. Yang, D. Kim, O.-P. Kwon, and M. Jazbinsek, "Broadband THz wave generation in organic benzothiazolium crystals at MHz repetition rates [Invited]," *Optical Materials Express*, vol. 13, no. 1, p. 53, 2023.

[34] S. Mansourzadeh, T. Vogel, M. Shalaby, F. Wulf, and C. J. Saraceno, "Milliwatt average power, MHz-repetition rate, broadband THz generation in organic crystal BNA with diamond substrate," *Optics Express*, vol. 29, no. 24, p. 38946, 2021.

[35] J. Hebling, G. Almasi, I. Kozma, and J. Kuhl, "Velocity matching by pulse front tilting for large area THz-pulse generation," *Optics Express*, vol. 10, no. 21, p. 1161, 2002.

[36] D. H. Auston, K. P. Cheung, J. A. Valdmanis, and D. A. Kleinman, "Cherenkov radiation from femtosecond optical pulses in electro-optic media," *Physical Review Letters*, vol. 53, no. 16, pp. 1555–1558, 1984.

[37] A. G. Stepanov, J. Hebling, and J. Kuhl, "THz generation via optical rectification with ultrashort laser pulse focused to a line," *Applied Physics B: Lasers and Optics*, vol. 81, no. 1, pp. 23–26, 2005.

[38] J. Hebling, "Derivation of the pulse front tilt caused by angular dispersion," *Optical and Quantum Electronics*, vol. 28, no. 12, pp. 1759–1763, 1996.

[39] J. A. Fülöp, L. Pálfalvi, G. Almási, and J. Hebling, "Design of high-energy terahertz sources based on optical rectification," *Optics Express*, vol. 18, p. 12311, 6 2010.

[40] H. Hirori, A. Doi, F. Blanchard, and K. Tanaka, "Single-cycle terahertz pulses with amplitudes exceeding 1 MV/cm generated by optical rectification in LiNbO3," *Applied Physics Letters*, vol. 98, p. 091106, 2 2011.

[41] S.-W. Huang, E. Granados, W. R. Huang, K.-h. Hong, L. E. Zapata, and F. X. Kärtner, "High conversion efficiency, high energy terahertz pulses by optical rectification in cryogenically cooled lithium niobate," *Optics Letters*, vol. 38, p. 796, 3 2013.

[42] M. Jewariya, M. Nagai, and K. Tanaka, "Enhancement of terahertz wave generation by cascaded χ^(2) processes in LiNbO_3," *Journal of the Optical Society of America B*, vol. 26, no. 9, p. A101, 2009.

[43] K. Ravi, W. R. Huang, S. Carbajo, X. Wu, and F. Kärtner, "Limitations to THz generation by optical rectification using tilted pulse fronts," *Optics Express*, vol. 22, no. 17, p. 20239, 2014.

[44] B. K. Ofori-Okai, P. Sivarajah, W. Ronny Huang, and K. A. Nelson, "THz generation using a reflective stair-step echelon," *Optics Express*, vol. 24, p. 5057, 3 2016.

[45] L. Guiramand, J. E. Nkeck, X. Ropagnol, T. Ozaki, and F. Blanchard, "Near-optimal intense and powerful terahertz source by optical rectification in lithium niobate crystal," *Photonics Research*, vol. 10, p. 340, 2 2022.

[46] P. F. Liao and A. Wokaun, "Lightning rod effect in surface enhanced Raman scattering," *The Journal of Chemical Physics*, vol. 76, pp. 751–752, 1 1982.

[47] P. Uhd Jepsen, M. Schall, V. Schyja, C. Winnewisser, H. Helm, and S. R. Keiding, "Detection of High Power THz Pulses by Phase Retardation in an Electro-Optic Crystal," *Ultrafast Processes in Spectroscopy*, vol. 53, no. 4, pp. 645–648, 1996.

[48] J. T. Darrow, X. C. Zhang, and D. H. Auston, "Power scaling of large-aperture photoconducting antennas," *Applied Physics Letters*, vol. 58, no. 1, pp. 25–27, 1991.

[49] A. Singh, A. Pashkin, S. Winnerl, M. Helm, and H. Schneider, "Gapless Broadband Terahertz Emission from a Germanium Photoconductive Emitter," *ACS Photonics*, vol. 5, no. 7, pp. 2718–2723, 2018.

[50] A. Dreyhaupt, S. Winnerl, T. Dekorsy, and M. Helm, “High-intensity terahertz radiation from a microstructured large-area photoconductor,” *Applied Physics Letters*, vol. 86, p. 121114, 3 2005.

[51] C. Headley, L. Fu, P. Parkinson, X. Xu, J. Lloyd-Hughes, C. Jagadish, and M. B. Johnston, “Improved performance of GaAs-based terahertz emitters via surface passivation and silicon nitride encapsulation,” *IEEE Journal on Selected Topics in Quantum Electronics*, vol. 17, no. 1, pp. 17–21, 2011.

[52] C. W. Berry, N. Wang, M. R. Hashemi, M. Unlu, and M. Jarrahi, “Significant performance enhancement in photoconductive terahertz optoelectronics by incorporating plasmonic contact electrodes,” *Nature Communications*, vol. 4, pp. 1610–1622, 2013.

[53] A. Singh, J. Li, A. Pashkin, R. Rana, S. Winnerl, M. Helm, and H. Schneider, “High-field THz pulses from a GaAs photoconductive emitter for non-linear THz studies,” *Optics Express*, vol. 29, no. 13, p. 19920, 2021.

[54] A. Singh, M. Welsch, S. Winnerl, M. Helm, and H. Schneider, “Non-plasmonic improvement in photoconductive THz emitters using nano- and micro-structured electrodes,” *Optics Express*, vol. 28, no. 24, p. 35490, 2020.

[55] “Toptica Product information for TeraFlash pro,” 2023.

[56] D. J. Cook and R. M. Hochstrasser, “Intense terahertz pulses by four-wave rectification in air,” *Optics Letters*, vol. 25, no. 16, p. 1210, 2000.

[57] M. Clerici, M. Peccianti, B. E. Schmidt, L. Caspani, M. Shalaby, M. Giguère, A. Lotti, A. Couairon, F. Légaré, T. Ozaki, D. Faccio, and R. Morandotti, “Wavelength scaling of terahertz generation by gas ionization,” *Physical Review Letters*, vol. 110, no. 25, pp. 1–5, 2013.

[58] B. Zhou, M. Rasmussen, and P. U. Jepsen, “Multi-mW-level, air-plasma induced ultrabroadband THz pulses for nonlinear THz spectroscopy,” *Optics InfoBase Conference Papers*, p. 6654, 2021.

[59] P. R. Whelan, B. Zhou, O. Bezencenet, A. Shivayogimath, N. Mishra, Q. Shen, B. S. Jessen, I. Pasternak, D. M. Mackenzie, J. Ji, C. Sun, P. Seneor, B. Dlubak, B. Luo, F. W. Østerberg, D. Huang, H. Shi, D. Luo, M. Wang, R. S. Ruoff, B. R. Conran, C. McAleese, C. Huyghebaert, S. Brems, T. J. Booth, I. Napal, W. Strupinski, D. H. Petersen, S. Forti, C. Coletti, A. Jouvray, K. B. Teo, A. Centeno, A. Zurutuza, P. Legagneux, P. U. Jepsen, and P. Bøggild, “Case studies of electrical characterisation of graphene by terahertz time-domain spectroscopy,” *2D Materials*, vol. 8, no. 2, 2021.

[60] P. Tan, J. Huang, K. F. Liu, Y. Q. Xiong, and M. W. Fan, “Terahertz radiation sources based on free electron lasers and their applications,” *Science China Information Sciences*, vol. 55, no. 1, pp. 1–15, 2012.

[61] Q. Wu and X. C. Zhang, “Free-space electro-optic sampling of terahertz beams,” *Applied Physics Letters*, vol. 67, no. October 1995, p. 3523, 1995.

[62] P. C. M. Planken, H.-K. Nienhuys, H. J. Bakker, and T. Wenckebach, “Measurement and calculation of the orientation dependence of terahertz pulse detection in ZnTe,” *Journal of the Optical Society of America B*, vol. 18, p. 313, 3 2001.

[63] L. Vicarelli, A. Tredicucci, and A. Pitanti, “Micromechanical Bolometers for Subterahertz Detection at Room Temperature,” *ACS Photonics*, vol. 9, no. 2, pp. 360–367, 2022.

[64] J. Nazdrowicz, M. Szermer, C. Maj, and W. Zabierowski, “Comparative Study on Various Microbolometer Structures,” *International journal of microelectronics and computer science*, vol. 7, no. 1, pp. 16–25, 2016.

[65] N. Oda, A. W. M. Lee, T. Ishi, I. Hosako, and Q. Hu, “Proposal for real-time terahertz imaging system with palm-size terahertz camera and compact quantum cascade laser,” *Terahertz Physics, Devices, and Systems VI: Advanced Applications in Industry and Defense*, vol. 8363, pp. 83630A–83630A–13, 2012.

[66] M. Chirtoc, R. M. Candea, and V. Mercea, “Operation Theory Of Pyroelectric Detectors. I. A New Physical Model And The Resulting Operation Modes,” *Ferroelectrics*, vol. 56, no. 1, pp. 283–291, 1984.

[67] M. Aleksandrova, C. Jagtap, V. Kadam, S. Jadkar, G. Kolev, K. Denishev, and H. M. Pathan, “An Overview of Microelectronic Infrared Pyroelectric Detector,” *Engineered Science*, vol. 16, no. 2, pp. 82–89, 2021.

[68] D. S. Sitnikov, S. A. Romashevskiy, A. V. Ovchinnikov, O. V. Chefonov, A. B. Savel’ev, and M. B. Agranat, “Estimation of THz field strength by an electro-optic sampling technique using arbitrary long gating pulses,” *Laser Physics Letters*, vol. 16, p. 115302, 11 2019.

[69] A. Einstein, “Über einen die Erzeugung und Verwandlung des Lichtes betreffenden heuristischen Gesichtspunkt,” *Annalen der Physik*, vol. 322, no. 6, pp. 132–148, 1905.

[70] P. Agostini, F. Fabre, G. Mainfray, G. Petite, and N. K. Rahman, “Free-free transitions following six-photon ionization of xenon atoms,” *Physical Review Letters*, vol. 42, no. 17, pp. 1127–1130, 1979.

[71] L. Wimmer, G. Herink, D. R. Solli, S. V. Yalunin, K. E. Echternkamp, and C. Ropers, “Terahertz control of nanotip photoemission,” *Nature Physics*, vol. 10, no. 6, pp. 432–436, 2014.

[72] R. Stratton, “Theory of Field Emission from Semiconductors,” *Physical Review*, vol. 125, pp. 67–82, 1 1962.

[73] Z.-S. Wu, S. Pei, W. Ren, D. Tang, L. Gao, B. Liu, F. Li, C. Liu, and H.-M. Cheng, "Field Emission of Single-Layer Graphene Films Prepared by Electrophoretic Deposition," *Advanced Materials*, vol. 21, pp. 1756–1760, 5 2009.

[74] A. Ghalgaoui, L. M. Koll, B. Schütte, B. P. Fingerhut, K. Reimann, M. Woerner, and T. Elsaesser, "Field-Induced Tunneling Ionization and Terahertz-Driven Electron Dynamics in Liquid Water," *Journal of Physical Chemistry Letters*, vol. 11, no. 18, pp. 7717–7722, 2020.

[75] E. Rokuta, H. S. Kuo, T. Itagaki, K. Nomura, T. Ishikawa, B. L. Cho, I. S. Hwang, T. T. Tsong, and C. Oshima, "Field emission spectra of single-atom tips with thermodynamically stable structures," *Surface Science*, vol. 602, no. 14, pp. 2508–2512, 2008.

[76] C. Kittel, *Introduction to Solid State Physics*. John Wiley & Sons, Inc., 8th ed., 11 2004.

[77] H. B. Michaelson, "The work function of the elements and its periodicity," *Journal of Applied Physics*, vol. 48, no. 11, pp. 4729–4733, 1977.

[78] R. G. Forbes, "Use of energy-space diagrams in free-electron models of field electron emission," *Surface and Interface Analysis*, vol. 36, no. 5-6 SPEC. ISS., pp. 395–401, 2004.

[79] R. G. Forbes, "Field electron emission theory (October 2016)," in *2016 Young Researchers in Vacuum Micro/Nano Electronics (VMNE-YR)*, pp. 1–8, IEEE, 10 2016.

[80] K. L. Jensen, "Electron emission theory and its application: Fowler–Nordheim equation and beyond," *Journal of Vacuum Science & Technology B: Microelectronics and Nanometer Structures*, vol. 21, no. 4, p. 1528, 2003.

[81] G. Binnig, H. Rohrer, C. Gerber, and E. Weibel, "Tunneling through a controllable vacuum gap," *Applied Physics Letters*, vol. 40, no. 2, pp. 178–180, 1982.

[82] L. Nordheim, "The effect of the image force on the emission and reflexion of electrons by metals," *Proceedings of the Royal Society of London. Series A, Containing Papers of a Mathematical and Physical Character*, vol. 121, no. 788, pp. 626–639, 1928.

[83] E. L. Murphy and R. H. Good, "Thermionic Emission, Field Emission, and the Transition Region," *Physical Review*, vol. 102, no. 6, pp. 1464–1473, 1956.

[84] R. G. Forbes and J. H. Deane, "Reformulation of the standard theory of Fowler-Nordheim tunnelling and cold field electron emission," *Proceedings of the Royal Society A: Mathematical, Physical and Engineering Sciences*, vol. 463, no. 2087, pp. 2907–2927, 2007.

[85] R. G. Forbes, "Comments on the continuing widespread and unnecessary use of a defective emission equation in field emission related literature," *Journal of Applied Physics*, vol. 126, no. 21, 2019.

[86] R. G. Forbes, J. H. Deane, A. Fischer, and M. S. Mousa, “Fowler-nordheim plot analysis: A progress report,” *Jordan Journal of Physics*, vol. 8, no. 3, pp. 125–147, 2015.

[87] A. M. Zheltikov, “Keldysh photoionization theory: through the barriers,” *Uspekhi Fizicheskih Nauk*, vol. 187, pp. 1169–1204, 11 2017.

[88] L. V. Keldysh, “Ionization in the field of a strong electromagnetic wave,” *Soviet Physics Jetp*, vol. 20, no. 5, 1964.

[89] S. L. Lange, *Terahertz-Enabled Ultrafast Electron Field Emission From Fundamentals to Applications*. PhD thesis, Technical University of Denmark, 2019.

[90] S. L. Lange, K. Iwaszczuk, M. Hoffmann, J. Broeng, and P. U. Jepsen, “Time-domain electric field enhancement on micrometer scale in coupled split ring resonator upon terahertz radiation,” *International Conference on Infrared, Millimeter, and Terahertz Waves, IRMMW-THz*, vol. 2016-Novem, 2016.

[91] S. S. Bukhari, J. Vardaxoglou, and W. Whittow, “A metasurfaces review: Definitions and applications,” *Applied Sciences (Switzerland)*, vol. 9, no. 13, 2019.

[92] K. Iwaszczuk, M. Zalkovskij, A. C. Strikwerda, and P. U. Jepsen, “Nitrogen plasma formation through terahertz-induced ultrafast electron field emission,” *Optica*, vol. 2, p. 116, 2 2015.

[93] S. L. Lange, L. R. Lindvold, and P. U. Jepsen, “Direct Injection of Ultrashort Electron Bunches into a Solid Material Using Terahertz-Driven Electron Field Emission,” in *International Conference on Infrared, Millimeter, and Terahertz Waves, IRMMW-THz*, vol. 2018-Septe, pp. 1–2, IEEE, 9 2018.

[94] T. Geldhauser, A. Kolloch, N. Murazawa, K. Ueno, J. Boneberg, P. Leiderer, E. Scheer, and H. Misawa, “Quantitative measurement of the near-field enhancement of nanostructures by two-photon polymerization,” *Langmuir*, vol. 28, no. 24, pp. 9041–9046, 2012.

[95] S. Komatsu, E. Ohta, H. Tanaka, Y. Moriyoshi, K. Nakajima, T. Chikyo, and M. Shiratani, “Electron field emission in air at an atmospheric pressure from sp 3-bonded 5H-BN microcones,” *Journal of Applied Physics*, vol. 101, no. 8, pp. 3–8, 2007.

[96] W. Park, Y. Lee, T. Kang, J. Jeong, and D. S. Kim, “Terahertz-driven polymerization of resists in nanoantennas,” *Scientific Reports*, vol. 8, no. 1, pp. 1–6, 2018.

[97] P. Zilio, M. Dipalo, F. Tantussi, G. C. Messina, and F. De Angelis, “Hot electrons in water: Injection and ponderomotive acceleration by means of plasmonic nanoelectrodes,” *Light: Science and Applications*, vol. 6, no. 6, pp. 17002–8, 2017.

[98] W. F. Schmidt and W. Schnabel, “Electron Injection into Dielectric Liquids by Field Emission,” *Zeitschrift fur Naturforschung - Section A Journal of Physical Sciences*, vol. 26, no. 1, pp. 169–170, 1971.

[99] K. Dotoku, H. Yamada, S. Sakamoto, S. Noda, and H. Yoshida, "Field emission into nonpolar organic liquids," *The Journal of Chemical Physics*, vol. 69, no. 3, pp. 1121–1125, 1978.

[100] J. J. Munro, S. Harrison, M. M. Fujimoto, and J. Tennyson, "A dissociative electron attachment cross-section estimator," *Journal of Physics: Conference Series*, vol. 388, p. 012013, 11 2012.

[101] S. Ptasińska and L. Sanche, "Dissociative electron attachment to hydrated single DNA strands," *Physical Review E*, vol. 75, p. 031915, 3 2007.

[102] C. Dass, *Fundamentals of Contemporary Mass Spectrometry*, vol. 18. John Wiley & Sons, Inc., 1st ed., 2007.

[103] Y. Zhang, X. Wang, L. F. Zhu, D. Lu, R. Hutton, Y. Zou, and B. Wei, "Dissociative ionization of N2 by fast electron impact: Roles of molecular orbitals," *Journal of Physics B: Atomic, Molecular and Optical Physics*, vol. 50, no. 20, 2017.

[104] T. D. Märk and G. H. Dunn, eds., *Electron Impact Ionization*. Vienna: Springer Vienna, 1st ed., 1985.

[105] J. Ma, A. Kumar, Y. Muroya, S. Yamashita, T. Sakurai, S. A. Denisov, M. D. Sevilla, A. Adhikary, S. Seki, and M. Mostafavi, "Observation of dissociative quasi-free electron attachment to nucleoside via excited anion radical in solution," *Nature Communications*, vol. 10, no. 1, pp. 1–7, 2019.

[106] F. Arnold, "Solvated electrons in the upper atmosphere," *Nature*, vol. 294, no. 5843, pp. 732–733, 1981.

[107] G. Zhang, T. Dai, Y. Wang, Y. Meng, B. Xie, Z. Ni, and S. Xia, "Modulation of photo-generated solvated electrons for ammonia synthesis via facet-dependent engineering of heterojunctions," *Applied Catalysis B: Environmental*, vol. 288, no. February, p. 119990, 2021.

[108] J. Li, Z. Nie, Y. Y. Zheng, S. Dong, and Z. H. Loh, "Elementary electron and ion dynamics in ionized liquid water," *Optics InfoBase Conference Papers*, 2014.

[109] A. Migus, Y. Gauduel, J. L. Martin, and A. Antonetti, "Excess electrons in liquid water: First evidence of a prehydrated state with femtosecond lifetime," *Physical Review Letters*, vol. 58, pp. 1559–1562, 4 1987.

[110] J. Ma, S. A. Denisov, A. Adhikary, and M. Mostafavi, "Ultrafast processes occurring in radiolysis of highly concentrated solutions of nucleosides/tides," *International Journal of Molecular Sciences*, vol. 20, no. 19, 2019.

[111] A. Bogaerts, R. Gijbels, and J. Vlcek, "Modeling of glow discharge optical emission spectrometry: Calculation of the argon atomic optical emission spectrum," *Spectrochimica acta, Part B: Atomic spectroscopy*, vol. 53, no. 11, pp. 1517–1526, 1998.

[112] S. J. Lange, M. C. Hoffmann, and P. U. Jepsen, “Lightwave-driven electron emission for polarity-sensitive terahertz beam profiling,” *APL Photonics*, vol. 8, p. 016105, 1 2023.

[113] M. Mosquera, J. C. Penedo, M. C. Ríos Rodríguez, and F. Rodrìguez-Prieto, “Photoinduced inter- and intramolecular proton transfer in aqueous and ethanolic solutions of 2-(2′-hydroxyphenyl)benzimidazole: Evidence for tautomeric and conformational equilibria in the ground state,” *Journal of Physical Chemistry*, vol. 100, no. 13, pp. 5398–5407, 1996.

[114] L. Ying, S. Chun-Yuan, L. Xiao-Sen, L. Jian, and N. Xiao-Wu, “Fluorescence spectrum characteristic of ethanol–water excimer and mechanism of resonance energy transfer,” *Chinese Physics*, vol. 16, pp. 1300–1306, 5 2007.

[115] H.-D. Beckey, *Principles of field ionization and field desorption mass spectrometry*. Pergamon Pr., 1977.

[116] C. Z. Bisgaard and L. B. Madsen, “Tunneling ionization of atoms,” *American Journal of Physics*, vol. 72, no. 2, pp. 249–254, 2004.

[117] X. M. Tong, Z. X. Zhao, and C. D. Lin, “Theory of molecular tunneling ionization,” *Physical Review A - Atomic, Molecular, and Optical Physics*, vol. 66, no. 3, p. 11, 2002.

[118] S. Hyeon and T.-I. Jeon, “Pressure-dependent refractive indices of gases by THz time-domain spectroscopy,” *Optics Express*, vol. 24, no. 25, p. 29040, 2016.

[119] F. R. Abbott and J. E. Henderson, “The range and validity of the field current equation,” *Physical Review*, vol. 56, no. 1, pp. 113–118, 1939.

[120] R. G. Forbes, “Call for experimental test of a revised mathematical form for empirical field emission current-voltage characteristics,” *Applied Physics Letters*, vol. 92, p. 193105, 5 2008.

[121] M. Zubair, Y. S. Ang, L. K. Ang, and S. Member, “Fractional Fowler-Nordheim Law for Field Emission From Rough Surface With Nonparabolic Energy Dispersion,” *IEEE Transactions on Electron Devices*, vol. 65, no. 6, pp. 2089–2095, 2018.

[122] B. Halpern and R. Gomer, “Field ionization in liquids,” *The Journal of Chemical Physics*, vol. 51, no. 3, pp. 1048–1056, 1969.

[123] S. A. Lang, A. M. Darr, and A. L. Garner, “Theoretical analysis of the transition from field emission to space-charge-limited emission in liquids and gases,” *Journal of Applied Physics*, vol. 128, no. 18, 2020.

[124] M. Aljure, M. Becerra, and M. E. Karlsson, “On the injection and generation of charge carriers in mineral oil under high electric fields,” *Journal of Physics Communications*, vol. 3, no. 3, 2019.

[125] P. Drude, “Zur Elektronentheorie der Metalle,” *Annalen der Physik*, vol. 306, no. 3, pp. 566–613, 1900.

[126] “LXCat database.”

[127] C. Yamabe, S. J. Buckman, and A. V. Phelps, “Measurement of free-free emission from low-energy-electron collisions with Ar,” *Physical Review A*, vol. 27, no. 3, pp. 1345–1352, 1983.

[128] C. Berthomieu and R. Hienerwadel, “Fourier transform infrared (FTIR) spectroscopy,” *Photosynthesis Research*, vol. 101, no. 2-3, pp. 157–170, 2009.

[129] A. Lochbaum, A. Dorodnyy, U. Koch, S. M. Koepfli, S. Volk, Y. Fedoryshyn, V. Wood, and J. Leuthold, “Compact Mid-Infrared Gas Sensing Enabled by an All-Metamaterial Design,” *Nano Letters*, vol. 20, no. 6, pp. 4169–4176, 2020.

[130] D. S. Boyd and F. Petitcolin, “Remote sensing of the terrestrial environment using middle infrared radiation (3.0-5.0 μm),” *International Journal of Remote Sensing*, vol. 25, no. 17, pp. 3343–3368, 2004.

[131] S. Türker-Kaya and C. W. Huck, “A review of mid-infrared and near-infrared imaging: Principles, concepts and applications in plant tissue analysis,” *Molecules*, vol. 22, no. 1, 2017.

[132] R. F. Potter and W. L. Eisenman, “Infrared Photodetectors: A Review of Operational Detectors,” *Applied Optics*, vol. 1, no. 5, p. 567, 1962.

[133] J. Haas and B. Mizaikoff, “Advances in Mid-Infrared Spectroscopy for Chemical Analysis,” *Annual Review of Analytical Chemistry*, vol. 9, pp. 45–68, 2016.

[134] A. Karim and J. Y. Andersson, “Infrared detectors: Advances, challenges and new technologies,” *IOP Conference Series: Materials Science and Engineering*, vol. 51, p. 012001, 12 2013.

[135] *Handbook for Photomultiplier Tubes*. Hamamatsu Photonics, 4th ed., 2017.

[136] G. Herink, D. R. Solli, M. Gulde, and C. Ropers, “Field-driven photoemission from nanostructures quenches the quiver motion,” *Nature*, vol. 483, pp. 190–193, 3 2012.

[137] J.-C. M. Diels, J. J. Fontaine, I. C. McMichael, and F. Simoni, “Control and measurement of ultrashort pulse shapes (in amplitude and phase) with femtosecond accuracy,” *Applied Optics*, vol. 24, no. 9, p. 1270, 1985.

[138] S. Jarabo, E. Rodríguez-Martín, J. E. Saldaña-Díaz, and F. J. Salgado-Remacha, “Sensitivity enhancement by increasing the nonlinear crystal length in second-order autocorrelators for ultrashort laser pulses measurement,” *Optics Communications*, vol. 437, no. January, pp. 367–372, 2019.

[139] Y. Takagi, S. Imamura, T. Kobayashi, and K. Yoshihara, “Multiple- and single-shot autocorrelator based on two-photon conductivity in semiconductors,” *Optics Letters*, vol. 17, no. 9, p. 658, 1992.

[140] A. Baltuska, M. S. Pshenichnikov, D. A. Wiersma, J. K. Ranka, and A. L. Gaeta, “Autocorrelation measurement of 6-fs pulses based on the two-photon induced photocurrent in a GaAsP photodiode,” *Optics InfoBase Conference Papers*, vol. 22, no. 17, pp. 1344–1346, 1997.

[141] R. Trebino, *Frequency-Resolved Optical Gating: The Measurement of Ultrashort Laser Pulses*. Springer US, 1st ed., 2000.

[142] G. Herink, D. R. Solli, M. Gulde, and C. Ropers, “Subplementary Info: Field-driven photoemission from nanostructures quenches the quiver motion,” *Nature*, vol. 483, no. 7388, pp. 190–193, 2012.

[143] B. Abel, U. Buck, A. L. Sobolewski, and W. Domcke, “On the nature and signatures of the solvated electron in water,” *Physical Chemistry Chemical Physics*, vol. 14, no. 1, pp. 22–34, 2012.

[144] V. Svoboda, R. Michiels, A. C. LaForge, J. Med, F. Stienkemeier, P. Slavíček, and H. J. Wörner, “Real-time observation of water radiolysis and hydrated electron formation induced by extreme-ultraviolet pulses,” *Science Advances*, vol. 6, no. 3, pp. 1–9, 2020.

[145] Y. I. Yamamoto and T. Suzuki, “Ultrafast Dynamics of Water Radiolysis: Hydrated Electron Formation, Solvation, Recombination, and Scavenging,” *Journal of Physical Chemistry Letters*, vol. 11, no. 14, pp. 5510–5516, 2020.

[146] E. J. Hart and J. W. Boag, “Absorption Spectrum of the Hydrated Electron in Water and in Aqueous Solutions,” *Journal of the American Chemical Society*, vol. 84, pp. 4090–4095, 11 1962.